Stony Brook University

Quantum Gases in State-Dependent Optical Potentials

A Thesis Presented

by

René Harald Reimann

to

The Graduate School

in Partial Fulfillment of the Requirements

for the Degree of

Master of Arts

in

Physics

Stony Brook University

August 2009

Stony Brook University

The Graduate School

René Harald Reimann

We, the thesis committee for the above candidate for the Master of Arts degree, hereby recommend acceptance of this thesis.

Dominik Schneble – Thesis Advisor
Assistant Professor, Department of Physics and Astronomy
Stony Brook University

Harold Metcalf – Chairperson of Defense
Distinguished Teaching Professor, Department of Physics and Astronomy
Stony Brook University

Thomas Bergeman
Adjunct Professor, Department of Physics and Astronomy
Stony Brook University

This thesis is accepted by the Graduate School.

Lawrence Martin
Dean of the Graduate School

Abstract of the Thesis

Quantum Gases in State-Dependent Optical Potentials

by

René Harald Reimann

Master of Arts

in

Physics

Stony Brook University

2009

This thesis describes preliminary results for the first experimental implementation of a state-dependent two-component superfluid-Mott insulator transition for two inter-convertible atomic species. The system is realized in a ^{87}Rb moving coil transporter Bose-Einstein condensate machine.

The implementation of a crossed optical dipole trap and optical lattices is described. By experimentally performing a one-component superfluid-Mott insulator transition the reliability of the Bose-Einstein condensate machine is shown.

State-dependent optical potentials and scattering rates are treated theoretically as well as experimentally in good agreement with each other.

Finally the first state-dependent two-component superfluid-Mott insulator transition is presented and a comparison of the system with theory is discussed, as well as issues of interaction between the two atomic components.

To Christina

Contents

List of Figures

List of Tables

Acknowledgments

Even though my girlfriend Christina might not like to hear these words, I have to say that my year in Stony Brook passed by pretty fast. I mostly contribute this to the "cool" atmosphere in the BEC lab, where work is fun.
Becoming serious now I would like to thank my advisor Dominik Schneble who accepted me with open arms as I arrived in August 2008. Even if he would not pay me right now for working in his lab, I certainly would note that Dominik is the best kind of advisor a student can have.
I thank Dominik for his cheerfulness that allows me to write my acknowledgments the way I do. Of course he is a great guy. It has never happened that he left me alone with a question I asked him ("Dominik, how is it with...." - "GREAT!!! Ja, what's up?"). He is very often in the lab and motivates through his advise and action. On the other hand I never felt "negative" pressure from his side which leads to the fact that I love spending my time in the BEC lab.
The lab atmosphere was completed in a perfect manner by Daniel Pertot, Bryce Gadway, Bartosz Bogucki and Marty Cohen.
Daniel is very well educated in both, theory and experiment and acts and thinks in a very accurate way. Thank you Daniel for answering many of my questions and for driving me home in rainy nights.
Bryce is pretty smart, too. His talent in physics is amazing. Furthermore it appears that he is experimentally immovable. No experimental disaster seems to be able to make him desperate.
Bryce and Daniel have made a huge experimental contribution to the work presented in this thesis.
Unfortunately I never had a closer interaction with Bart, but he certainly is a very nice guy and can build electronic devices that do not even have the possibility of being, in my mind.
I am also grateful to Marty who often helped when specific experimental questions arose, and proofread this thesis with Bryce and Daniel. Thank you all for your helpful comments and corrections.
Harold Metcalf, Thomas Bergeman and Dominik are in my thesis committee

and gave me very constructive feedback - thank you very much for that.
Of course I do not want to miss the opportunity to express my gratefulness to Fakher Assaad, Laszlo Mihaly and Peter Koch who made the exchange between Würzburg and Stony Brook possible. Furthermore I would like to thank Harold Metcalf who was there at the very beginning to answer my questions and helped me out by lending me a bike.
With switching from work to weekend, I would like to mention my close friend Ali. Having dinner with you on Saturdays and discussing cultural, political, philosophical and personal issues with you enlarged my horizon immensely. People like you are rare.
Finally I want to thank my girlfriend Christina. Even though you sometimes might have the feeling that physics is more important to me than you, I certainly know that this is not true. Thank you for staying by my side for this year. I really look forward to have you again. This thesis is dedicated to you.

I acknowledge support of DAAD, the German government and the Research Foundation of the State University of New York.

Chapter 1

Introduction

The theoretical foundation for Bose-Einstein condensation (BEC) was formulated in 1924 (for a theoretical review on BEC in dilute trapped gases see [1]). In short, condensation happens at low enough temperatures when bosons macroscopically occupy the energetic ground state of the system. For the achievement of BEC in dilute atomic gases (for an experimental review see [2]) the invention of lasers [3] in 1958 and laser cooling in the 1980s [4] were necessary. After a rather short time the first condensates with alkali metals were achieved in 1995 [5–7]. To date many interesting experiments with BECs have been performed and studied, for instance, interference between two BECs, collective excitations, atom lasers or vortices in BECs (for reviews see [1, 2, 8, 9]).

Here we will concentrate on the scenario of ultracold atoms in an optical lattice. When two laser beams of the same wavelength counter-propagate, they form a 1D optical lattice due to interference. Using the freedom of polarization and more laser beams optical lattices of higher dimensionality and complexity can be formed [10]. Atoms interact with these lattices via the dipole force [11]. For now we restrict ourselves to far detuned optical lattices where scattering can be neglected and the internal structure of the atoms is not important. When studying cold atoms in an optical lattice, one has to distinguish between laser cooled atoms ($T \sim 100$ μK, $n \sim 10^{11}$ cm^{-3}) or a BEC ($T \sim 100$ nK, $n \sim 10^{14}$ cm^{-3}) as starting point. The former scenario is in the weakly-interacting regime because the density of the atoms in the "light crystal" is so low that the atoms practically never see each other [8]. The latter case has the potential to explore the strongly-interacting regime where the filling factor (the number of atoms per lattice site) is on the order of one and atom-atom interactions are important. Both cases, however, have in common that the systems are well described by basic solid state theory, which, however, cannot always be probed in a solid. The main advantages of

a "light crystal" over an actual one, are the missing defects of the "light crystal" and the possibility to easily vary the lattice properties by changing the intensities, polarizations and wavelengths of the lattice light nearly without any experimental restrictions. Furthermore, lattice experiments with different dimensionality can be performed and the lattice can be turned on and off arbitrarily. These facts enable the system to probe solid state theories in regions where no solid exists.

In the 1990s the weakly-interacting regime has been studied a lot. At the beginning of the decade the localization of laser cooled atoms to less than an optical wavelength in a 3D lattice was reported [12]. A few years later the quantized motion of cold atoms [13] (in three dimensions), [14] (in two dimensions), [15] (in two and three dimensions) was observed. The first experimental connections between typical solid state scenarios and atom-optical lattice systems where found by the groups of C. Salomon [16] and M. G. Raizen [17, 18]. The famous Bloch oscillations and Wannier-Stark ladders, both predicted for solid state systems, were observed in an artificial light crystal. The static electric field that accelerates the electrons in the solid state case was modeled by accelerating the optical lattice via detuning the frequencies of the two beams. The advantage of the new atom-light system indeed becomes clear in the case of Bloch oscillations. These oscillations have already been observed in 1992 in semiconductor superlattices [19]. In this case the oscillations were damped because the typical timescale of the oscillations was on the same order of magnitude as relaxation processes (scattering from lattice defects, phonons,...). The damping in the atom-light experiments, however can be adjusted by the detuning of the lattice lasers[1] [20] and Feshbach resonances [21]. Therefore new regimes can be entered.

In 2001 the group of M. A. Kasevich explored the strongly-correlated regime where atom-atom interactions become important, in a one dimensional experiment [22]. One year later the group of T. W. Hänsch opened up a new branch of BEC experiments [23]. Using a 3D optical lattice for ^{87}Rb atoms they were able to leave the weakly-interacting BEC regime and entered a strongly correlated regime that is known as the Bose-Hubbard regime [24]. A phase transition from the superfluid to the Mott insulating phase was observed. In the former phase the atoms can move freely from one lattice site to the next and a global phase is established (like in the BEC case without lattice) while the latter phase is characterized by a fixed atom number at each site and no global phase coherence. Since then quantum transitions in different dimensions and dynamics of the boson-lattice systems have been studied. Furthermore,

[1] Far-detuned from atomic resonance → no damping. Detuning close to resonance → strong damping.

fermions have been introduced (for a review see [8]). In 2003 T. W. Hänsch's group used the idea of spin-selective potentials [25, 26] to transport and collide atoms of different hyperfine states [27, 28] in a controlled way. A spin-selective or state-dependent potential could, for instance, be chosen in a way such that one hyperfine state of an atom conservatively interacts with the light that forms the potential but another hyperfine state of the same atom does not at all.
In this thesis experiments which combine the SF-MI approach with spin-selective potentials to a state-dependent 3D superfluid-Mott insulator (SF-MI) transition are discussed.

The thesis is divided into five parts. First a general BEC and optical lattice toolbox is introduced. An explanation of experimentally useful techniques like time-of-flight imaging or visibility measurements follows a short theoretical BEC discussion. The general tools provided in this chapter will be used during the entire thesis.
In the third chapter we partially recall the work that has been done before in our group as an experimental basis. The machine with its moving coil transporter is discussed as well as the laser and vacuum systems. Finally the BEC production is reviewed.
The fourth chapter starts with a theoretical description of the interaction between atoms and light. This description is used to introduce the crossed optical dipole trap (XODT). A measurement of the XODT frequencies follows. In addition optical lattices and state-dependent potentials and scattering rates are covered, both theoretically and experimentally. A reliable method for lattice depth calibration via the Kapitza-Dirac effect is established.
In the fifth chapter the well-known one-component SF-MI transition is repeated. The Bose-Hubbard model as well as a useful solid state description of the atom-light system is given.
Finally the first experimentally achieved state-dependent two-component SF-MI transition for two inter-convertible species is shown. Comparisons with theory and experimental challenges are discussed and analyzed.

Chapter 2

Basic Aspects of Bose-Einstein Condensates and Experimental Methods

In this chapter we introduce general theoretical descriptions which will provide us with experimentally useful statements and tools. This chapter is written to give a fundamental basis which is needed in many parts of the thesis or to explain general concepts of the BEC theory or related topics. Discussions which are more specific to this work will appear in later chapters.

2.1 BEC Theory

In a simple model one can think of bosonic atoms as point particles with a mass m but no further intrinsic properties. In a quantum mechanical formalism these atoms can be described as "wave packets" with a typical extension scale that is given by their thermal de Broglie wavelength $\lambda_T = \sqrt{(2\pi\hbar^2)/(m\mathrm{k_B}T)}$ with T being the temperature and $\mathrm{k_B}$ being Boltzmann's constant. A quantum mechanical description becomes inevitable when this wavelength extends to scales which are comparable to intrinsic scales of the considered system. Here this intrinsic scale is the inter particle spacing d. Assuming that each particle has a small cubic box with volume $V = d^3$ it can call its own, the particle density $n = N/V$ connects to particle spacing by $nd^3 = 1$. In our simple picture Bose-Einstein condensation appears when the atomic "wave packets" start to overlap which means $\lambda_T \sim d$. Therefore condensation starts to occur for

$$n\lambda_{T_c}^3 \sim 1 \tag{2.1}$$

where every particle starts to be at "any place" in the system because of the fundamental principle of indistinguishability in quantum mechanics. T_c is called the critical temperature for which the transition starts and a macroscopic number of particles occupy the ground state. For T=0 condensation is complete and all particles are in the lowest energetic state. The system is sometimes said to be a "giant matter wave" [2] because it can be described by a macroscopic wave function. The quantity $n\lambda_T^3$ of eq. 2.1 is called the phase space density. Ref. [2] gives a very nice introduction to BECs from an experimental point of view. Performing a proper statistical calculation for a homogeneous bosonic gas in 3D [29], one gets $n\lambda_{T_\mathrm{c}}^3 = \zeta_{3/2}[1] \approx 2.6$, where $\zeta_n[x]$ is the Riemann zeta function.

2.1.1 Non-Interacting Bosons in a Harmonic Trap

In all the experiments we will discuss later, the external trap confinement for the atoms can be approximated harmonically which gives a general potential of the form

$$V_\mathrm{ext}[\mathbf{r}] = \frac{m}{2} \sum_{i=x,y,z} \omega_i^2 i^2 \ \text{ with} \tag{2.2}$$
$$\text{eigenenergies } \ \epsilon_{n_x n_y n_z} = \sum_{i=x,y,z} \hbar\omega_i (n_i + 1/2)$$

The eigenenergies belong to the single particle Hamiltonian of the non-interacting system and the n_i are non negative integers. The quantum-statistical calculation starts with the Bose-Einstein distribution which gives the average particle number in the quantum state k with energy ϵ_k

$$f[\epsilon_k] = \frac{1}{\exp[\beta(\epsilon_k - \mu)] - 1} \ \text{ with } \ \beta = (\mathrm{k_B} T)^{-1} \tag{2.3}$$

From eq. 2.2 and eq. 2.3 all needed relations can be derived with the help of the formalism of statistical mechanics (cf. [1, 29]) in the frame of the grand canonical ensemble. Doing so one can derive the critical temperature[1] T_c at which the phase transition to the BEC happens, by setting $\mu = \epsilon_{000}$.

$$T_c = \frac{\hbar\tilde{\omega}}{\mathrm{k_B}} \left(\frac{N}{\zeta_3[1]} \right) \ \text{ with } \ \tilde{\omega} = (\omega_x \omega_y \omega_z)^{1/3} \tag{2.4}$$

[1] In a lattice, the critical temperature is reduced compared to the described case. This happens due to an increase of the effective mass [8].

As stated above, only at $T = 0$ are all N atoms in the condensate. For $0 < T < T_c$ some of the bosons are not in the ground state and contribute to a thermal background. The condensate fraction is then given by

$$\frac{N_0}{N} = 1 - \left(\frac{T}{T_c}\right)^3 \tag{2.5}$$

where N_0 gives the number of atoms being in the ground state. It is impressive that the BEC phase transition happens only because of quantum statistics and not because of interactions between the particles.

2.1.2 Effects of Interaction

Even though the non-interacting gas model gives a qualitatively correct description details like the shape of the condensate cannot be explained. Therefore interactions have to be introduced.

Gross-Pitaevskii Equation

In 1947 Bogoliubov treated the superfluid problem with a mean field approach [1]. Without going into details, for $N_0 \gg 1$ he wrote the bosonic field operator as sum of a complex function $\Psi[\mathbf{r}, t]$ and a small perturbative field operator. $\Psi[\mathbf{r}, t]$ is called the condensate wavefunction and relates to the condensate number density by $n_0[\mathbf{r}, t] = |\Psi[\mathbf{r}, t]|^2$.
Starting with this idea Gross and Piteavskii derived in 1961 their well-known equation which reads in the time independent form

$$\left(-\frac{\hbar^2}{2m}\Delta + V_{\text{ext}}[\mathbf{r}] + g|\Psi[\mathbf{r}]|^2\right)\Psi[\mathbf{r}] = \mu\Psi[\mathbf{r}] \tag{2.6}$$

A derivation can be found in [30]. The interaction potential for eq. 2.6 has been approximated by a pseudo contact potential which is characterized by

$$g = \frac{4\pi\hbar^2 a_s}{m} \tag{2.7}$$

This can be done because of the diluteness ($d \gg a_s$) of the gas which leads to a simplification of the complex many body potential. Interactions are based on elastic two particle collisions which are described by the s-wave scattering length a_s and a mean-field energy. a_s will be positive in all discussed cases herein. The interaction potential is therefore repulsive. Eq. 2.6 is only strictly valid for T=0 when all the atoms are in the condensate.

Thomas-Fermi Approximation

If one neglects the kinetic term in eq. 2.6, a simple equation for the density profile is achieved

$$n_0[\mathbf{r}] = (\mu - V_{\text{ext}}[\mathbf{r}])/g \tag{2.8}$$

for $V_{\text{ext}}[\mathbf{r}] < \mu$ and $n_0 = 0$ elsewhere. This approximation is referred to the Thomas-Fermi approximation and is valid for the limit $E_{\text{int}}/E_{\text{kin}} \sim N_0 a_s/a_{\text{ho}} \gg 1$ with the typical trap length scale $a_{\text{ho}} = \sqrt{\hbar/(m\tilde{\omega})}$. For our experimental situation this translates to $10^{-3}N_0 \gg 1$ which is fulfilled in all of the experiments that will be discussed. The density profile of the cloud in eq. 2.8 is an inverted paraboloid. The approximation is very good except for the outer shell of the condensate were the quantum pressure ($\Delta\Psi[\mathbf{r}]$-term) is not completely insignificant. In discussing the size of a condensate, the so-called Thomas-Fermi radius is often considered. This radius measures from the center of the condensate to the point where the density in eq. 2.8 becomes 0. For a spherical trapping potential, it is [1]

$$R_{\text{TF}} = a_{\text{ho}} \left(\frac{15 N_0 a_s}{a_{\text{ho}}} \right)^{1/5} \tag{2.9}$$

This concludes the short theoretical BEC description. Refs. [1, 2, 8, 30] provide a good introduction on a much broader basis than given here.

2.2 Time-of-Flight Measurement and Absorptive Imaging

With a BEC confined in a harmonic trap, one can generally image the trapped cloud (in-situ), or switch the trap off and image the atoms after a certain time-of-flight (TOF). The TOF method has the advantage that it reveals the momentum distribution of the BEC after the ballistic expansion. This happens due to the quantum pressure of the BEC in the trap (see eq. 2.6). For an anisotropic trap this leads to a bigger momentum along the more confined directions and therefore to an anisotropic expansion of the BEC cloud with TOF [31]. Assuming thermal equilibrium between the thermal background and the BEC the temperature of the system can be calculated by fitting the BEC with a Thomas-Fermi parabola and the thermal background with a thermal Gaussian [2].
Ref. [2] also discusses different techniques for imaging the atom cloud. In our case, we exclusively use absorptive imaging [32, 33]. The principle of this

technique is very simple. The atoms absorb photons of a laser beam that illuminates them for imaging. The emission of the absorbed photons follows also spontaneously in a random direction. This means that the atom cloud can be seen as a shadow in the imaging beam which shines on a CCD chip of a camera. To cancel inhomogeneous illumination and background noise of the data, three pictures are taken. One with atoms and imaging light which leads to an intensity $I_{\text{atoms}}[x, y]$ in the xy-plane of the chip. One without atoms but with imaging light ($I_{\text{ref}}[x, y]$) and one without light ($I_{\text{bkg}}[x, y]$). The laser beam propagates along the z-direction where x,y and z from a orthogonal coordinate system. The theoretical intensity on the chip with beam and atoms is given by

$$I[x, y] = I_0[x, y] \exp[-\text{OD}[x, y]] \text{ with } \text{OD}[x, y] = \tilde{\sigma} \cdot n_{\text{2D}}[x, y] \tag{2.10}$$

$I_0[x, y]$ is the intensity without atoms but only with the imaging beam. The scattering cross section $\tilde{\sigma}$ depends on the atomic resonance frequency, the light frequency (and linewidth) and on the intensity[2] [34]. $n_{\text{2D}}[x, y] = \int_{-\infty}^{\infty} n[x, y, z]dz$ is the two dimensional column density, where $n[x, y, z]$ is the real atomic density. OD is called optical density and is experimentally given by

$$\text{OD}[x, y] = -\ln\left[\frac{I_{\text{atoms}}[x, y] - I_{\text{bkg}}[x, y]}{I_{\text{ref}}[x, y] - I_{\text{bkg}}[x, y]}\right] \tag{2.11}$$

The number of atoms imaged is now

$$N = \text{const} \int_{-\infty}^{\infty} \int_{-\infty}^{\infty} \text{OD}[x, y]dxdy \tag{2.12}$$

with const being a constant (if effects of saturation can be neglected) which depends on $\tilde{\sigma}$ and the length calibration of the camera [33].
In conclusion the integrated optical density OD gives a measure for the imaged atom number. Our only way in extracting information from the system is processing the optical density. Since the used imaging method is destructive a new condensate has to be prepared for each image.

[2] If the laser power stays well below the saturation intensity, the intensity dependence can be neglected.

2.3 Rabi Pulses, Stern-Gerlach Method and Visibility Measure

The tools provided in this section are a little more specific to our experiments. The transfer of atoms in one atomic state to another one is treated. Then the question arises of how to distinguish these two states on the recorded image after TOF. Finally the visibility measurement is discussed which is a specific technique for lattice experiments.

2.3.1 Rabi Pulses

Experimentally we are at the point where we want to have two atomic ^{87}Rb species in our BEC. Therefore we want to transfer a certain fraction of the species (= hyperfine state) we start with ($|1\rangle$), to another atomic state which is then labeled as the second species ($|2\rangle$). This can be done by applying a microwave Rabi pulse of certain length and strength to the atoms of the first species.
The theory behind this problem was introduced by Rabi [35] and is included in many textbooks (e.g. [4]). Having a driving electro-magnetic field with frequency ω_l which has a much narrower linewidth than the atomic transition (which is characterized by ω_t) that it drives, it is possible to consider the system as a two level one. This can be done as long as the detuning $\Delta = \omega_\mathrm{l} - \omega_\mathrm{t}$ is small enough that coupling to other existing atomic levels does not become important. The Hamiltonian of the system can then be truncated. After some algebra and approximations, two coupled differential equations remain [4]. Solving these equations leads to the time dependent populations P_1 (population of 1st species) and P_2 (population of 2nd species)

$$P_2 = \left(\frac{\Omega}{\Omega'}\right)^2 \sin^2\left[\frac{\Omega'}{2}t\right] \quad \text{and} \quad P_1 = 1 - P_2 \tag{2.13}$$

$\Omega = E_0\langle 1|\mathrm{e}\mathbf{r}|2\rangle/\hbar$ is called the Rabi frequency, where E_0 is the electric field amplitude of the driving field. The dipole matrix element that is an important part of the Rabi frequency is taken between the atomic state of the 1st and 2nd species. $\Omega' = \sqrt{\Omega^2 + \Delta^2}$ is called the generalized Rabi frequency. eq. 2.13 shows that by applying a driving pulse which is close enough to the frequency of the desired transition to stay within the limits of the approximations used, one can get arbitrary mixtures between the species. The pulse just has to be turned off at the right time. It has to be pointed out that directly after applying

the pulse, each of the atoms is in a coherent superposition[3] between $|1\rangle$ and $|2\rangle$. Imaging the atoms however projects the states out and a population distribution in agreement with eq. 2.13 can be measured.
This technique can now be applied to transfer atoms from one to another atomic state. However it can happen that the transition frequency between the states depends crucially on magnetic fields (Zeeman effect). A change of the magnetic field or unwanted gradients therefore lead to experimental issues. A solution to this is to apply a so called Landau-Zener sweep [36–38]. This technique is much less sensitive to small changes in the magnetic field or inhomogeneities over the extension of the atom cloud because the frequency of the driving field is swept over the resonance with a certain constant speed. By varying the sweep speed and the power of the driving frequency, the population transfer can be adjusted.

2.3.2 Stern-Gerlach Method

The Zeeman effect can now be used to separate atoms in atomic states with different magnetic moments. For weak[4] magnetic fields, the energy offset of an atom in a state with the magnetic quantum number m_F and the g-factor g_F (values for ^{87}Rb see Fig 3.1) is [39]

$$E = m_F g_F \mu_\mathrm{B} B_0 \tag{2.14}$$

where μ_B is the Bohr magneton and B_0 the amplitude of the magnetic field. Applying an inhomogeneous magnetic field, atoms with different magnetic moments will separate. This is the idea of a Stern-Gerlach pulse where a magnetic gradient field is pulsed on for a short time to have separated species when the image is taken after a certain TOF [40, 41]. Fig. 2.1 shows the separation of the species after applying a magnetic gradient pulse. Note that the magnetic moment of $|\mathrm{F} = 2, \mathrm{m_F} = -2\rangle$ is twice as big as the one of $|\mathrm{F} = 1, \mathrm{m_F} = -1\rangle$. This can be seen by the seperation in Fig. 2.1.

2.3.3 Visibility Measurement

In the context of quantum gases in optical lattices, interference effects will be measured (see Fig. 5.4). In order to quantify the degree of coherence of the system that leads to the interference, a measure has to be defined. Fig. 2.2 shows two absorbtion images which illustrates our definition of visibility. The

[3] For an integer π-pulse pure states are obtained.

[4] Weak means that the splitting of the states due to the field is small compared to the fine structure spitting.

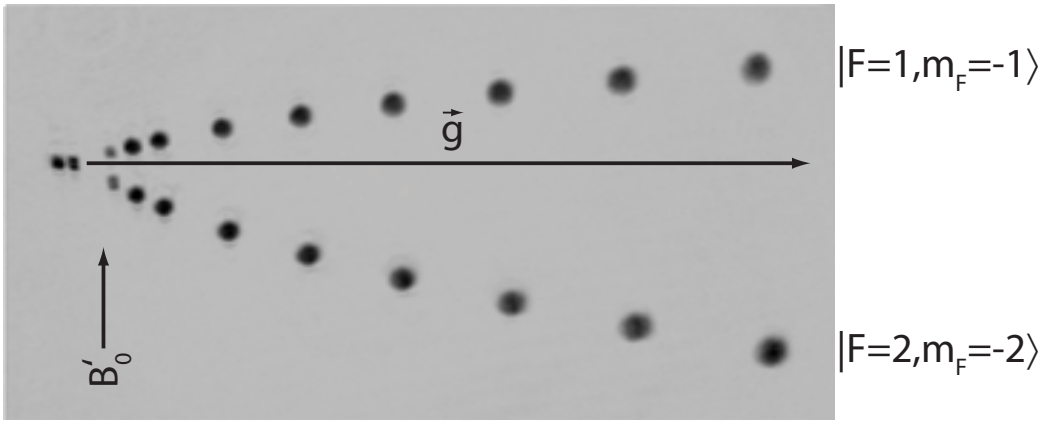

Figure 2.1: Stern-Gerlach pulse applied to ^{87}Rb atoms in the ground states $|\mathrm{F}=1,\mathrm{m_F}=-1\rangle$ and $|\mathrm{F}=2,\mathrm{m_F}=-2\rangle$ (compare to Fig. 3.1). The images are shown in a stroboscopic manner from TOF= 0 ms (left) to TOF= 14 ms (right). The direction of the strongest B-field gradient is indicated. The length of the Stern-Gerlach pulse was 4.5 ms.

left part of the figure shows a coherent scenario. Most of the atoms are in the interference peaks. In this case the visibility is close to 1 because the peaks can be seen and distinguished perfectly. The right part shows a case where the interference peaks cannot be seen in a very clear way. Here the visibility is closer to zero than to one.
For the definition of the visibility $\mathcal{V}$, we need the optical density OD from eq. 2.11. We define $\tilde{\mathrm{OD}}_{\mathrm{peak}}$ as the integrated OD that is enclosed by the four green solid circles in Fig. 2.2 and $\tilde{\mathrm{OD}}_{\mathrm{bkg}}$ as the one that is enclosed by the four red dotted circles. All circles have the same area.
The visibility is defined as [42]

$$\mathcal{V} = \frac{\tilde{\mathrm{OD}}_{\mathrm{peak}} - \tilde{\mathrm{OD}}_{\mathrm{bkg}}}{\tilde{\mathrm{OD}}_{\mathrm{peak}} + \tilde{\mathrm{OD}}_{\mathrm{bkg}}} \tag{2.15}$$

This definition fulfills the requirements given above and is a measure of coherence of the system[5]. The radii of the circles should be chosen such that all interference peaks of the most coherent image are a little bigger than the circles themselves (in the figure, the circles are therefore drawn to big). Of course once chosen, the radii remain constant.

[5]More about this in 5.2.

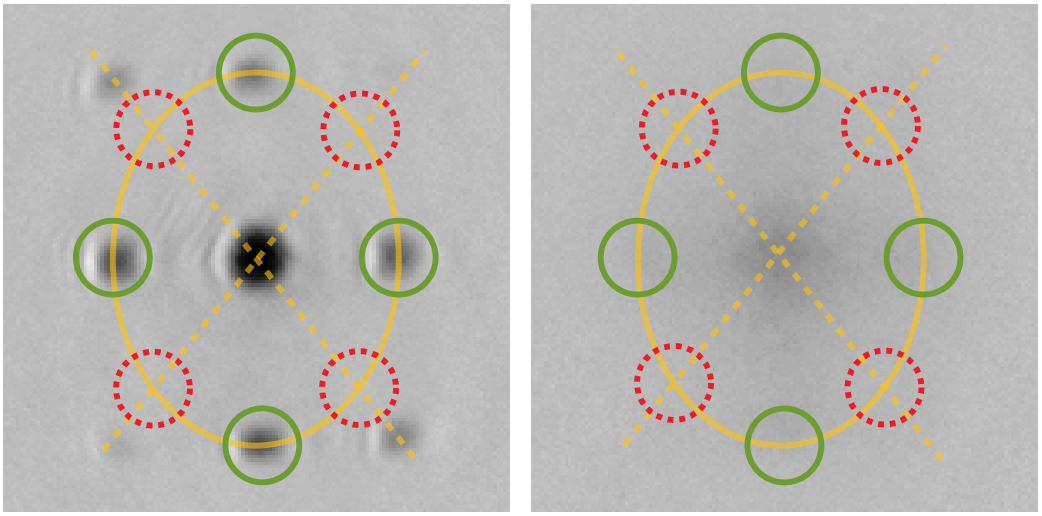

Figure 2.2: Definition of visibility. The left side shows a coherent case, while the right side shows a image that is less coherent and has smeared out interference peaks. The ellipse that connects the strongest peaks as well as the dotted gray lines are guides to the eye. The green solid circles are centered on the peaks while the red dotted ones lie on the ellipse and the diagonals.

Chapter 3

Experimental Basis

This chapter partially summarizes the work that has been done in earlier times in our group but is important as a basis for this thesis. Therefore the fundamental setup of the machine and how it produces a BEC, will be discussed. Detailed information can be found in [32, 33, 43, 44].

3.1 Laser System

Fig. 3.1 shows the ^{87}Rb energy level diagram with the relevant cooling and imaging structure.
The cycling transition, which is used for cooling, is operated by a DL pro 780 that is amplified by a BoosTA (see Fig. 3.2). The DL pro 780 and the DL 100[1], that is used for repumping are both external cavity diode lasers from Toptica. The BoosTA is a tapered amplifier that amplifies 65 mW from the DL pro to 700 mW.
For laser cooling generally, a closed transition is needed which means that the atoms cycle between the two chosen levels (here F=2 and F=3) but do not escape to other levels. However there is a small probability that an atom escapes and ends up in the F=1 ground state. To get these atoms back into the cooling cycle, the repump beam is used. For a detailed discussion of laser cooling see [4]. The purpose of the depump beam is to transfer atoms from the F=2 to the F=1 ground state. For absorptive imaging a closed transition is preferred, too. Therefore the cycling light is used for imaging ($\sim$ 100 μs) while the repumper pumps F=1 atoms to the F=2 manifold at the same time. Both diode lasers are frequency stabilized by a PID loop that uses a signal from ^{87}Rb polarization saturation spectroscopy as reference [33, 46]. The desired frequency is generated with acousto-optic modulators (AOM [47]).

[1] not shown in Fig. 3.2 but in [33]

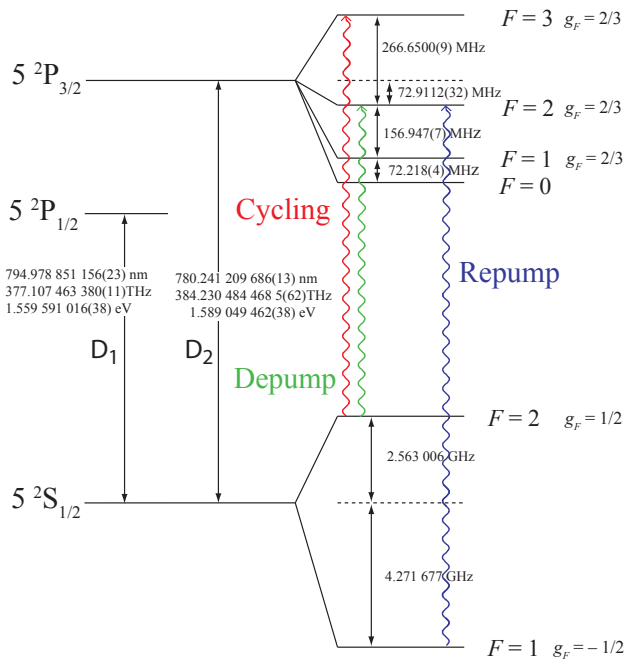

Figure 3.1: ^{87}Rb level scheme with experimentally relevant fine and hyperfine splitting. The data are taken from [45].

These devices are also used for modulating the intensity of the beams and as shutters (see Fig. 4.5).
Fig. 3.2 furthermore shows the laser system that is used for creating the state-dependent optical lattice along the z-direction (see Fig. 4.13). This system consists of a 899-21 Titanium:Sapphire Ring Laser which is pumped by a Verdi V-10. The Verdi V-10 is a diode-pumped, frequency-doubled solid state laser. The wavelength of the ring laser can be adjusted between 700 - 825 nm [48]. The properties of this system are discussed in [49]. Appendix A shows that the linewidth of the ring laser, at the used wavelength of 785 nm, is good enough for a lattice experiment. For this system, the use of an AOM as an intensity modulator can be seen in Fig 3.2.
The same principle is used to control the intensity of the crossed optical dipole trap and the state independent 1064 nm lattice (see 4.2 and 4.3). The 1064 laser light is produced by an IPG fiber laser (IPG YRL LP-SF series) with maximum output of 20 W and a linewidth of 50 kHz (not shown in Fig. 3.2).

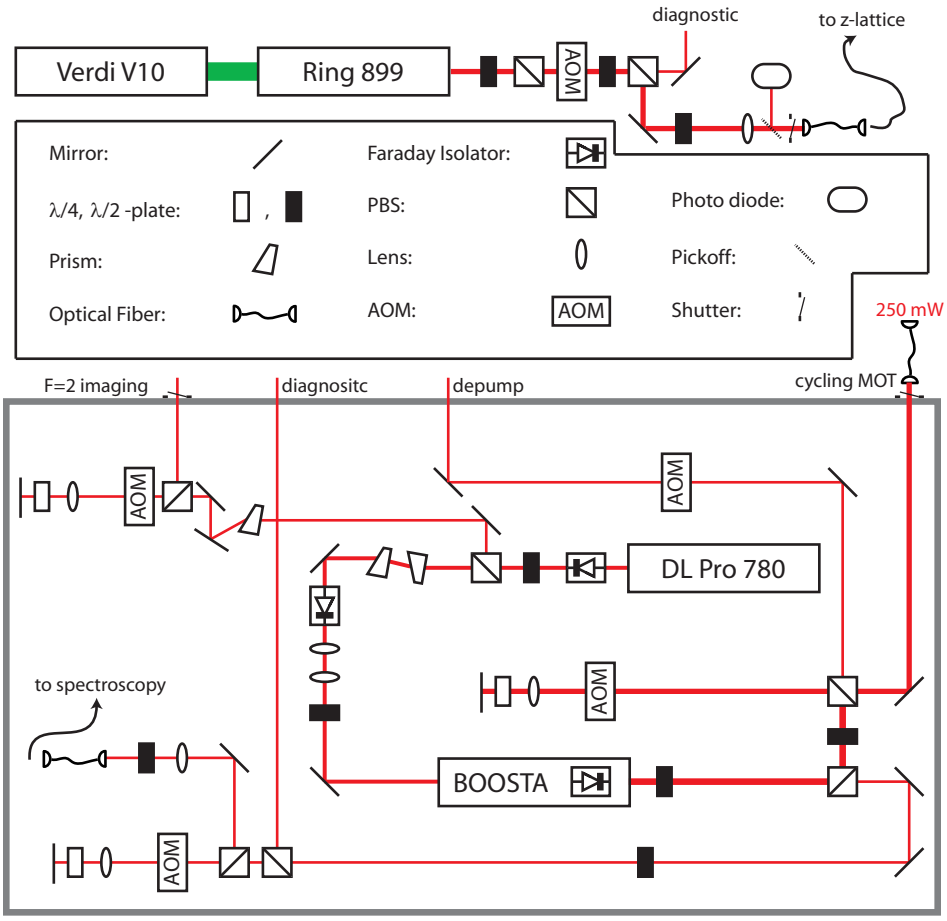

Figure 3.2: Setup of new cycling and lattice laser system. On the bottom of the figure the laser system for cycling and depumping is shown. The system is isolated by a box (gray in the picture). On the top of the figure, the laser system for the state-dependent lattice is shown.

3.2 Vacuum System, Quadrupole Coils and Transportation

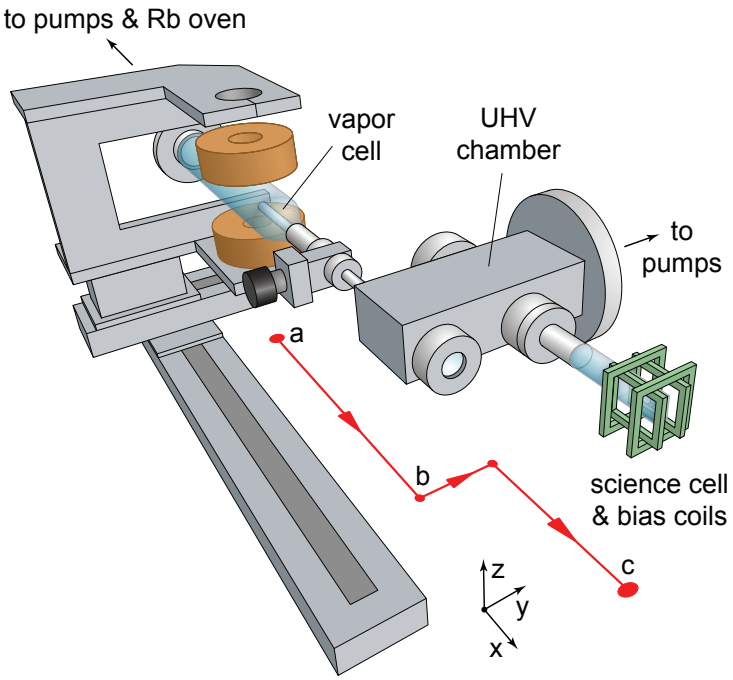

Figure 3.3: Transporter apparatus [44]. The figure shows the transporter apparatus and its path (red arrows) from the vapor to the science cell. The quadrupole coils are shown in the MOT (magneto-optical trap) position. Moving these coils, the cooled atom cloud can be transfered to the science cell. Around the science cell the bias coils can be seen. More coils (not shown here) exist that can be used to vary magnetic field amplitudes and gradients along different directions. The lab coordinate system is shown. Figure included with kind permission of D. Pertot.

The vacuum system is divided into a low and a high pressure region. Fig. 3.3 shows both regions.
In the vapor cell or MOT region the Rb background pressure is $\sim 10^{-9}$ torr which is necessary for loading the MOT. The atoms get into the vapor cell from a rubidium oven that can be opened and closed manually (not shown in figure). In this high pressure region, the atoms are confined by the magnetic potential (physical principle: eq. 2.14) of quadrupole coils in anti-Helmholtz configuration. About 10^{10} atoms are cooled by a standard ^{87}Rb MOT. The principle of laser cooling is based on a dissipative interaction between light

and atoms which means that photons scatter (see 4.1). This causes a net momentum transfer to the atoms which cools them down to, in our case, 25 μK. In the end the atoms are optically pumped into the $|\mathrm{F} = 1, \mathrm{m_F} = -1\rangle$ ground state and the field gradient along the z-direction is increased to stiffen the trap prior to transport.
The atom cloud is then quickly moved to the ultra-high vacuum region in the science cell. This is done by the quadrupole coils which are mounted to the mechanical transporter. The pressure in the science cell is $< 10^{-11}$ torr and achieved by an ion pump combined with a Ti sublimation pump. The two pressure regions are connected by a differential pumping tube. The transport from the MOT region to the science cell happens in 3 s. It must be this fast because the high pressure in the MOT region strongly decreases the lifetime of the atom cloud. During the transport, the cloud is compressed by a further increase of the magnetic field gradient along the z-direction to 350 G/cm.

3.3 Production of Bose-Einstein Condensates

The stiff linear potential of the quadrupole trap only contains atoms in the hyperfine ground state $|\mathrm{F} = 1, \mathrm{m_F} = -1\rangle$. Atoms with a non-negative magnetic quantum number are not trapped. The atoms are now cooled further by applying a 14 s long radio frequency (RF) ramp, linearly sweeping from higher to lower frequencies. The principle here is called evaporative cooling: the atoms with high temperatures can travel to regions of high magnetic fields (see eq. 2.14). In these regions the RF drives transitions to magnetically non-trapped states and the atoms with high thermal energies are removed from the trap. Since the RF sweep is slow enough to allow for thermalization (elastic two body collisions) the cloud becomes colder. At cold temperatures (here 75 μK) a problem occurs [50]. The atoms amplified (compared to higher temperatures) undergo Majorana losses which means that their magnetic quantum number flips near the center of the trap where the magnetic field is zero. This problem is solved by introducing homogeneous bias field coils (see Fig. 3.3). These coils produce a rotating bias field in the xy-plane which is added to the quadrupole field of the moving coils. The result is that the atoms see a time-averaged harmonic potential without a field zero. This kind of trap is called a time-averaged orbiting potential trap (TOP trap). Therefore Majorana losses do not appear. With this configuration, we can go on with RF evaporation untill the cloud has a temperature of ~ 250 nK.
At this temperature we transfer the atoms into the crossed optical dipole trap (XODT) (see Fig. 4.5) by smoothly ramping up the XODT potential and then smoothly ramping down the magnetic confinement which together takes

$\sim$ 1s. Then the XODT potential is lowered to force evaporative cooling until a nearly pure ^{87}Rb BEC with $\sim 10^5$ atoms in the $|\mathrm{F}=1,\mathrm{m_F}=-1\rangle$ ground state is produced. Whenever we refer to the XODT in the following text, we mean this all-optical potential which contains the BEC.
One advantage of our machine is the possibility to move the quadrupole coils away from the science cell after loading the XODT. This guarantees good optical access. The production time for on BEC is about one minute. Both reproducibility in atom number and in position are discussed in detail in [44].

Chapter 4

Trapping and Manipulating Quantum Gases with Laser Beams

Laser light exerts two fundamental forces on atoms. One has a dispersive nature and is called the optical dipole force which can form a conservative trap for the atoms. The second part of the atom-light interaction is of absorptive nature and is dissipative. This radiation force leads to a scattering of photons. For trapping quantum gases the dipole force is widely used, whereas the radiation force is to be avoided, since it causes heating and minimizes the lifetime of the trapped atoms.
The use of the dipole force for trapping atoms in a 1-D standing light wave was suggested by Letokhov in 1968 [51]. In 1986 Chu *et al.* [52] reported the first experimental success in optically trapping atoms, where the sodium atoms were not confined in a standing light wave but by a strongly focused Gaussian "one-way" beam.
This chapter introduces the theoretical basis for understanding the radiation and dipole force. In addition we describe our optical trap, optical lattices in general, and state-dependent optical lattices in particular. This discussions forms the main part of the chapter.

4.1 The Dipole and the Radiation Force

The semi-classical Lorentz model [53] describes the electron as an oscillator in the electric light field. This light field induces an electric dipole moment at the atom

$$\mathbf{p} = \alpha \mathbf{E} \tag{4.1}$$

where $\mathbf{E}$ is the real and time dependent electric field at the place of the atom and α is the complex polarizability. The induced dipole moment leads directly to the dipole potential

$$U_{\mathrm{dipole}} = -\frac{1}{2}\langle \mathrm{Re}(\mathbf{p})\mathbf{E}\rangle = -\frac{1}{2\epsilon_0 \mathrm{c}}\mathrm{Re}(\alpha) I \tag{4.2}$$

The brackets in eq. 4.2 indicate the time average over the fast oscillating electric field. Furthermore the relation between the electric field amplitude and the intensity $I = \frac{1}{2}\epsilon_0 \mathrm{c} {E_0}^2$ has been used. From the equation one can see that the only spatial part that could be used for trapping the atoms inside U_{dipole} is induced by the intensity. Therefore the gradient of the light intensity is directly connected to the attracting or repelling force that acts on the atoms. To gain deeper insight into the dipole potential, the polarizability α needs to be calculated. This can be done classically by solving [34] the damped equation of motion of the vibrating electron that is driven by the light field:

$$\alpha = 6\pi\epsilon_0 \mathrm{c}^3 \frac{\Gamma_\mathrm{t}/{\omega_\mathrm{t}}^2}{{\omega_\mathrm{t}}^2 - {\omega_\mathrm{l}}^2 - \mathrm{i}\Gamma_\mathrm{t}{\omega_\mathrm{l}}^3/{\omega_\mathrm{t}}^2} \tag{4.3}$$

with ω_l being the frequency of the light and ω_t as the transition frequency of the atom that is considered. eq. 4.3 holds for large detuning (no saturation). To obtain a proper quantum mechanical description, the damping rate (=spontaneous decay rate) has to be described as [11]

$$\Gamma_\mathrm{t} = \frac{{\omega_\mathrm{t}}^3}{3\pi\epsilon_0 \hbar \mathrm{c}^3} |\langle n_\mathrm{t}|\mathrm{e}\mathbf{r}|m\rangle|^2 \tag{4.4}$$

where the dipole matrix element is taken between the ground state $|m\rangle$ and the excited state $|n_\mathrm{t}\rangle$ with respect to the specific atomic transition. For not too small detunings eq. 4.2 and 4.3 lead in a very good approximation to

$$U_{\mathrm{dipole,t}} = \frac{3\pi \mathrm{c}^2}{2{\omega_\mathrm{t}}^3}\left(\frac{\Gamma_\mathrm{t}}{\omega_\mathrm{l} - \omega_\mathrm{t}} - \frac{\Gamma_\mathrm{t}}{\omega_\mathrm{l} + \omega_\mathrm{t}}\right) I \tag{4.5}$$

Fig. 4.1 shows that the error introduced by using the approximation that leads to eq. 4.5 is insignificant, as long as the laser is not operated very close to an atomic resonance. At resonance, or for too high intensities, saturation occurs which makes the above equations invalid. These cases however do not eventuate for our experiments.

The polarizability also relates to the scattering rate that gives the number of scattered photons per unit time. An expression for this rate can be derived by

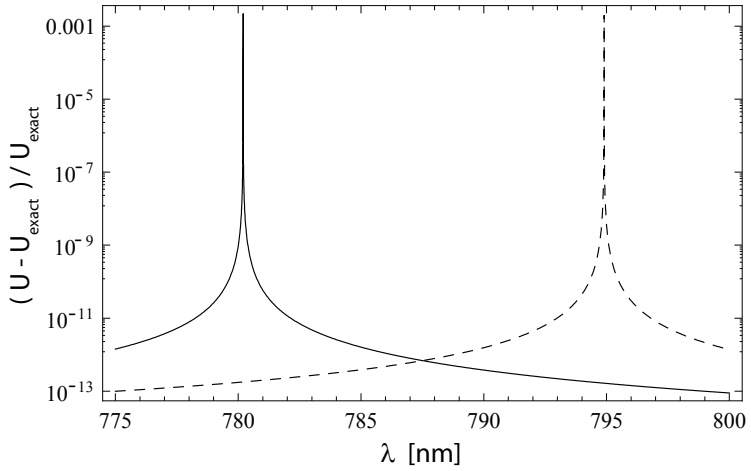

Figure 4.1: Plot of $\frac{U_{\mathrm{dipole,t}}-U_{\mathrm{exact}}}{U_{\mathrm{exact}}}$ with respect to the laser wavelength λ. U_{exact} is the potential for ^{87}Rb that can be calculated from eq. 4.2 and 4.3 without any approximation. The solid curve corresponds to the D_2, the dashed curve to the D_1 transition. The hyperfine splitting is not taken into account (2x two level atom). Data for calculation are taken from [45].

dividing the power the dipole absorbs from the light field (and emits again) by the energy of the corresponding photon of the light field [11]

$$\Gamma_{\mathrm{scatt}} = \frac{P}{\hbar\omega_{\mathrm{l}}} = \frac{\omega_{\mathrm{l}}\mathrm{Im}(\alpha)I/(\epsilon_0 \mathrm{c})}{\hbar\omega_{\mathrm{l}}} = \frac{1}{\epsilon_0 \mathrm{c}\hbar}\mathrm{Im}(\alpha)I \tag{4.6}$$

Now again eq. 4.3 is used for the imaginary part of α. Performing a similar approximation as used for eq. 4.5

$$\Gamma_{\mathrm{scatt,t}} = \frac{3\pi \mathrm{c}^2}{2\hbar}\frac{{\omega_{\mathrm{l}}}^3}{{\omega_{\mathrm{t}}}^6}\left(\frac{\Gamma_{\mathrm{t}}}{\omega_{\mathrm{l}}-\omega_{\mathrm{t}}} - \frac{\Gamma_{\mathrm{t}}}{\omega_{\mathrm{l}}+\omega_{\mathrm{t}}}\right)^2 I \tag{4.7}$$

is achieved. The area in which $\Gamma_{\mathrm{scatt,t}}$ is valid follows the same restrictions as those for the dipole potential. The force that is connected to the scattering rate is caused by the photon recoil momentum $\hbar\mathbf{k}$ of the laser light field.
A deeper discussion on both the dispersive and the absorptive force can be found in [11]. The dipole potential can also be derived using the dressed atom approach which gives an intuitive understanding due to energy shifts of the eigenstates of the atom-light Hamiltonian (dressed state picture)[54].

4.2 Red-Detuned Crossed Dipole Trap

To get a qualitative impression that often is important for understanding experiments, eq. 4.5 and 4.7 can be considered for a simple 2-state atom. Furthermore the so called rotating wave approximation (RWA) that sets ω_l/ω_t to 1 (only for the fraction in eq. 4.7) and neglects the terms containing $\omega_l + \omega_t$ can be applied. This approximation is valid for rather small detunings but even for larger detunings - in our case resonances for ^{87}Rb at about 795 and 780 nm, laser at 1064 nm - the discrepancy is only on the order of a few percent. eq. 4.5 and 4.7 become

$$U_{\text{dipole,RWA}} = \frac{3\pi c^2}{2{\omega_t}^3}\left(\frac{\Gamma_t}{\Delta}\right) I \quad \text{and} \quad \Gamma_{\text{scatt,RWA}} = \frac{3\pi c^2}{2\hbar{\omega_t}^3}\left(\frac{\Gamma_t}{\Delta}\right)^2 I \tag{4.8}$$

with $\Delta = \omega_l - \omega_t$. Equ 4.8 shows two important physical features of dipole traps and optical lattices. First the dipole potential is attractive for red-detuning ($\Delta < 0$) and repulsive for blue one ($\Delta > 0$). Second large detuning is needed to minimize the scattering rate which destroys the coherence. But since Δ goes linearly into the potential and quadratically into the scattering rate, the former one is less affected by a growing detuning than the latter. Therefore high intensities in combination with large detunings can be used to minimize the scattering rate without significantly affecting the potential.
Eq. 4.8 suggests trapping the ultra cold atoms in the intensity maximum of a far red detuned laser beam. For the sake of completeness it should be mentioned that blue-detuned traps can be used, too. Here the atoms are trapped in the dark by a repulsive force. The advantage of the blue-detuned dipole trap is the further reduction of the scattering rate. For a review on blue dipole traps, see for example [55].

4.2.1 Theoretical Description of Crossed Optical Dipole Trap

In our case however a red detuned trap is implemented. It will turn out that a TOP trap as described in 3.3 is not usable for our experiments because its potential strongly depends on the hyperfine state of the atoms (see eq. 2.14). Furthermore micromotion of the atoms in the TOP trap might cause problems [56].
The crossed optical dipole trap (XODT) does not have these drawbacks. It

is formed by two crossed[1] Gaussian laser beams. Each beam forms an optical dipole trap (ODT) and is labeled with 1 or 2, respectively (see Fig. 4.5). The intensity of such one beam is described by

$$I[r,z] = \frac{2P}{\pi w^2[z]} \exp\left[\frac{-2r^2}{w^2[z]}\right] \quad \text{with} \quad w[z] = w_0\sqrt{1+(z/z_R)^2} \tag{4.9}$$

The laser beam propagates along the z-direction and shows a radial symmetry. $w[z]$ is the $1/e^2$-radius of the beam and has its minimum w_0 at $z = 0$. w_0 is commonly called the (smallest) beam waist. $z_R = \pi {w_0}^2/\lambda$ is named the Rayleigh range. It describes how fast the beam diverges. The power of the beam P is related to the peak intensity $I_0 \equiv I[0,0]$ by

$$I_0 = \frac{2P}{\pi {w_0}^2} \tag{4.10}$$

A Gaussian laser beam is therefore fully characterized by its power, wavelength, propagation direction, waist minimum w_0 and location of w_0.

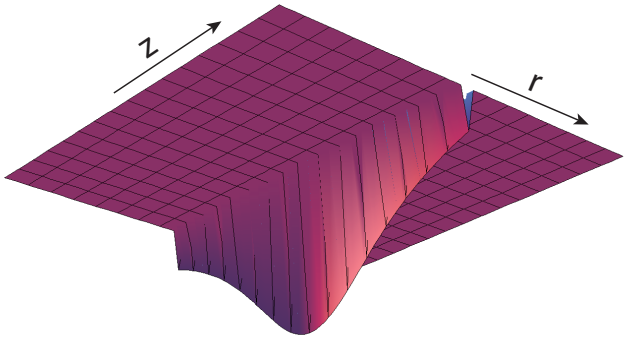

Figure 4.2: Plot of Dipole potential for a 1064 nm beam with a smallest waist w_0=140 μm. The radial and the axial scale is the same. The ultra cold ^{87}Rb atoms are trapped at the minimum of the potential. The gravitational potential is not considered.

Fig. 4.2 shows a typical (far red-detuned) optical dipole trap as it is used in the experiment. Since the spatial axes of the plot have the same scale it becomes clear that the axial confinement is much weaker than the radial one. This is one of the reasons why a crossed optical dipole trap is used. The beams of the XODT cross at their smallest waists. For smallest waists of the

[1]Crossing angle = 90°; the normal vector of the plane formed by the crossing beams is parallel to the gravitational force, see Fig. 4.5.

same size and the right power (to compensate the gravitational potential) a confinement with approximately equal trap frequencies in all three directions can be achieved.

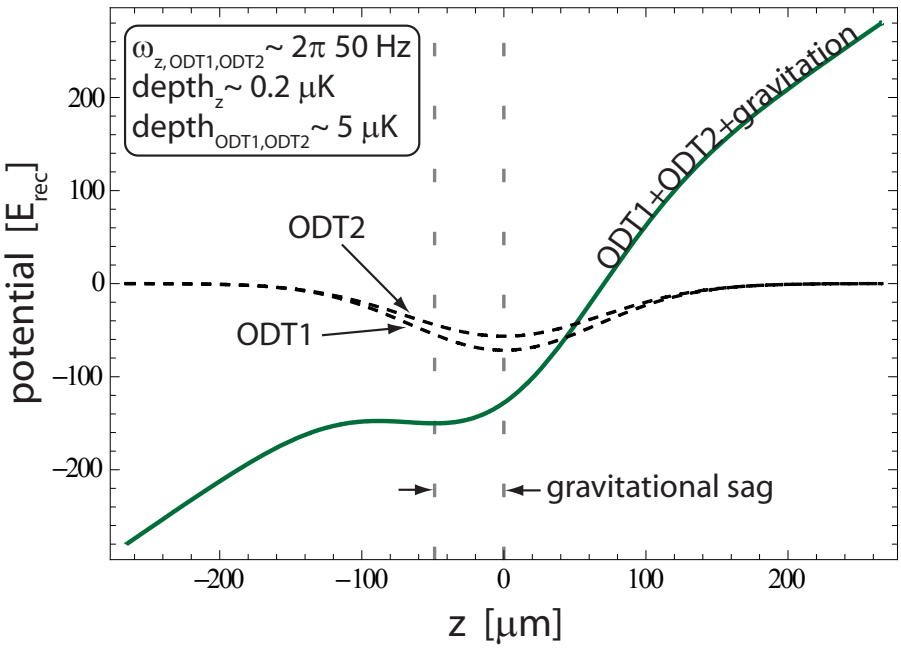

Figure 4.3: Plot of 1064 nm XODT dipole potential for ^{87}Rb with gravitation (solid line) with smallest waists $w_0 = 135,\ 141\ \mu$m and power $P = 1.27,\ 1.08$ W for ODT1, ODT2-beam. The dashed curves show the ODT1 and ODT2 potentials without gravitation. The horizontal axis points along the gravitational force. The gray dashed lines indicate the minimum of the dipole potential with and without gravitation, respectively. The energy is measured in units of the recoil energy $E_{\mathrm{rec}} = (\hbar k)^2/(2m)$. k is the absolute value of the wave vector of the light used and m is the mass of one atom.

Fig. 4.3 shows the dipole potential of the XODT with parameters typical for our experiment. Comparing the dotted vertical lines in the plot the effect of gravitation can be seen: it lowers the equilibrium position of the trap. The potential is calculated for ^{87}Rb atoms in the hyperfine ground state $|\mathrm{F} = 1, \mathrm{m_F} = -1\rangle$. This is done by using eq. 4.5 and performing the sum $\sum_{\mathrm{t}} U_{\mathrm{dipole,t}}$ by summing over all excited D1 and D2 states of ^{87}Rb. The dipole matrix element of eq. 4.4 is evaluated by calculating the particular Clebsch-Gordan coefficients as suggested in [45]. These matrix elements depend on the polarization of the laser light. The plot shows the potentials for π-polarized light which are only slightly different from σ^+ or σ^- light potentials. Further-

more the trap is not state-dependent and therefore traps any hyperfine ground state without significant discrepancy. This is because the hyperfine structure is not resolved, due to the large detuning of the XODT. Therefore the exact summation which has been performed for the XODT could be reduced to the two-level case without a significant error[2].
Finding the minimum of the three-dimensional XODT potential and expanding the potential around this minimum to the second polynomial order, the trap frequencies in the directions of ODT1, ODT2 and z can be found. It turns out that the angular trap frequencies are on the order of $2\pi\times50$ Hz for all three directions. The depth of the trap is a few μK in the ODT1 and ODT2 directions and some hundreds of nK in the z direction. A more accurate specification on the basis of a calculation cannot be given, since all the above parameters depend sensitively on the smallest waists and the power of the beams. The smallest waists especially cannot be measured to a higher accuracy at the required position. Furthermore a misalignment of the beams may change the parameters of the trap.
Using eq. 4.7 and performing the sum $\sum_{\mathrm{t}} \Gamma_{\mathrm{scatt,t}}$ in the same way as described for the XODT potential, the scattering rate can be obtained. Since the BEC is located at the trap minimum the potential with gravitation (solid line in Fig. 4.3) has to be considered for a reference point. The calculation shows that the scattering rate at this point is on the order of 10^{-2} s^{-1}. This value includes a reduction of scattering by 1/3 compared to the XODT potential without gravitation, since the atoms are not sitting at the intensity maximum of the Gaussian ODT1 and ODT2 beams when gravitation is considered. The argument for the 1064 nm scattering rate is the same as for the 1064 nm potential. Hence it is neither sensitive to the polarization of the trap light nor to the trapped atomic state. A scattering rate of $\sim 10^{-2}$ s^{-1} is very low and therefore sets the lifetime of the ultra cold atoms in the trap to a high value, which is experimentally favorable.

4.2.2 Measurement of XODT Trap Frequencies

The values of the trap frequencies need to be known to determine the equilibrium properties of the BEC such as the Thomas-Fermi radius (see 2.1.2). Experimentally the XODT trap frequencies can be measured by kicking the condensate, letting it evolve freely in the trap, switching off the trap after a certain but variable holdtime and taking a picture of the atom cloud after a fixed TOF. The displacement of the BEC from its equilibrium position (without kick) gives the velocity of the BEC at the time when the trap was switched

[2]This cannot be done for the state-dependent potentials which will be discussed later.

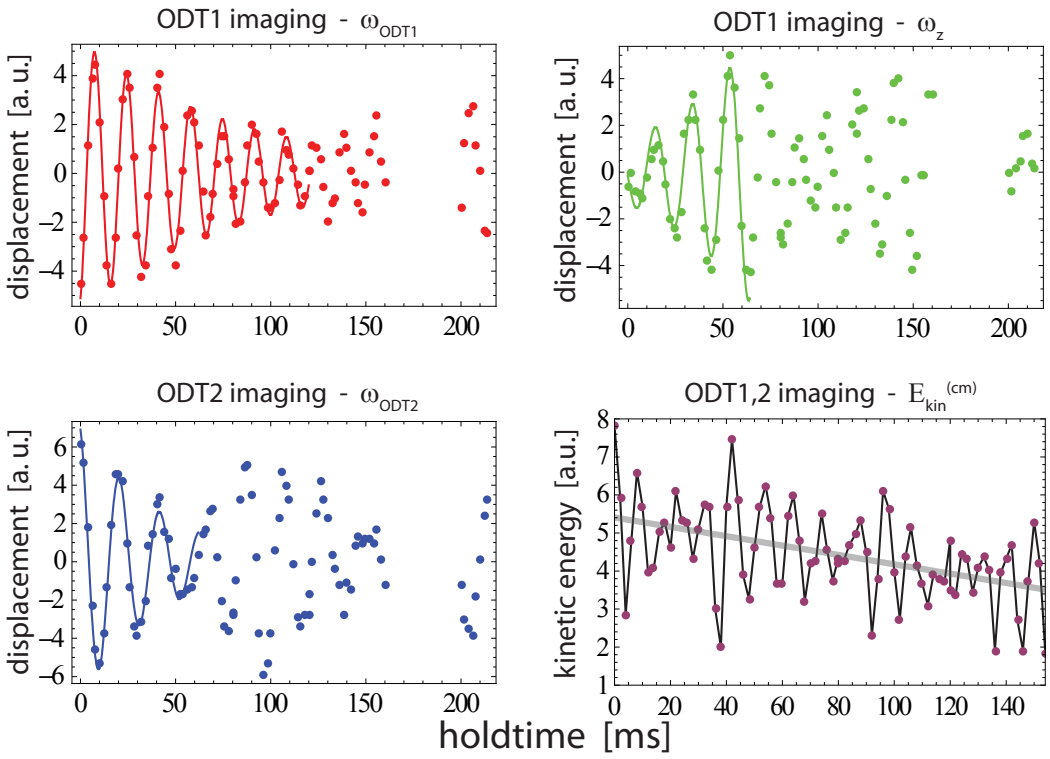

Figure 4.4: XODT trap frequencies. The plots show the time evolution of the kicked BEC in XODT trap. The data of ODT1-imaging ω_{ODT1} and ODT2-imaging are fitted by a function $A\exp[\gamma t]\sin[\omega t+\phi]$ with A, γ, ω and ϕ as free parameters. All shown fits are best fits with respect to the data which lie in the time interval of the extension of each plotted fit function. All the data are taken after a TOF of 12 ms. The plot in the lower right corner shows the center of mass kinetic energy $E_{\mathrm{kin}}^{(\mathrm{cm})}$ of the BEC cloud. It can be seen that $E_{\mathrm{kin}}^{(\mathrm{cm})}$ decreases with time as indicated by the gray linear fit.

off. Assuming a harmonic trap, one can easily find the trap frequencies by taking pictures of the condensate for different holdtimes. In our case the BEC is kicked by applying a short magnetic pulse with the quadrupole coils (see Fig. 3.3) which are ∼10 cm away from the science cell. This leads to a force mainly along the x-direction (compare Fig. 4.5). Fig. 4.4 shows the displacement of the cloud as a function of the holdtime. The position of the cloud is found by applying a Gauss fit to the data. Table 4.1 shows the frequencies and the damping constants of the XODT. Fig. 4.4 reveals two qualitative behaviors. First a general damping can be seen. All the oscillations tend to zero for very long times. This could be explained by a disorder of the dipole potential that forms the XODT [57]. This disorder (small kinks in the transverse Gaussian distributions) could be caused by dirt on the optics that are used to form the XODT. An explanation which is more likely is that atoms with high energies fall out of the trap because a clear decrease in atom number for longer hold times can be seen by summing over the optical densities (see 2.2) of the TOF images. On the other hand this decrease is possibly caused by the normal decrease of the atom number over time. Another option that has been checked is energy transfer to shape oscillations of the cloud. These oscillations can clearly be seen but they also decrease with time without any interesting behavior like coupling between different directions or revivals. In the end, it is not clear where the energy that disappears in the center of mass frame, occurs again. A mixture between the suggested mechanisms is likely.

	ODT1	ODT2	z
$\omega/(2\pi)$ [Hz]	59.2 ± 1.0	46.9 ± 2.0	51.1 ± 1.5
γ [s^{-1}]	-11.8 ± 1.0	-24.6 ± 3.7	21.5 ± 3.0

Table 4.1: XODT trap frequencies and decay constants. The errors of the trap frequencies are estimated for different possible best fits in the time intervall from 0 to 60 ms (see Fig. 4.4). The decay constants belong to the fits shown in Fig. 4.4 and are given with the corresponding best fit errors. ω_{ODT1} is the frequency of the oscillation along the ODT2 direction, and vice versa. ω_{z} is the frequency of the oscillation along the z-direction.

The second interesting observation that can be made is that there seems to be a strong coupling between the z-oscillation and the ODT2-oscillation. Considering these two signals for times smaller than 50 ms one sees a clear increase in the amplitude of the ω_{z}-signal whereas the ω_{ODT2}-signal decays. The ODT1 and ODT2 imaging[3] data are taken at the same time by dual imaging. The decay constants of the ω_{ODT1} and ω_{z}-signal are well agreeable (see Table 4.1)

[3]The imaging along ODT1 and ODT2 works with the same principle as shown in Fig.

which suggests that the main energy transfer happens from the ω_{ODT2} to the ω_{z}-signal. Furthermore it can be seen that the ω_{ODT2}-signal peaks around 100 ms wheres the ω_{z}-signal has a local minimum at this time. This strong coupling indicates an anharmonicity of the trap.
It has to be mentioned that the trap frequencies of the XODT depend on the polarization of the beams only because the polarization changes the transmitted power through the glass cell. This measurement was taken after changing the polarization of the ODT2 beam and realigning the trap (only ODT2 beam). This was done in order to avoid interferences of the ODT2 beam with the science cell that could change the beam profile. Now the polarizations of ODT1 and ODT2 are parallel. Cross interferences between the beams, however, do not happen since the two beams are detuned by 20 MHz with respect to each other.
In conclusion the measured trap frequencies match up well with the calculated ones (see Fig. 4.3).

4.3 Optical Lattices

The physical principle that applies to an optical lattice (OL) is rather simple. A laser beam with wavelength λ is reflected back on itself by a fixed mirror, forming a standing light wave with a periodicity of $\lambda/2$ and a node at the surface of the mirror. Ultra cold atoms can now be trapped in the nodes (blue-detuned OL) or antinodes (red-detuned OL) due to the dipole force (see eq. 4.8). To insure that no phase shifts destroys the homogeneity of the 1-D lattice the coherence length of the light has to be larger than twice the distance of a point in the lattice to the surface of the mirror. This can easily be achieved since the linewiths of the lasers used in the experiment are all below 1 MHz which corresponds to a coherence length of 300 m. By superimposing additional 1-D lattices, one can create higher dimensional OL.
Standing light waves have been used to diffract atoms at an optical grating. Hereby the Kapitza-Dirac effect [58] and the well-known Bragg effect [59] have been probed. For an introduction to this topic see [60].
Fig. 4.5 shows the setup of the XODT and the OL in the xy-plane. The ODT1 and 2 beams are focused such that their smallest waists (135 μm for ODT1, 141 μm for ODT2) are located at the BEC position. Since the Rayleigh range of the beams is on the order of 5 cm the position of the mirrors does not have to be very accurate in order to assure a good overlap of the incoming and the reflected beams at BEC position. The switching between ODT and OL in the

4.13. The XODT is built with dichroic mirrors that transmit the imaging light. Therefore imaging along the XODT directions is possible (not shown in simplified setup of Fig. 4.5).

xy-plane is done using two AOMs for each beam. The first AOM puts the light in its first diffraction order and the second one in its minus first diffraction order. Going twice through this shutter, the frequency and propagation direction of the diffracted light is not changed. The advantage of this shutter is that it is fast ($\sim \mu$s) and has negligible leakage if closed. Furthermore the intensity of the reflected light can be varied by changing the power of the RF applied to the AOMs. This way it is possible, e.g., to ramp up the lattice adiabatically with respect to the trap frequencies. The two-way intensity efficiency of the AOM shutters is around 10%.

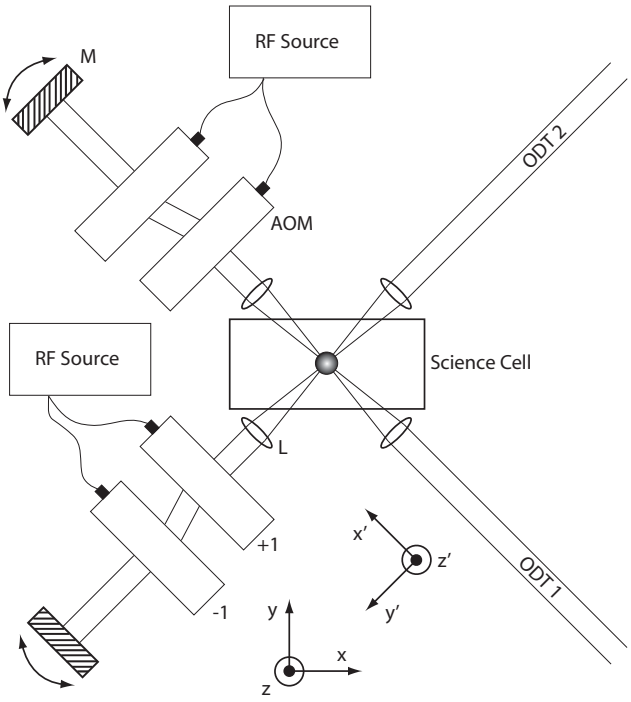

Figure 4.5: Setup of XODT (simplified) and OL. The two beams which act as dipole trap are retro reflected with mirrors (M) when the AOM-shutter is open. ODT1 and ODT2 then become OL1 and OL2. A third standing light wave along the z-direction (see Fig. 4.13) can be added. The wavelength of the beams is 1064 nm. All beams are focused on the BEC with lenses (L). The xyz-coordinate system is the lab coordinate system (compare to Fig 3.3). The gravitational force points along the negative z-direction. The x′y′z′-coordinate system is created by rotating the xyz-system by $(3/4)\pi$ where z′=z. The primed coordinate system is a natural choice for the XODT.

The two linearly polarized standing light waves are detuned from each other by 20 MHz[4]. This is done to avoid cross interferences between the beams. The two-way detuning minimizes the effect of cross interferences since the atoms cannot follow the rapid oscillations of the unwanted potential. To understand the potential that is formed by the standing light fields with wavelength λ, it is useful to consider the effect of one standing wave. For one plane standing wave the intensity which, is proportional to the potential (eq. 4.5), varies sinusoidally in the direction of propagation but is independent of the transverse directions. Therefore it forms a sheet of constant potential for every plane perpendicular to the propagation direction. Leaving out the symmetry breaking effect of gravitation the atoms would be confined in light sheets with a spacing of $\lambda/2$. Adding now a second standing wave with perpendicular propagation, the equipotential planes of the two fields cross and form 1D tubes of confinement that are parallel and in the order of a 2D square lattice. The potential sheets of a third beam (again perpendicular to the first and second one) would now cut the tubes and form a 3D simple cubic lattice with a lattice spacing of $\lambda/2$. The atoms are trapped at the points of the minimum potential which are the lattice sites. The potential formed by three standing plane waves is described as

$$V_{\mathrm{pw}}(x,y,z) = V_0 \sum_{i=x,y,z} \sin^2[k_i x] \tag{4.11}$$

In our case however the Gaussian beams are an overlying potential according to eq. 4.9 [61]

$$\begin{aligned} V_{\mathrm{G}}(x,y,z) &= V_x \exp\left[-2\frac{y^2+z^2}{w^2[x]}\right] \sin^2[k_x x] + \\ &\quad + V_y \exp\left[-2\frac{x^2+z^2}{w^2[y]}\right] \sin^2[k_y y] + \\ &\quad + V_z \exp\left[-2\frac{x^2+y^2}{w^2[z]}\right] \sin^2[k_z z] \end{aligned} \tag{4.12}$$

with $k_i = 2\pi/\lambda_i$. Here the possibility of different lattice periodicity along different axes is taken into account. This Gaussian confinement can be approximated harmonically at the position of the BEC (trap center). For deep lattices the potential of one lattice well at the trap center is well approximated by

[4]If a third 1064 nm beam along the z-direction is added, the beam is detuned by 10 MHz with respect to both XODT beams.

$$\omega_i = \sqrt{\frac{2V_i k^2}{m}} = \frac{k^2\hbar}{m}\sqrt{\frac{V_i}{\mathrm{E_{rec}}}} \tag{4.13}$$

4.3.1 Lattice Envelope and Lattice Ramp

In Fig. 4.3 the dipole potential for the XODT is shown. As discussed above the trap frequencies of this XODT are $\sim 2\pi\cdot 50$ Hz for a laser power of ~ 1 W and the known beam parameters. When a certain fraction of the beams is reflected back to form a standing light wave with the incoming beams the situation changes. Now there are small wells which are formed due to the standing wave and are equally spaced at the trap center. These small wells are enveloped by the Gaussian potentials described above.

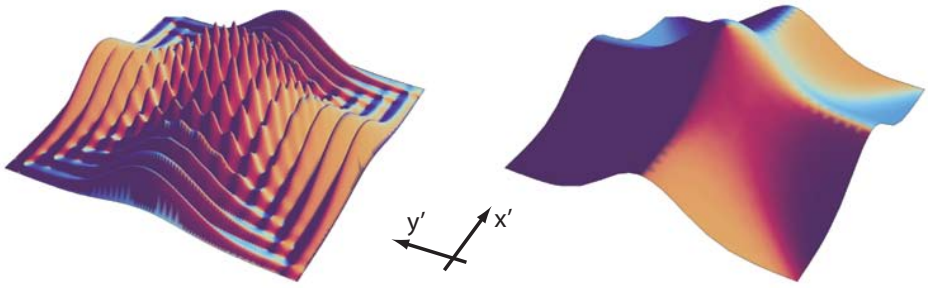

Figure 4.6: Standing wave potential of lattice beams along XODT directions and corresponding envelope for a constant z value. The beam waist is multiplied by a factor of 100 and the plots are flipped, both to make the structure of the potential clear.

Fig. 4.6 shows the potential of the OL1 and OL2 standing waves. If the potential were drawn to scale it would become clear that the envelope changes only slightly over the region in which the BEC is localized and that around 50^2 lattice sites extend over this region. To describe the situation adequately, the parameters of the envelope and the lattice sites (see eq. 4.12) have to be considered separately. First I will discuss the envelope of the OL1-OL2 2D lattice. The intensity distribution of the envelope is given by

$$I_{\mathrm{env}}[x,y,z] = I_{\mathrm{x}}(1 + R_{\mathrm{x}} + 2\sqrt{R_{\mathrm{x}}}) + I_{\mathrm{y}}(1 + R_{\mathrm{y}} + 2\sqrt{R_{\mathrm{y}}}) \tag{4.14}$$

where $I_{\mathrm{x,y}}$ describes the intensity of a Gaussian beam traveling in the **$\mathbf{x}'$ (Ol1) or $\mathbf{y}'$ (OL2)**-direction respectively, and is given by eq. 4.9 with r replaced by $\sqrt{\{y^2, x^2\} + z^2}$. The factors containing $R_{\mathrm{x,y}}$ occur due to interference of the

incoming and reflected beams in the x- and y-direction. As described above, no interference between the x- and y-beams must be taken in account. $R_{\mathrm{x,y}}$ is the intensity fraction which is reflected back to form the standing waves along the x- and y-axes. eq. 4.14 indicates that the envelope potential and therefore the envelope trap frequencies ω_{env} change as a function of $R_{\mathrm{x,y}}$. This can cause experimental problems when ramping up the lattice which means increasing $R_{\mathrm{x,y}}$.

The 1D ramp up of a lattice has been treated experimentally and theoretically [62, 63]. Increasing the lattice potential V_0 from 0 to 1 $\mathrm{E_{rec}}$ has to happen in a time bigger than the recoil time $\mathrm{m_{Rb}}\lambda^2/(\hbar\pi)$ [64] which is ~ 490 μs for 1064 nm light. The reason for this lies in the band structure (see Fig. 5.1). For a very flat potential, the energy gap between the first and higher bands is very small. Ramping up the lattice in a timescale faster than the recoil time would therefore excite the atoms into a higher band. On the other hand the ramps also have to be slow for a deep lattice to stay in the adiabatic regime. Here the atoms are confined to lattice wells and can not move freely as in the pure XODT case but go from one lattice site to the next by hopping which is described by the rate $t/\hbar$ (with t being the hopping amplitude, see equs. 5.7, 5.10). The deeper the lattice, the smaller the hopping rate. To avoid excitations of the BEC, now a change of the envelope trap frequencies has to be slow enough that the atoms can follow by hopping. This sets an upper limit for the lattice ramp up speed which may lead to an increase of decoherences due to a longer ramp time.

To analyze the lattice ramp problem it is helpful to calculate the detailed change of the envelope frequencies when ramping up the lattice equally in ODT1- and ODT2-direction. Fig 4.7 shows the result of such a calculation on the basis of eq. 4.14. The envelope trap frequencies are evaluated following the description in 4.2.

The plot shows two main points. First the the envelope frequencies change significantly when ramping up the lattice and second this change leads to a shift of the BEC position in z-direction (gravitational sag). The reason for this connection becomes clear when one remembers that the dipole force in a red-detuned trap pulls the atoms to the places of high intensity that are the centers of the Gaussian beams. If the intensity of the beams is increased due to reflecting back parts of the light (cf. eq. 4.14) the dipole force becomes stronger with respect to the gravitational force which leads to a "pull-up" effect for the BEC. At the new position the envelope frequencies differ from the old ones since the trap minimum now is closer to the beam centers. As a result the trap frequencies are directly connected to the gravitational sag. To avoid the change of the envelope frequencies, the power of the incoming beams

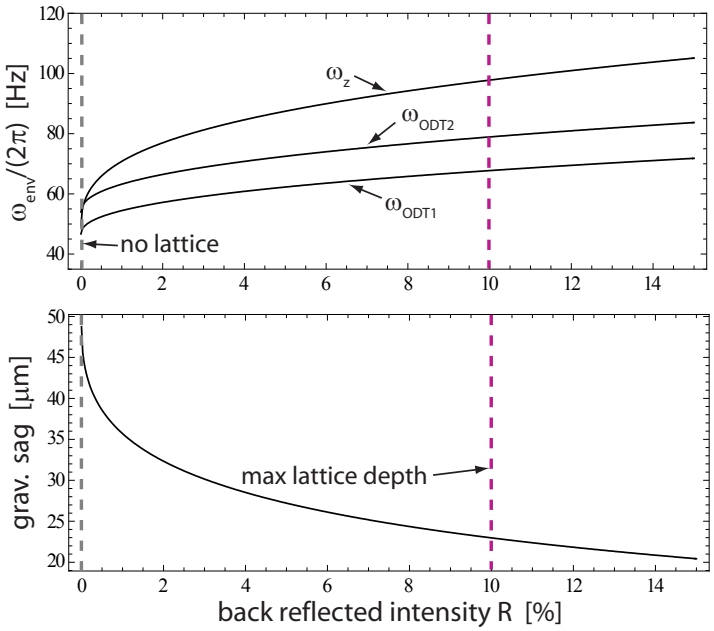

Figure 4.7: Change of ω_{env} due to ramping up the OL in the xy-plane of the lab coordinate system. The parameters of the beams are the same as for Fig. 4.3. It is assumed that the smallest waists of the reflected beams have the same sizes and positions as for the incoming beams. The parameter R on the abscissa equals both, R_{x} and R_{y}. The lower graph shows the change of the gravitational sag (compare Fig. 4.3) as a function of R.

can be decreased proportionally when $R_{x,y}$ is increased.
Experimentally this can be done by looking at the change of the position of the BEC in z-direction. Fig. 4.8 shows data from such an experiment. In detail the BEC was loaded into the XODT and the lattice in OL1-direction was ramped up exponentially while the power in the ODT2 beam was held constant. At a certain point of the lattice ramp an in situ image of the BEC was taken. The z-position of the BEC of this image is now compared with a reference image of the BEC held in the full power XODT with no lattice beams (point without error bars in Fig. 4.8). If the lattice in OL1-direction is ramped up with ODT1 and ODT2 beams at full power a clear shift (up to ~ 15 μm for max. lattice depth) in z-direction (with respect to the z-position of the reference file) against gravity can be seen. The data points in Fig. 4.8 are obtained by looking at this shift for a certain back reflected intensity along Ol1-direction (which corresponds to a certain lattice depth along this direction) and resetting it (the shift) with respect to the reference by taking power out of the ODT1 beam. The black line in the figure is a best fit with the model developed for Fig. 4.7. The theory contains the powers, the waists and the percentage of back reflected light (to form the lattice) of the beams as variables. For the data in Fig. 4.8 the values of the ODT2 beam do not matter since the BEC is always sitting at the same position in this beam and the ODT2 parameters do not change. Due to the normalization in Fig. 4.8 the power and the waist of ODT1 can be changed without affecting the fit. Therefore the maximum value for R_x (see eq. 4.14) is the only free parameter. It is evaluated to $R_x^{(max)} = (1.22 \pm 0.20)$ %. This value corresponds to the max. lattice depth in Fig. 4.7. In this figure however $R_x^{(max)}$ is shown to be 10 %. One has to remember now that Fig. 4.7 is based on a calculation where the incoming and reflected beams have the same waist properties at the BEC-position. Since a beam pick-off was used to measure $R_{x,y}^{(max)}$ between the science cell and the AOM-shutters (compare Fig. 4.5) and 10 % were found it is very likely that the waists of the back reflected beams are bigger than the ones of the incoming beams. eq. 4.9 and eq. 4.2 tell that the dipole potential the atoms see is proportional to $1/w^2$. This means that the waist of the back reflected beam at BEC position should be $\sim$3 times bigger than the ODT1 waist.
For the ODT2 direction the same data as shown in Fig. 4.8 has been taken. It comes out that $R_y^{(max)} = (2.10 \pm 0.20)$ %. Therfore an equal argumentation holds for the waists of the OL2 beams as for the OL1 ones.
With the data of Fig. 4.8 and the corresponding data set for the ODT2 direction the lattice in ODT1- and ODT2-direction can now be ramped without changing the position of the BEC and without changing the envelope trap

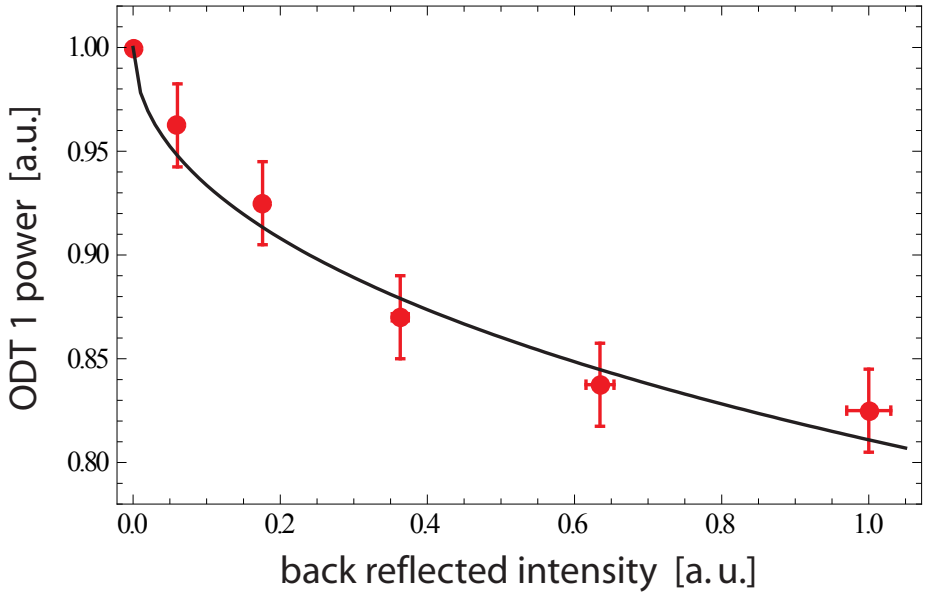

Figure 4.8: Canceling the shift of the BEC position (found by simple Gauss fit) against gravity when ramping up the lattice. The ODT2 beam stays at constant power whereas the ODT1 power (vertical axis) is reduced when the lattice in OL1 direction (horizontal axis) is ramped up. For each data point the power in the ODT1 beam is chosen such that the z-position of the BEC is always the same. The black line is numerically found with the theory for Fig. 4.7 by requiring no change in the gravitational sag (cf. Fig. 4.3). The only free parameter in the fit (again assumption: waist of incoming and reflected beam have same size and sit at BEC position) is the maximum reflectivity R_{x} (see eq. 4.14) which corresponds to the very right data point in the plot. The fit suggests $R_{\mathrm{x}}^{(\mathrm{max})} = (1.22 \pm 0.20)$ %.
The errors of the data arise from the calibration of the AOM shutter ($\pm 3\%$ horizontal) which regulates the lattice depth (see Fig. 4.5), and from the variation of the z-position for 3 different runs (vertical error) for fixed hoizontal and vertical values in the plot.

frequencies (compare to Fig. 4.7). This has the two advantages that first the atoms do not have to redistribute due to a change of the external confinement and second the BEC is not pulled through the lattice which can be applied along the z-direction. Both advantages reduce heating of the atoms when loading them into the lattice.

4.3.2 Lattice Sites

The second important part of the lattice (besides the envelope) of course is formed by the lattice sites themselves. For an expansion of the BEC over $\sim$ 50 lattice sites per direction the envelope only changes slightly from the center to the last occupied site. Therefore it is a good approximation to describe the lattice sites by the parameters of a site at the trap center. For our setup the light field at the trap center can be approximated as plane waves with a Gaussian envelope. A simple calculation on the basis of the dipole force of a plane wave with a Gaussian envelope gives the site frequencies and the lattice depth as a function of the back reflected power. Fig. 4.9 shows the justification (part a)) for a description of all 50 occupied sites along one direction by the center lattice site. From the plots it can be seen that high lattice depth can be achieved assuming that the smallest waist of the back reflected beams have the same size and position as for the incoming beams. Part d) shows the effect of lowering the incoming power on the site frequencies. This is of interest if one wants to maintain the envelope frequencies (see above). The depth of the lattice sites decreases proportionally with the incoming power because the incoming intensity is just a factor in the formula describing the lattice depth (compare to eq. 4.14).

4.4 Kapitza-Dirac Diffraction

To be able to make quantitative statements it is important to know the lattice depth of the applied OL. Since the lattices along different directions are decoupled in our case it is sufficient to concentrate on the 1D case. In 1933, Kapitza and Dirac proposed that electrons should be diffracted by a standing light wave [65]. This effect also happens for atoms [58] instead of electrons and is even stronger pronounced for equal light intensities.
For the purpose of lattice calibration the BEC is held in the XODT and a lattice along a certain direction is pulsed on (=Kapitza-Dirac pulse =KD pulse). The system can now be described by the Hamiltonian:

$$\widehat{\mathcal{H}} = -\frac{\hbar^2}{2m}\frac{\partial^2}{\partial x^2} + V_0 \cos^2[kx] \tag{4.15}$$

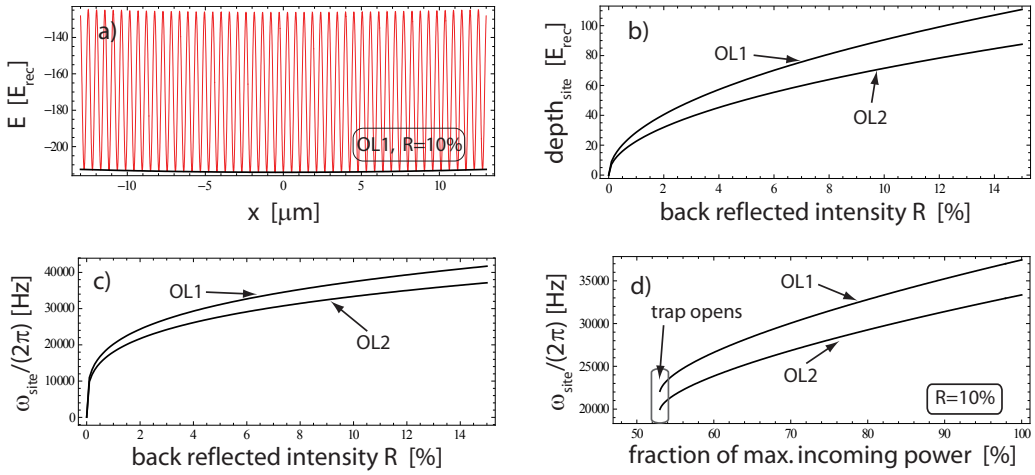

Figure 4.9: Overview of lattice parameters. Part a) shows the red lattice sites (around 50 here) for R=10% along the OL1 direction. The black line at the bottom of the plot is the envelope function which occurs due to the transverse Gaussian distribution of the OL2 beams. All the plots are based on the same beam parameters as in Fig. 4.7 and Fig. 4.3 as long as nothing else is mentioned especially. Part b) shows the depth and part c) the site frequencies along the OL1- and OL2-axis. Part d) shows the change of the site frequencies for a back reflected intensity of 10% when one lowers the power of both incoming beams equally. The end of the plot between 50 and 60% indicates that the power of the beams becomes to low to hold the atoms against gravity.

where m is the mass of the ^{87}Rb atoms, V_0 the lattice depth and k the wave vector of thef laser light that forms the lattice. Inserting the Ansatz

$$\Psi = \sum_n c_n[t] \exp[i2nkx] \tag{4.16}$$

with n being an integer, $c_n[t=0] = \delta_{0,n}$ and $\sum_n |c_n[t]|^2 = 1$ into the time-dependent Schödinger equation with the Hamiltonian from eq. 4.15 leads to

$$i\dot{c}_n[t] = \frac{2\hbar n^2 k^2}{m} c_n[t] + \frac{V_0}{4\hbar}(c_{n-1}[t] + 2c_n[t] + c_{n+1}[t]) \tag{4.17}$$

The coefficients c_n tell how much the n^{th} diffraction order is populated by the condensate wave function. The term $\frac{2\hbar n^2 k^2}{m}$ (kinetic energy) becomes more important for longer interaction times (pulse lengths). Note that a change of n by 1 corresponds to a change of 2 in terms of scattered photons.
For $\tau \ll 1/\omega_{osc} \sim \frac{1}{k}\sqrt{\frac{m}{V_0}}$ the first term on the right hand side (kinetic energy) of eq. 4.15 can be neglected and the coupled differential equations 4.17 have the analytic solutions $c_n[t] = i^n \exp[-i\frac{V_0}{2\hbar}t] J_n[-\frac{V_0}{2\hbar}t]$ with J_n being the Bessel functions of the first kind. This approximation is called the Raman-Nath approximation and can be made when the length τ of the applied lattice pulse is much smaller than the oscillation time of a particle in a lattice well. Now the population in the nth diffraction order due to atom photon scattering from the KD pulse is given by the absolute value of $c_n[t]$ squared

$$P_n = J_n^2 \left[\frac{V_0}{2\hbar}\tau\right] \tag{4.18}$$

For sufficiently short pulses (note: short is here always dependent on the lattice depth V_0) equation 4.18 can be used to calibrate the lattice depth.
Fig. 4.10 shows a typical KD pattern. Wanting to know the the lattice depth one could use eq. 4.18 as a fit function. However especially for deep lattices[5] the above condition, for eq. 4.18 to be valid, is easily broken (unless pulse durations are very short which gives a technical limit) and the suggested fit introduces a uncertainty. To overcome this drawback but not wanting to loose an analytical fit function, different simple extensions to the model are possible [66]:
The maximum occupied diffraction order $n_{\max}$ is given by $n_{\max}^2 = \frac{V_0}{4\mathrm{E_{rec}}}$ where the lattice energy is fully converted into kinetic energy [67]. For not to high

[5]The lattice for Fig. 4.10 turns out to be $\sim 20\, E_{\text{rec}}$ deep. A fit with eq. 4.18 however requires $V_0 \ll 10$ $\mathrm{E_{rec}}$ for a 10μs pulse. And even for shallow lattices corrections have to be added here [66].

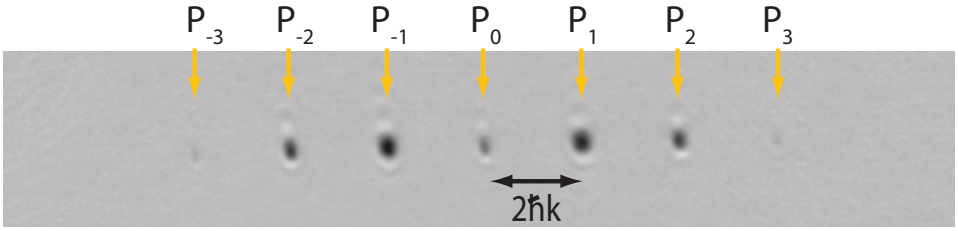

Figure 4.10: Typical diffraction pattern after 12 ms of free expansion from XODT. The length of the KD square pulse equals 10 μs. The pulse is generated with the 785 nm lattice along the z-direction (cf. Fig. 4.5 and Fig. 4.13) and controlled with an AOM. The peaks are separated by $2\hbar k$ which can be understood with eq. 4.16 and 4.18. For an analysis in terms of lattice calibration one has to evaluate the relative atom number in each diffracted peak by summing over the optical density (see 2.2).

lattice depth ($V_0 \lesssim 4\mathrm{E_{rec}}$) only the 0th and the 1st diffraction patterns are populated. This means eq. 4.18 can be truncated for $|n| > 1$. The remaining three coupled equations can be solved analytically and give

$$P_{\pm 1} = \frac{1}{2}\left(\frac{\chi}{\Omega}\right)^2 \sin^2\left[\frac{\Omega}{2}\tau\right] \quad \underline{\textbf{and}} \quad P_0 = 1 - 2P_{\pm 1} \tag{4.19}$$

with a generalized Rabi frequency $\Omega = \sqrt{\chi^2 + \Delta^2}$, a resonant coupling term $\chi = V_0/(\sqrt{2}\hbar)$ and a detuning of $\Delta = 4\mathrm{E_{rec}}/\hbar$. The analogy in terms of structure to a Rabi frequency that drives a two level atom can be drawn because of the symmetry of the problem which generally has its manifestation in $P_n = P_{-n}$.
Thinking in terms of the Rabi formalism (see 2.3.1) helps to motivate an advancement to eq. 4.18. A scattering event that puts an atom from the $|0\hbar k\rangle$ to the $|\pm 2\hbar k\rangle$ state needs to conserve energy. Energy conservation can be fulfilled by a detuning of Δ of the scattered photon with respect to its standing light wave. Now it is well known that there is a connection between the temporal width and the frequency width of a light pulse. The connection is formed by a Fourier transformation where the two widths behave reciprocally with respect to each other: the longer the pulse in the time domain the narrower is its frequency width and vice versa. In our case this translates to a bigger Δ and therefore an occupation of higher momentum states for a smaller pulse width. The used pulses are rectangular in the time domain. The Fourier transform of such a rectangular function is a sinc function and well known from diffraction at a slit. Here this motivates to extend the Bessel function in eq. 4.18 to

$$P_n = J_n^2 \left[\beta \,\mathrm{sinc}\frac{\alpha}{2}\right] \tag{4.20}$$

The two dimensionless parameters $\alpha = (4\mathrm{E_{rec}}/\hbar)\tau$ and $(V_0/2\hbar)\tau$ are introduced for convenience. Indeed the two formulas eq. 4.20 and eq. 4.19 agree well up to $\mathcal{O}(\alpha^2\beta^2)$. These two analytical formulas fit much better with experimental observations than the simple Bessel function from eq. 4.18 [66].
The possibility of using these functions however ends with stronger lattice pulses when the kinetic energy term in eq. 4.17 cannot be neglected or higher momentum orders are populated by the atomic wave function. In this case eq. 4.17 can be truncated for $n \gg n_{\mathrm{max}}^{(\mathrm{observed})}$ and numerically integrated. This method is reliable without any restrictions (except of the disregard of a mean-field interaction in eq. 4.15) and is always used within the frame of this thesis when lattice depths are named.

4.5 State-Dependent Optical Lattice

So far optical lattices in general have been discussed. This discussion entirely ignored the atomic hyperfine the ^{87}Rb atoms (although it was included in the calculations). This has been valid since the used lattice wavelength of 1064 nm is so far detuned from the atomic transitions that the finer structure is not resolved. Even the very rough formula 4.8 gives a very good approximation of the potential the atoms see independently of their internal state. This means that this OL is state independent and traps all atomic states equally. For a lattice wavelength close to the atomic transitions of ^{87}Rb (D1- and D2-line) the situation becomes much richer [25, 26]. Fig. 4.11 shows the hyperfine structure of ^{87}Rb. The two ground states $|\mathrm{F} = 1, \mathrm{m_F} = -1\rangle$ and $|\mathrm{F} = 2, \mathrm{m_F} = -2\rangle$ are marked in the scheme. These two levels are chosen to be the quantum states of interest for the 2 component Bose-Hubbard model which will be discussed later.

4.5.1 State-Dependent Potential

In order to calculate the potential that acts on the atoms eq. 4.5 has to be consulted. The dipole potential that is described in this equation is a function of the dipole matrix element given with eq. 4.4. To derive an equation for the potential an atom in one particular hyperfine state feels, the sum $\sum_{\mathrm{t}} U_{\mathrm{dipole,t}}$ is evaluated. As described above, this means summing over all levels that can couple to the fixed hyperfine state of interest. Doing so the only problem that has to be solved lies in the calculation of the dipole matrix elements in eq. 4.4.

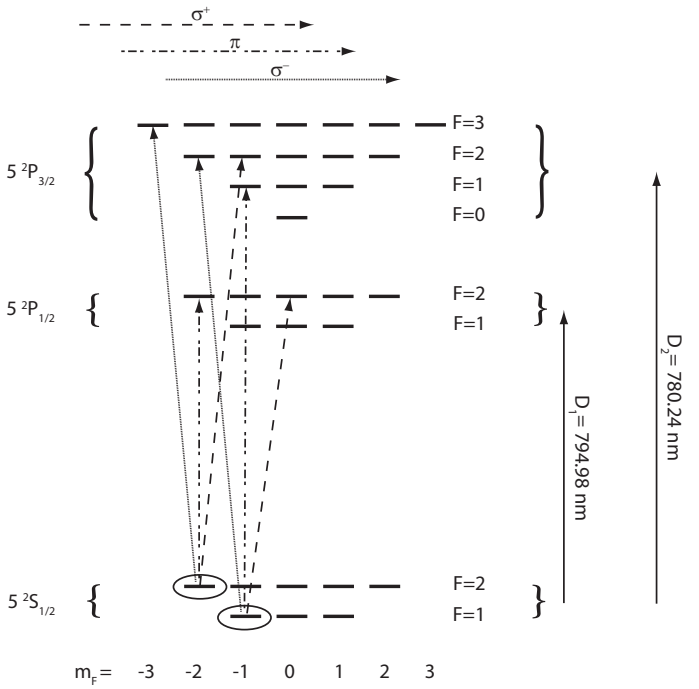

Figure 4.11: The hyperfine structure of ^{87}Rb with its magnetic sublevels (not on scale). The states $|\mathrm{F}=1,\mathrm{m_F}=-1\rangle$ and $|\mathrm{F}=2,\mathrm{m_F}=-2\rangle$ are marked since the atoms are only prepared to be in these states in the experiment. Some possible dipole transitions regarding these states of interest are indicated. The D1- and the D2-line are shown to give a scale of the transitions in terms of wavelength.

It turns out that these matrix elements can be reduced to a constant for each line (D1, D2) which is multiplied by Clebsch-Gordan coefficients that depend on the polarization of the light that forms the dipole potential (see [45]). As an example the state $|\mathrm{F}=2,\mathrm{m_F}=-2\rangle$ could be considered. For this state most of the dipole matrix elements are 0 which can be seen by calculating them or just by looking at Fig. 4.11. It is clear that none of the S-states can give a contribution since the dipole selection rule forbids transitions with $\Delta l = 0$. Due to conservation of angular momentum all matrix elements with $m_F \geq 0$ are 0 because none of the existing polarizations of light can induce single photon transitions with $|\Delta m| > 1$. The remaining possible transitions that contribute to the potential with the corresponding dipole matrix element now depend on the chosen polarization of the light. Fig. 4.11 shows some possible transitions. In order to follow the chosen example, one could choose σ^+-polarized light. This means that all the matrix elements that connect to the P-states with $m_F = -1$ can give non-zero numbers. Therefore 5 matrix elements have to be calculated to be put in $\sum_{\mathrm{t}} U_{\mathrm{dipole,t}}$ where the ground state is $|\mathrm{F}=2,\mathrm{m_F}=-2\rangle$ and the light is σ^+-polarized. This can be done for other polarizations and for the $|\mathrm{F}=1,\mathrm{m_F}=-1\rangle$ state.

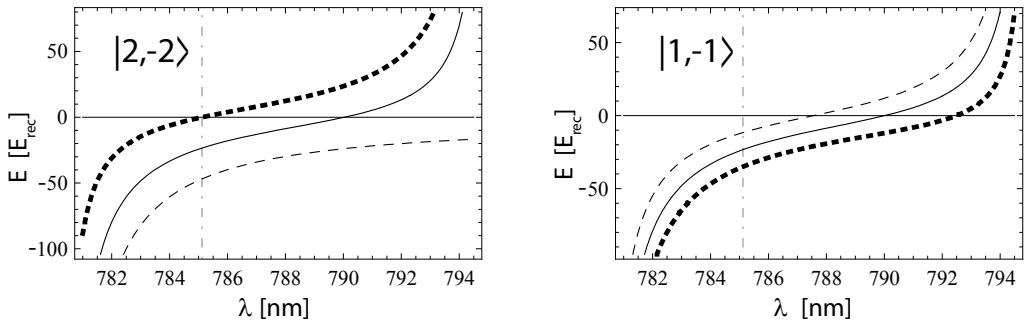

Figure 4.12: State-dependent potentials for the states $|\mathrm{F}=2,\mathrm{m_F}=-2\rangle$ and $|\mathrm{F}=1,\mathrm{m_F}=-1\rangle$. The solid lines correspond to π, the thick dotted lines to σ^+ and the dashed lines to σ^- polarized light. The vertical dashed dotted lines indicate the zero of potential for the $|\mathrm{F}=2,\mathrm{m_F}=-2\rangle$ state and σ^+ polarized light which happens at λ= 785.12 nm. The potential is calculated for ^{87}Rb atoms sitting at the smallest waist of a 230 μm laser beam (no standing wave) with 125 mW power.

Fig. 4.12 shows the result of the calculation. In order to define a quantization axis for the polarization a small magnetic field which points along the propagation direction of the light has to be applied. The small effect of this field (Zeeman shift) can be neglected in the calculations. The direction of the

magnetic field however is crucial since an angle between the laser beam and the magnetic field lines breaks the rotational symmetry of the potential and leads to coherences between the magnetic sublevels. This can lead to off diagonal terms in the Hamiltonian of the problem and changes the structure of the potential[6]. Here this is not done but the magnetic field is aligned parallel to the laser beam and has a magnitude of ~ 300 mG.
We now want to concentrate on σ^+-light (thick dotted line in Fig. 4.12). As indicated by the dashed dotted line the potential for the $|\mathrm{F} = 2, \mathrm{m_F} = -2\rangle$ state vanishes (of course independently of the intensity since the intensity is just a factor in eq. 4.5) for a laser wavelength of about 785 nm. The $|\mathrm{F} = 1, \mathrm{m_F} = -1\rangle$ state however feels an attractive force at this wavelength. The possibility of a laser wavelength with vanishing dipole potential could have been guessed with the simplified formula eq. 4.8. For red-detuning with respect to a transition this potential is attractive for blue-detuning however repulsive. Furthermore the strength of the potential becomes bigger the smaller the detuning is chosen. Having now two transitions (here D1 and D2-line) it seems to be natural that there is a wavelength in between the lines where the attractive (D2-transition) and the repulsive (D1-transition) forces cancel out. This is the main idea for a state-dependent optical lattice (SDOL), where the beam of a wavelength and polarization at which one species sees a lattice but the other one does not, is reflected back to itself and forms a 1D OL for one species but not for the other one.
In the experiment the SDOL beam is set up along the z-direction in the lab coordinate system as shown in Fig. 4.13.

To test the described idea of a SDOL experimentally the BEC is loaded into the XODT. Then a 10 μs long 785 nm lattice pulse with constant depth is applied along the z-direction, the atom cloud is dropped by switching of the XODT and an absorptive Image is taken after a TOF of 12 ms. Fig. 4.10 shows an image that led to a data point for the measurement. The lattice depth is then found with the procedure described in 4.4. To introduce the effect of the state-dependence the measurement is once done with the atoms in the $|\mathrm{F} = 1, \mathrm{m_F} = -1\rangle$ and once with the atoms in the $|\mathrm{F} = 2, \mathrm{m_F} = -2\rangle$ state. In the second case the nearly full population transfer from $|\mathrm{F} = 1, \mathrm{m_F} = -1\rangle$ to $|\mathrm{F} = 2, \mathrm{m_F} = -2\rangle$ is driven by a Landau-Zener sweep (see 2.3.1) with the atoms sitting in the XODT. For both of the named atomic states the angle of a $\lambda/4$-plate that changes the polarization of the applied 785 lattice is scanned through.
Fig. 4.14 shows the obtained KD patterns for the $|\mathrm{F} = 2, \mathrm{m_F} = -2\rangle$ state. One

[6]Therefore it is possible to create double well potentials by choosing the right angle between the magnetic field and the direction the beam propates along (cf. [25]).

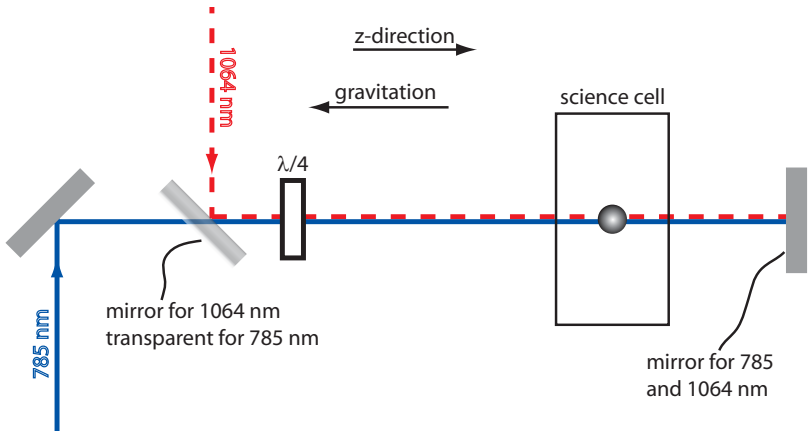

Figure 4.13: Simplified setup of z-lattice. Along the z-direction the state independent 1064 nm beam can be exchanged by a state-dependent 785 nm beam. If we are talking about a SDOL it means that there is no 1064 but only the 785 beam along the z-direction. Along the x′ and y′-direction (compare to Fig. 4.5) no SDOL exists. For switching between the 1064 and the 785 lattice the setup does not have to be changed. The trick is to use a dichroic mirror for 1064 light that is (nearly) transparent for 785 light. For the SDOL a 300 mG magnetic field is applied along the z-direction.

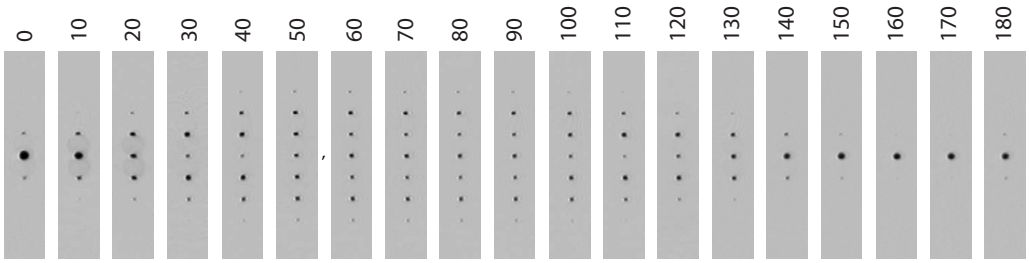

Figure 4.14: The picture shows KD-patterns for a 10 μs 785nm lattice pulse of constant intensity applied to atoms in the $|\mathrm{F} = 2, \mathrm{m_F} = -2\rangle$ state. The numbers above the images give the the angle (in degree) of the $\lambda/4$-plate (see Fig. 4.13) that changes the polarization of the lattice beam

sees that the effect of the KD pulse becomes minimal at an angle of $\sim 160°$. Evaluating the lattice depth for both states as a function of the angle of the $\lambda/4$-plate leads to Fig. 4.15.

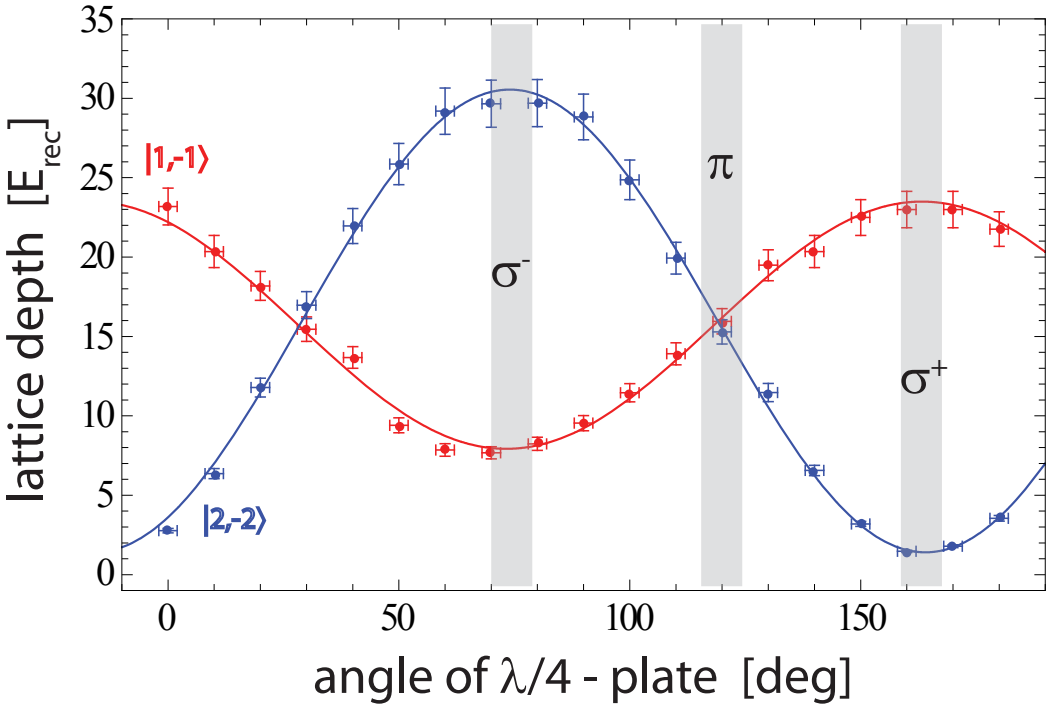

Figure 4.15: Polarization dependent lattice depth for the $|\mathrm{F}=1,\mathrm{m_F}=-1\rangle$ and the $|\mathrm{F}=2,\mathrm{m_F}=-2\rangle$ state. The lattice depth is plotted as a function of the polarization of the 785 nm light that forms the OL. The locations of typical polarizations are indicated by transparent gray vertical bars. The error of the wave plate angle is estimated with $\pm 2°$. The error of the lattice depth rises because of a $\pm 5\%$ variation of the monitored back reflected light intensity[3]. An error of the lattice depth fit which tends to overestimate the lattice depth for shallow lattices is not included. The blue and the red curve are best fits (see text).

The data of Fig. 4.15 is fit with the fit function $A \sin\left[\frac{\pi}{90}x + \phi\right] + off$. Table 4.2 shows the values of the fit parameters.
Comparing the theoretical result form Fig. 4.12 with the obtained experimental result from Fig. 4.15 good agreement can be seen. First Table 4.2 gives the phases ϕ of the sinusoidal fit function which are off by exactly π with respect

[3]The back reflected 785 beam that forms the lattice with in this case constant ingoing beam, can be monitored with a photo diode that measures a small part of the back reflected intensity which is deflected by a beam pickoff.

	A [E_{rec}]	off [E_{rec}]	ϕ
$\|F = 1, m_F = -1\rangle$	7.78 ± 0.20	15.71 ± 0.14	2.156 ± 0.026
$\|F = 2, m_F = -2\rangle$	14.57 ± 0.17	15.98 ± 0.12	-1.013 ± 0.012

Table 4.2: Best fit parameters to data shown in Fig. 4.15 with $A \sin\left[\frac{\pi}{90}x + \phi\right] + off$ as fit function. The errors are the standard errors from the fit.

to each other. This is in nice agreement with the theory since the σ^+ and the σ^--potential lines in Fig. 4.12 are flipped for the $|F = 1, m_F = -1\rangle$ and the $|F = 2, m_F = -2\rangle$ state. The offset parameter off is about the same for both states. This parameter tells the height of the point symmetry center of the two data sets. This center lies right in between σ^+ and σ^- polarized light and is realized by the data when the $\lambda/4$-wave plate does not affect the linear polarization of the light. Therefore the light remains π-polarized and the parameter off gives the corresponding lattice depth. Comparing the result that both states should see nearly the same lattice for 785 nm π polarized light with the theory leads again to a nice agreement. In the end the relative depth of the potentials can be compared with theory. This can be done by calculating the ratio of the measured curves for σ^--light and comparing this with the theoretical values for 785 nm light of the same polarization. This leads to

$$\frac{E^{785\,\mathrm{nm},\,\sigma^-}_{\mathrm{measured}}[|F{=}1,m_F{=}-1\rangle]}{E^{785\,\mathrm{nm},\,\sigma^-}_{\mathrm{measured}}[|F{=}2,m_F{=}-2\rangle]} = \frac{off[|F{=}1,m_F{=}-1\rangle]-A[|F{=}1,m_F{=}-1\rangle]}{off[|F{=}2,m_F{=}-2\rangle]+A[|F{=}2,m_F{=}-2\rangle]} = \underline{0.260 \pm 0.08}$$

$$\frac{E^{785\,\mathrm{nm},\,\sigma^-}_{\mathrm{theory}}[|F{=}1,m_F{=}-1\rangle]}{E^{785\,\mathrm{nm},\,\sigma^-}_{\mathrm{theory}}[|F{=}2,m_F{=}-2\rangle]} = \underline{0.257}$$

Again theory and experiment agree within the margin of error that is given by simple error propagation. For π-light experiment and theory are in good agreement, too.
However looking at σ^+-light one would expect no potential for the $|F = 2, m_F = -2\rangle$ state, but there clearly is a residual lattice in Fig 4.15 for this state. One explanation for this is that the numerical lattice depth fit based on eq. 4.17 tends to overestimate the lattice depth for very weak lattices. On the other hand one can still see very dilute diffraction peaks in Fig. 4.14 for an angle of 160° (that is the lowest fitted lattice depth for the $|2, -2\rangle$ atoms). This can either be explained by weak residual magnetic fields which do not point along the 785 lattice beam direction or by the fact that the laser wavelength does not exactly correspond to the calculated magic wavelength of 785.12 nm.

Both effects lead to a non-vanishing potential for the mentioned atomic state. To draw a conclusion the experimental results are in good agreement with the theoretical calculation.

4.5.2 State-Dependent Scattering Rate

The availability of a state-dependent optical potential has the great advantage to give one the possibility to explore new and rich physics in the ultra cold regime. However a potential with a wavelength between the D1- and D2-line of the atom under study results in a much higher scattering rate than for the 1064 nm potential of the XODT.
Fig. 4.16 shows the measurement of the scattering rate for 780.8 nm light with respect to ^{87}Rb atoms in the $|\mathrm{F} = 1, \mathrm{m_F} = -1\rangle$ state. This measurement is repeated for 785.3 and 779.0 nm. Table 4.3 gives the measured scattering rates for these wavelengths.

λ [nm]	779.0 ± 0.3	780.8 ± 0.3	785.3 ± 0.3
Γ_{scatt} [1/s]	0.62 ± 0.14	6.1 ± 1.3	0.221 ± 0.051
P [mW]	11.75 ± 0.59	1.48 ± 0.07	22.1 ± 1.1

Table 4.3: Values of measured scattering rate (σ^+-light) for a beam power of 10 mW (scaled!) and waist of 230 μm (experimental waist) at the BEC position. The errors result from a error analysis of the errors of the measured power (5%) and waist of the beam (10%) and of the fit error (compare Fig 4.16). The wavelength error is estimated (calibration issue with wave meter). The last line gives the experimental power of the beam at BEC position.

In order to compare the experimental results with theory eq. 4.4 and 4.7 have to be consulted. The scattering rate is then evaluated in exactly the same way as described in the previous part of this chapter. Fig 4.17 shows the calculated scattering rates for different polarizations of the light. Part c) gives the comparison between the measured data and the theoretical curve with no free parameters.
All points except the measured point at around 785 nm agree well with the theory. The measured scattering rate at $\sim$ 785 nm however is slightly higher than the theory value. One systematic error in the measurement could be that a scattered photon removes more than one atom from the BEC by a avalanche like effect that comes in by atom-atom interaction. Furthermore the theory does not implement saturation effects. This, however, is insignificant in our case because the used intensity stays far below the saturation intensity. In conclusion the theory fits well with the experimental data and the scattering

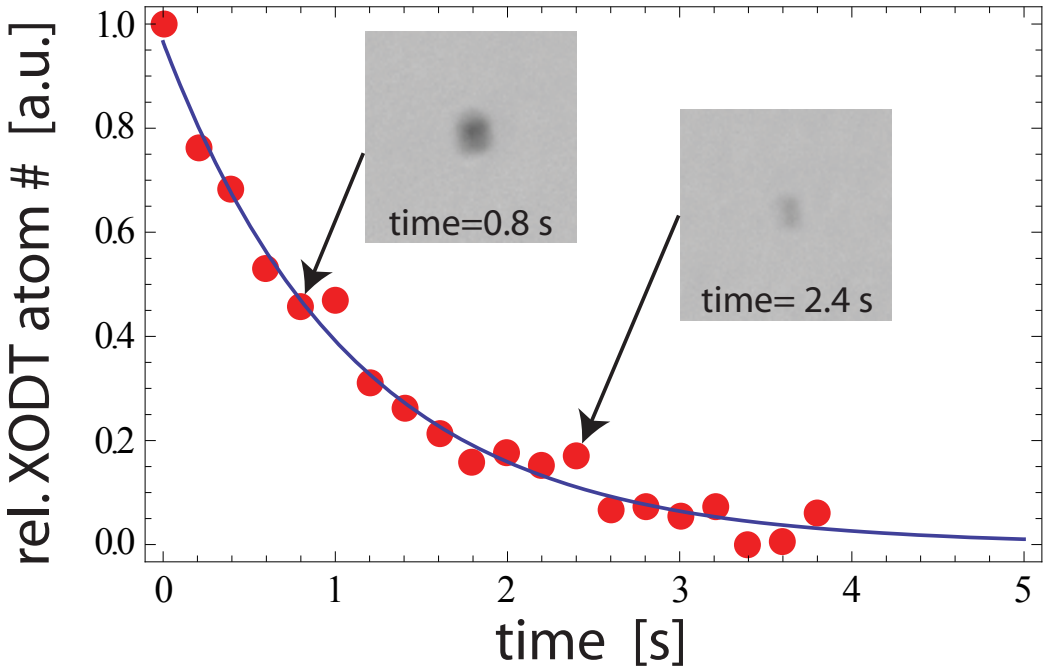

Figure 4.16: State-dependent scattering rate measured for $|\mathrm{F}=1,\mathrm{m_F}=-1\rangle$ atoms and σ^+-light at λ= (780.8±0.3) nm with a power of the 780.8 nm beam in the science cell of (1.48±0.08) mW. The beam has a smallest waist at the BEC position of (230±23) μm. The time on the abscissa of the plot gives the exposure time of the BEC to the 780.8 nm light. The BEC is trapped in the 1064 nm XODT. The y-axis shows the remaining atom # after a certain exposure time to the 780.8 nm light divided by a reference atom # that was measured without the 780.8 nm light. The holdtime of the reference run in the XODT equals the holdtime for the corresponding 780.8 nm run that was taken directly before the reference run to exclude the effect of long time drifts in the atom #. The plot shows the best fit of the data with the fit function $A \cdot \exp[-\Gamma_{\mathrm{scatt}} t]$ with A and Γ_{scatt} as free parameters. The two insets show example images of the BEC after a certain exposure time to the 780.8 nm light.

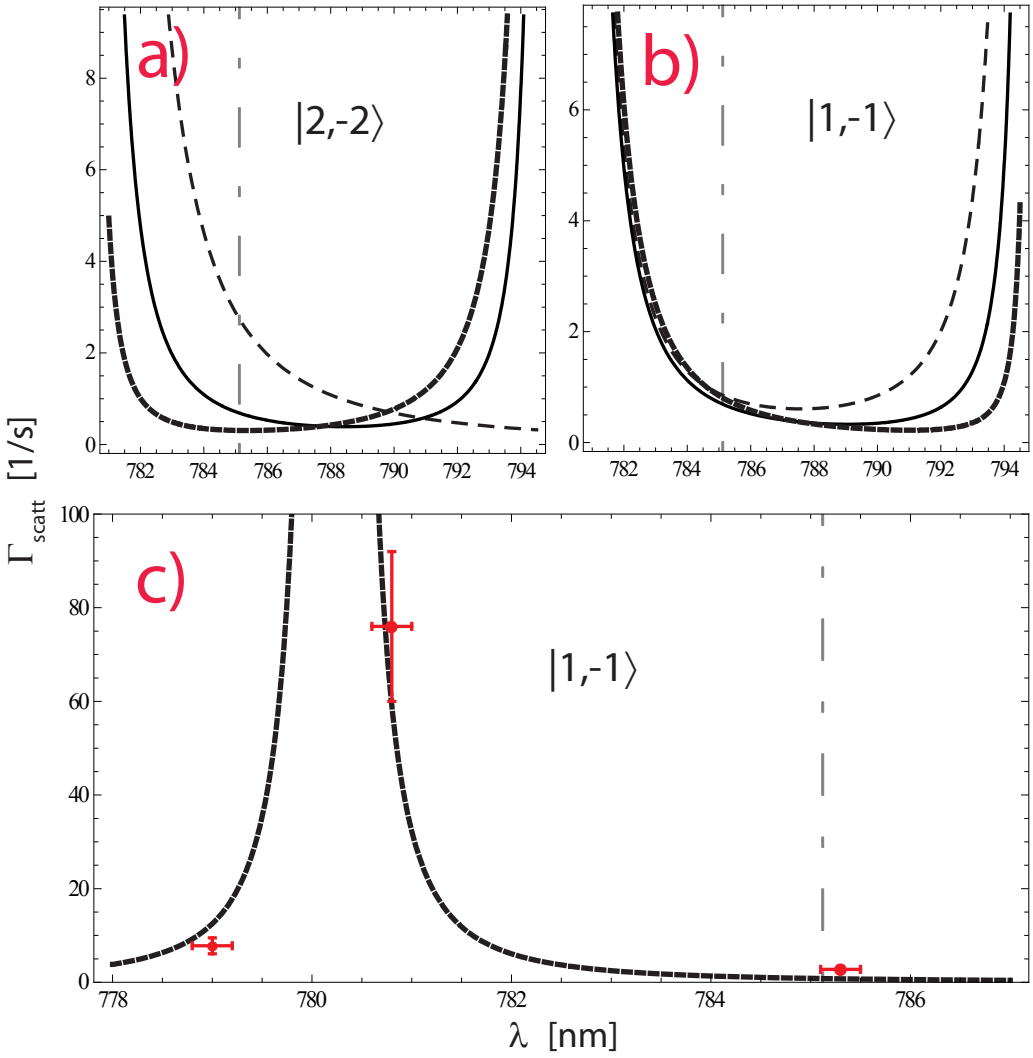

Figure 4.17: State-dependent scattering rate. a) and b) show the scattering rate for the two ^{87}Rb states of interest. Again the solid lines correspond to π, the thick dotted lines to σ^+ and the dashed lines to σ^- polarized light. Part c) shows the data from table 4.3 with the corresponding theoretical curve. The dashed dotted line is again drawn at the "zero-lattice" wavelength (see Fig. 4.12). All plots are shown for atoms which sit at the intensity maximum of a Gaussian beam with a waist of 230 μm and a power of 125 mW.

rate at $\sim$ 785 nm is low enough to give a sufficiently long time scale for performing experiments with a SDOL without leaving the quantum gas regime.

Chapter 5

Optical Lattice Bandstructure and Bose-Hubbard model

Here we want to give the theoretical and experimental basis for a state-dependent two-component lattice experiment. Therefore we first discuss theoretical models of bosons in a lattice and then check the functionality of our system with a one-component SF-MI transition. The two-component case will be treated theoretically at the end of this chapter.

5.1 Solid State Description

The system of atoms in an OL shows strong parallels to the typical solid state system of electrons moving in the potential of atomic ions. Both systems exhibit the periodic structure of the potentials and in both the particles which move in the potentials can (in a first step) be considered without mutual interactions. Therefore the atom-OL system can be treated with well known formalisms from solid state physics in a time independent way. For a lattice potential of infinite extent the eigenenergies of the system lie in continuous bands which are separated by gaps. The wave function of a particle in such a 1D lattice can be written as a plane wave multiplied by a function with the lattice periodicity (Bloch theorem) [68, 69]:

$$\Phi_q^{(n)}[x] = \exp\left[i\frac{qx}{\hbar}\right] u_q^{(n)}[x] \tag{5.1}$$

where q is called the quasimomentum, is continuous and can be reduced to the 1st Brillouin zone due to the periodicity of the problem whereas n is a positive integer and labels the energy bands. Inserting this Ansatz into the standard time-independent Schrödinger equation of a particle in a periodic potential

$V[x]$ leads to:

$$\widehat{\mathcal{H}} u_q^{(n)}[x] = E_q^{(n)} u_q^{(n)}[x] \quad \text{with} \quad \widehat{\mathcal{H}} = \frac{1}{2m}(\widehat{p} + q)^2 + V[x] \tag{5.2}$$

The standing light wave potential (neglecting the envelope) may now be written as

$$V[x] = V_0 \sin^2[kx] = -\frac{V_0}{4}(\exp[2ikx] + \exp[-2ikx] - 2) \tag{5.3}$$

The above form of the potential suggests to write the lattice part of the Bloch function as a Fourier sum:

$$u_q^{(n)}[x] = \sum_s c_s^{(n,q)} \exp[2iskx] \tag{5.4}$$

Inserting this sum into eq. 5.2, writing $\widehat{p}$ as $-i\hbar\partial_x$ and remembering that none of the exponential functions in the sum can be replaced by a linear combination of other exponential functions of the same kind leads to

$$\left(E_{rec}(2s + \frac{q}{\hbar k})^2 + \frac{V_0}{2}\right) c_s^{(n,q)} - \frac{V_0}{4} c_{s+1}^{(n,q)} - \frac{V_0}{4} c_{s-1}^{(n,q)} = E_q^{(n)} c_s^{(n,q)} \tag{5.5}$$

In terms of linear algebra this equation can be written as $\widehat{\mathcal{H}'}\boldsymbol{c} = E_q^{(n)}\boldsymbol{c}$, with $\boldsymbol{c}$ being a vector of infinite extension. The Hamiltonian $\widehat{\mathcal{H}'}$ has one diagonal and two off-diagonal terms per row. The other entries are zero. Of course the Hamiltonian is of infinite extension, too. However it happens that the components of the vector decay rather quickly for big $|s|$. Therefore it is possible to truncate the Hamiltonian and only solve it for $|s| \leq 5$ as long as higher bands are not of interest [61]. Following this path an 11×11 Hamiltonian with real entries remains. The eigenvalues of this Hamiltonian depend on q and n, give the eigenenergies of the system and can be calculated by numerically solving its 11th order polynomial determinant equations. Fig. 5.1 shows the band structure of the described system for different lattice depths. For an increasing depth V_0 the band gap between the 1st and the 2nd band increases whereas the width of the 1st band decreases. The strict theory applies to a lattice of infinite size. It can be shown, however, that for a finite lattice the general results remain valid, but the continuous bands become quasi continuous [69]. The vector components $c_s^{(n,q)}$ can now (with the diagonal matrix equation that follows from the described procedure from eq. 5.5) numerically be obtained for certain n and q. This leads with eq. 5.4 and eq. 5.1 to the Bloch functions $\Phi_q^{(n)}[x]$. It is well known that the Bloch functions spread out over the whole lattice. In our case we are interested in processes in the lattice such as

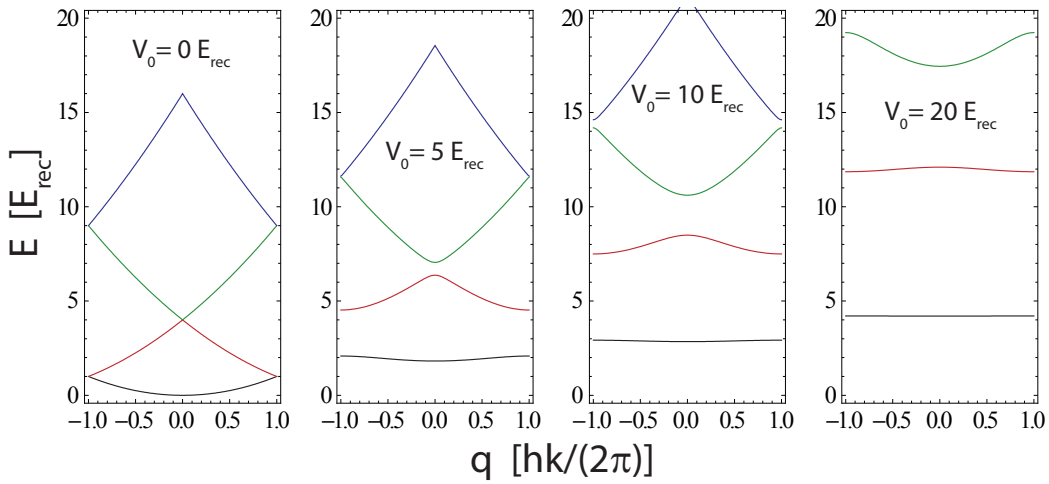

Figure 5.1: 1D band structure of a sinusoidal lattice potential. The plot shows the first energy bands (different bands in different colors). It can be seen clearly that a band gap between the first (black) and the second (red) opens up when a lattice is applied ($V_0 = 5E_{rec}$) and that this gap becomes larger for deeper potentials. Furthermore the width of the first band becomes smaller with higher lattice depths.

tunneling or hopping of particles to neighboring sites. Those processes can be described best with a set of localized wave functions that can be addressed to one specific lattice site. The so-called Wannier functions which are widely used in solid state physics represent such a basis set. Therefore we change our basis from Bloch to Wannier functions. The connection between the two basis sets is given by [69]

$$w_n[x - x_j] = \frac{1}{\sqrt{N}} \sum_q \exp[\frac{iqx_j}{\hbar}] \cdot \Phi_q^{(n)}[x] \tag{5.6}$$

where N is a normalization constant and x_j labels the lattice site at which the Wannier function is localized. For us the Wannier function for different bands and lattice depth can be found with eq. 5.6 by numerically integrating over the known Bloch functions. Fig. 5.2 shows the real Wannier functions of the first band for two lattices of different depth. Furthermore the Gaussian ground wave function of a corresponding harmonic potential is shown. It becomes clear that a particle in the 1st band of a deeper lattice can approximately be treated like a particle in a harmonic potential. This means also that the Wannier function becomes more localized the deeper the lattice is.
A particle in the lattice at the lattice site j in the lowest (=1st) band can

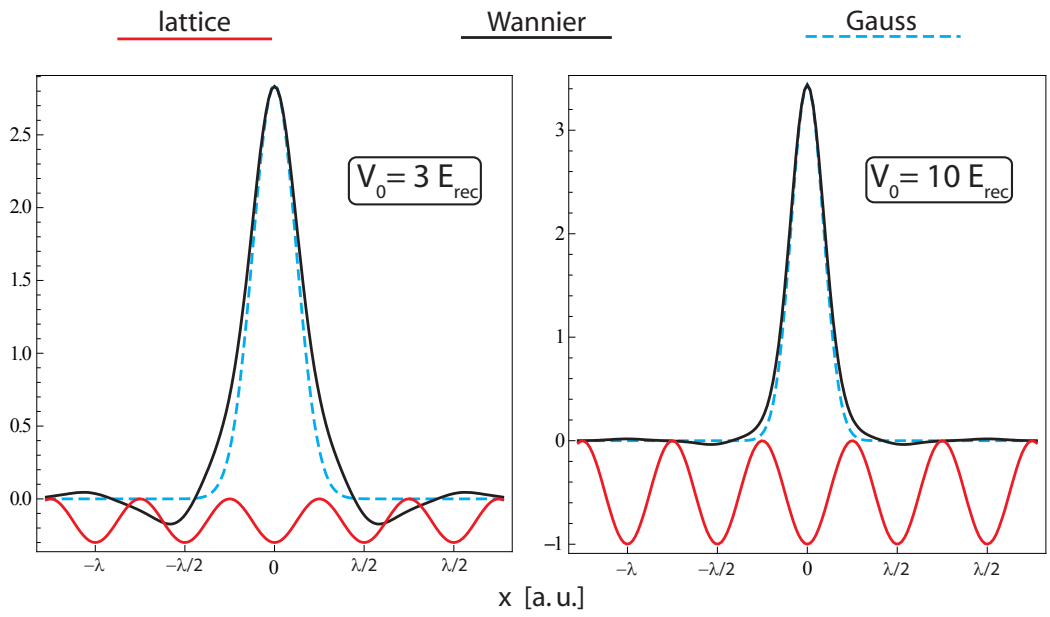

Figure 5.2: Wannier functions of the 1st band (black) for different lattice depth and ground function of harmonic potential (blue, dashed) that taylors the corresponding lattice potential at its minimum. It can be seen that the potential becomes more harmonic for deeper lattices.

now be described by $w_1[x - x_j]$. In the Bose-Hubbard model (see below) the hopping or tunneling matrix element t of a particle to a neighboring lattice site is given by [70]:

$$t \approx \frac{max(E_q^{(1)}) - min(E_q^{(1)})}{4} \tag{5.7}$$

which is the width of the 1st band divided by 4. This is not surprising since the width of the 1st band decreases with higher lattice depth (see Fig. 5.1) and one intuitively expects less tunneling for deeper lattice wells. eq. 5.7 agrees better with the exact value of t the deeper the lattice becomes [8]. For a lattice depth of 3 E_{rec} the deviation is 1.8% whereas it reduces to 0.022% for 10 E_{rec} lattice depth. Approximation eq. 5.7 always overestimates t and stays below 10% deviation with respect to the accurate value. The other important parameter of the one species Bose-Hubbard model is given by the onsite interaction U with

$$U = \frac{4\pi\hbar^2}{m} a_s \int |w_1[\mathbf{x}]|^4 d^3x \tag{5.8}$$

This term that gives the energy difference between one and two particles per site becomes bigger when the 3D-Wannier function $w_1[\mathbf{x}] = \prod_{i=x,y,z} w_1[i]$ is more localized, meaning that the nearest neighbor tails of the Wannier function which control tunneling are vanishing more and more. The factor $4\pi\hbar^2 a_s/m$ that contains the s-wave scattering length a_s can be positive (repulsive interaction as in our case) or negative (attractive interaction) and adjusts the onsite interaction strength.
The above discussion has been done for the 1D case. For the 3D-case it can be shown however that the problem decouples[1] as indicated by eq. 5.8 as long as the 3D potential can be written as sum of the 1D potentials [8]. This is always true for orthogonal optical 1D lattices with no effective mutual interferences.

5.2 The Bose-Hubbard Model

In solid state physics electrons with small energy bands in a crystal can be described by the Hubbard model [71]. This tight-binding model can for example be applied to explore physics of band magnetism, high-temperature superconductors or metal-insulator transitions (Mott-transitions). The extension of this fermionic model to bosons is called Bose-Hubbard model. Fisher

[1] This means that mathematically now new term or step shows up in the calculation. Therefore the 3D solution is known if the 1D problem is solved.

et al. [24] did this expansion in 1989 and proposed a bosonic lattice system with a superfluid and a Mott insulating phase. For lattices with disorder a third phase, the Bose glass phase, was predicted. In 1998 Jacksch et al. [26] recognized that a 3D optical lattice filled with bosons is a system that realizes the Bose-Hubbard model (BHM) and exhibits a tunability that allows one to explore the predicted phase diagram.
This chapter introduces the standard one-component BHM and the more complex and much more interesting two-component BHM.

5.2.1 The One-Component Bose-Hubbard Model

The system under study consists of ultra cold bosonic atoms in a periodic lattice with an harmonic overlying slowly varying trapping potential $V_T[\mathbf{x}]$ from the Gaussian confinement of the laser beams. In second quantization the Hamiltonian reads [26]

$$\begin{aligned}\widehat{\mathcal{H}} &= \int d^3x \;\; \widehat{\psi}^\dagger[\mathbf{x}] \left(-\frac{\hbar^2}{2m}\Delta + V[\mathbf{x}] + V_T[\mathbf{x}] \right) \widehat{\psi}[x] + \\ &\quad + \frac{1}{2}\frac{4\pi a_s \hbar^2}{m} \int d^3x \;\; \widehat{\psi}[\mathbf{x}]^\dagger \widehat{\psi}^\dagger[\mathbf{x}] \widehat{\psi}[\mathbf{x}] \widehat{\psi}[\mathbf{x}]\end{aligned} \tag{5.9}$$

with $\widehat{\psi}[\mathbf{x}]$ a bosonic field operator, a_s the s-wave scattering length of the atoms, and $V[\mathbf{x}] = V_0 \sum_{m=1}^{3} \sin^2[k_m x_m]$ the periodic potential (cf. eq. 5.3). The first term of eq. 5.9 contains the kinetic energy and the energies of the potentials one atom sees. The second term takes interactions between the bosons by the pseudo potential (see 2.1.2) into account. m is the mass of one atom. The bosonic field operator is now expanded in terms of Wannier functions (see eq. 5.6) $\widehat{\psi}[\mathbf{x}] = \sum_i \widehat{a}_i w_1[\mathbf{x} - \mathbf{x_i}]$ with the assumption that all the atoms are and stay in the lowest state or band. With this and eq. 5.9 the one-component Bose-Hubbard Hamiltonian (BHH) follows [26, 72]:

$$\widehat{\mathcal{H}}_{BH,1} = -t \sum_{\langle ij \rangle} (\widehat{a}_i^\dagger \widehat{a}_j + \widehat{a}_j^\dagger \widehat{a}_i) + \sum_i (\epsilon_i - \mu)\, \widehat{n}_i + \frac{1}{2} U \sum_i \widehat{n}_i (\widehat{n}_i - 1) \tag{5.10}$$

Generally the Hamiltonian describes no long range interactions between the bosons. These interactions are small compared to the nearest neighbor energies. Even the next nearest neighbor interactions are 2 orders of magnitude smaller than the nearest neighbor ones [26]. The terms of the one-component BHH can be understood intuitively [61].

1. **Tunneling or Hopping** - The first term of the Hamiltonian describes hopping of atoms to neighboring sites. The sum is taken over all possible nearest neighbor combinations. The scalar t gives the hopping amplitude and is evaluated by eq. 5.7 or can be approximated (for deep lattices) by $t \approx \frac{4}{\sqrt{\pi}} \mathrm{E_{rec}} (\frac{V_0}{\mathrm{E_{rec}}})^{3/4} \exp[-2\sqrt{\frac{V_0}{\mathrm{E_{rec}}}}]$ [8]. In second quantization the hopping picture translates to annihilation of an atom at site i and creation of an atom at site j. This process is expressed by the annihilation and creation operators $\widehat{a}_i$ and $\widehat{a}_j^\dagger$, respectively. The operators obey the canonical commutation relations: $[\widehat{a}_i, \widehat{a}_j^\dagger]_- = \delta_{i,j}$, $[\widehat{a}_i, \widehat{a}_j]_- = 0$ and $[\widehat{a}_i^\dagger, \widehat{a}_j^\dagger]_- = 0$.

2. **External confinement and chemical potential** - The second term of the BHH contains the energy offset of the ith lattice site, which comes from the external confinement [26]: $\epsilon_i = \int d^3x V_T[\mathbf{x}] |w_1[\mathbf{x}-\mathbf{x}_i]|^2 \approx V_T[\mathbf{x}_i]$. The last approximation is valid since the external potential V_T is only slowly varying.
   The chemical potential μ is a Lagrange multiplier that guarantees for a fixed mean particle number in a grand canonical calculation.

3. **Onsite interaction** - The last term of the Hamiltonian describes the interaction of one particle at lattice site i with all the other particles $(n-1)$. In the derivation of this term the sum is taken over several different lattice sites, but can be truncated to one because the interaction (localized Wannier functions) between the atoms is of very short range. In the tight binding regime the parameter U which is given by 5.8 can be approximated by $U \approx \sqrt{8/\pi} k a_s \mathrm{E_{rec}} (V_0/\mathrm{E_{rec}})^{3/4}$ [8]. This is done by expanding the lattice sites into harmonic potentials and correspondingly using eq. 5.8 for a Gaussian function. The onsite interaction term is the complement to t: it localizes one atom at a specific site. The ratio between U and t plays a crucial role in the phase diagram of the system that correspondingly shows two extrema. In one case the atoms are pinned at the lattice sites (Mott insulator) and in the other case they are delocalized across the whole system (superfluid phase) [73].

In the experiment the system is realized by adiabatically loading ultra cold ^{87}Rb atoms into a far red detuned optical lattice (see Chapter 4.3). The parameters U and t can easily be manipulated by changing the intensity of the back reflected light and therefore the lattice depth of the system. The deeper the lattice becomes the more the atoms are pinned at their specific lattice sites. This means that U increases and t decreases with an increasing lattice depth. It shall be pointed out again that the whole description of the system is only valid for the ground state.

The Superfluid (SF) Phase

If the onsite repulsion U goes to 0 (very shallow lattice) and the system is considered to be in its homogeneous limit ($\epsilon_i \to 0$) the ground-state wave function of the BHH can be approximated as [70]

$$|\Psi_{SF}\rangle_{t/U\to\infty} \propto \left(\sum_{i=1}^{M} \widehat{a}_i^\dagger\right)^A |0\rangle \tag{5.11}$$

A is the number of atoms in the lattice and M is the number of lattice sites. To make clear what the superfluid wave function looks like it is helpful to write it explicitly out for freely chosen numbers A and M. For the sake of simplicity I choose A=4 and M=2. The wave function than reads:

$$|\Psi_{SF}(A=4, M=2)\rangle \propto |4,0\rangle + |0,4\rangle + 4|3,1\rangle + 4|1,3\rangle + 6|2,2\rangle$$

From this example it becomes clear that every atom has the same probability to be in any lattice site. Due to the fundamental indistinguishability of the atoms, states with symmetric populations (here $|2,2\rangle$) are more likely. Effectively one atom is not pinned at one lattice site but can move freely over the entire system. Therefore the atom number at one site is completely undefined. Within a measurement one would find a random number of atoms at a lattice site with a Poisson distribution for repeating this measurement. On the other hand the phase of the state that can be described as a macroscopic wave function is well defined which can be seen by looking at the non zero order parameter $\langle \widehat{a}_i \rangle = \langle \phi_i | \widehat{a}_i | \phi_i \rangle$ [70] with ϕ_i being the wave function at lattice site i. In our example it can be seen that $\langle \widehat{a}_1 \rangle = \langle \widehat{a}_2 \rangle \neq 0$. Neglecting U the superfluid state can be written as a coherent state [61] which is an eigenstate of the annihilation operator and intrinsically exhibits a Poisson distribution.

The Mott Insulator (MI) Phase

In the other limiting case of the homogeneous system an infinitely deep lattice has to be considered. Now the ground state can be approximated as:

$$|\Psi_{MI}\rangle_{t/U\to 0} \propto \prod_{i=1}^{M} \left(\widehat{a}_i^\dagger\right)^N |0\rangle \tag{5.12}$$

This state holds as ground function for so called commensurate filling which means $N = A/M \in$ integer. For $N \notin$ integer a Mott insulating core according to eq. 5.12 with a new N being the biggest possible integer below the old N is formed. The rest of the atoms go into the SF state (eq. 5.11). To illustrate

the MI state I give the same example as for the SF one:

$$\Psi_{MI}(A = 4, M = 2)\rangle \propto |2, 2\rangle$$

This is a Fock state with 2 atoms per lattice site. In contrast to the SF case the atoms are pinned at their sites. In a measurement one always would get the same atom number per site. In general the MI state has exactly N atoms per site. The fixed atom number minimizes any phase correlation between the atoms. There are no coherences left. Again this can be seen by the order parameter $\langle \widehat{a}_i \rangle$ which becomes zero. In our example $\langle \widehat{a}_1 \rangle = \langle \widehat{a}_2 \rangle = 0$.
A further difference between the SF and the MI phase is that the MI phase has a finite gap in its excitation spectrum and is incompressible ($\partial n / \partial \mu = 0$). Deep in the MI regime the gap has the size of U.

The BH Phase Diagram

From the two previous subsections it has become clear that two extreme cases exist. In the SF phase the atoms move freely in the lattice potential and the system can be described by a macroscopic wave function. In the opposite case the atoms are confined at specific lattice sites and coherences are suppressed. With the description below eq. 5.10 it is clear that the parameters t and U that drive the transitions from the SF to the MI regime and vice versa can be adjusted by changing the depth of the optical lattice.
To get a qualitative answer to how a variation of t and U changes the ground state the phase diagram of the system has to be calculated. This can be done in a mean field approach following [72, 74, 75]. After finding the effective on-site Hamiltonian with a decoupling approximation, second order perturbation theory is applied to find the ground state energy of the system. After this the standard Landau procedure is used which yields the borders of the phases, dependent on the number of nearest neighbors in the lattice.
Fig. 5.3 shows the result of the calculation for a simple cubic lattice. The gray loops show the regions where the system is in the MI state. The phase diagram shows what one expects intuitively: in order to drive the system to the MI state a sufficiently deep lattice has to be used (t/U small enough). Furthermore it can be seen that for a high enough local chemical potential μ_i at the center of the system (yellow dot), Mott phases with different integer fillings per site can exist. The more atoms are loaded into the lattice the higher the local chemical potential at the trap center will be and consequently the higher the MI filling (labeled by N in the figure) in the center can be.

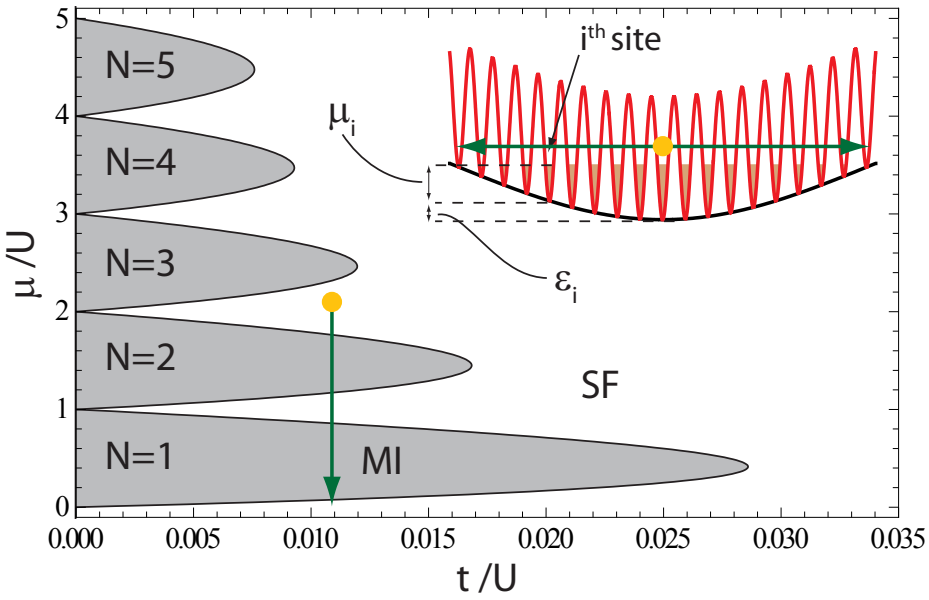

Figure 5.3: Phase diagram of one-component BHM for the three dimensional case of a simple cubic lattice (6 nearest neighbors). The drawing on the upper right shows a cartoon of the BEC in the lattice with a Gaussian envelope. The local chemical potential μ_i which leads to an onion structure (for spherical symmetry) of the system, gives a constant energy if added to the energy offset ϵ_i (compare to eq. 5.10). The two arrows (one in the phase diagram, the other one in the cartoon) show one possible way from the core to the surface of the condensate.

Measuring the Phase Transition

In chapter 4 I described theoretically and experimentally how to trap and manipulate a system of ultra cold atoms in an optical lattice. In this chapter so far I described the theoretical physics of a system of ultra cold atoms in an OL in terms of the band model and the BHM. Now these two chapters are going to be combined by performing an experiment in analogy to [23] which uses the setup described in chapter 4 within the treated theoretical frame.
The setup shown in Fig. 4.5 is used with laser light of a wavelength of 1064 nm along all three beam directions. Therefore the potentials are non state-dependent (see chapter 4.2.1). The BEC is held in the XODT in the xy-plane. Now the lattices along all three beam directions are ramped up such that the lattice depth along each direction is the same at every time. The lattice ramp is sketched in Fig. 5.4 and is exponential which takes care of the adiabaticity problem (see discussion in 4.3).
Furthermore Fig. 5.4 shows the atom cloud 18 ms after falling freely from a 3D lattice of a certain depth. The first image shows the BEC in the XODT with no optical lattice. The next image shows the atoms after being confined in a 3D OL with a depth of 3 E_{rec}. Clear diffraction peaks can be seen which indicate the the SF phase where the atom cloud can be described with a macroscopic phase that leads to coherences. The shape of the pattern can be understood by using the solid state description from 5.1. First one notices that our lattice is a simple cubic lattice. Performing TOF measurement with a long enough flight time corresponds to a Fourier transform that reveals the momentum distribution of the atoms [76]. For the solid state system under study this corresponds to a transformation from the real to the reciprocal space. Since the reciprocal lattice of a simple cubic lattice is again simple cubic, one expects a highly symmetric interference pattern. This pattern can be seen in the images and looks always the same no matter along which beam direction the absorptive image is taken. Therefore the spacing between two peaks equals $2\hbar k$ as indicated in one image, where k is the absolute value of the wave vector of the used lattice light. In the atom-light interaction picture this means that atoms in a certain peak always scattered with 2n photons where n=$\{0,1,2,...\}$.
For deeper and deeper lattice depth however the interference peaks become more and more washed out and vanish for sufficiently deep lattices. This indicates the transition of the system from the SF to the MI state. From the calculation that was used for the plot in Fig. 5.3 and the approximative formulas for t and U which are given below eq. 5.10 one can estimate the value of the lattice depth where the system starts to enter the $N = 1$ MI phase. This happens theoretically at $\sim 12E_{rec}$ (see also [8]). Indeed it becomes clear by

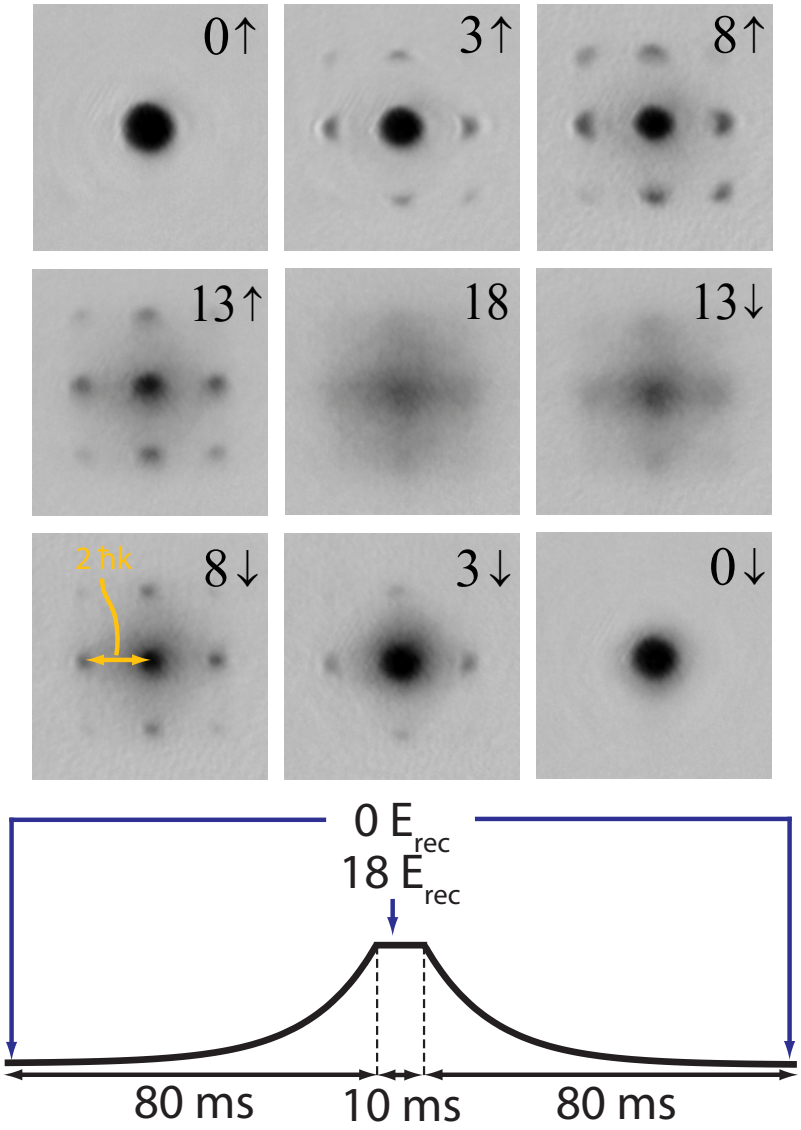

Figure 5.4: Quantum phase transition of $|F = 1, m_F = -1\rangle$ atoms. The lattice is ramped exponentially to a certain value at which all lattice and trapping beams are switched off and the atoms fall freely for 18 ms where a absorptive image is taken. The small arrows in the images that are next to the numbers which give the lattice depth (directly before dropping the cloud) in E_{rec} indicate if the lattice is ramped up or down. Where ↑ stands for up and ↓ for down. The ramp is symmetric, 170 ms long and sketched at the bottom or the figure.

looking at Fig. 5.4 that the interference peaks in the 13 E_{rec} $\uparrow$ image are less pronounced than the peaks in the 8 E_{rec} $\uparrow$ image. This can be affirmed by an evaluation of the visibility (see eq. 2.15) which is bigger for the later case. Going to an even higher lattice depth of 18 E_{rec} the peaks vanish and the system is clearly in the MI state.
The images which are taken on the the way down ($\downarrow$) show that the phase transition happened in a good approximation adiabatically because the SF phase is reentered for lower lattice depth. This proves that the image at 18 E_{rec} does not show just a thermal cloud due to heating.

5.2.2 The Two-Component Bose-Hubbard Model

In the foregoing section the one-component BHM was described theoretically and it was shown that the experimental reality agrees well with what follows from the theory. The next step is now to enrich the system by having two different hyperfine states in the frame of an OL. Interesting physics can be explored if the parameters that drive the dynamics and transitions of the system can be varied differently for each atomic hyperfine state. It is clear that the SDOL which was described in 4.5 will play an important role in doing so.

The Hamiltonian

With similar approximations as introduced for the one-component BHM one can derive a low-energy Hamiltonian in second quantization [77, 78]

$$\begin{aligned} \widehat{\mathcal{H}}_{BH,2} &= -\sum_{\langle ij\rangle,\alpha} t_\alpha(\widehat{a}^\dagger_{i,\alpha}\widehat{a}_{j,\alpha} + \widehat{a}^\dagger_{j,\alpha}\widehat{a}_{i,\alpha}) + \\ &\quad + \frac{1}{2}\sum_{i,\alpha} U_\alpha \widehat{n}_{i,\alpha}(\widehat{n}_{i,\alpha} - 1) + U_{1,2}\sum_i \widehat{n}_{i,1}\widehat{n}_{i,2} \end{aligned} \tag{5.13}$$

Comparing $\widehat{\mathcal{H}}_{BH,2}$ with $\widehat{\mathcal{H}}_{BH,1}$ of eq. 5.10 it first has to be pointed out that the same approximations (only nearest neighbor hopping, atoms in lowest Bloch band) have been made for the derivation eq. 5.13. The term that took care of the external confinement in the case of $\widehat{\mathcal{H}}_{BH,1}$ is now left out for the sake of simplicity. The main and most interesting difference between the two models however is a new term in the two-component BHM that takes care of interactions between the two different atomic species. Even though the principal meanings of the different terms of $\widehat{\mathcal{H}}_{BH,2}$ do not change compared to

$\widehat{\mathcal{H}}_{BH,1}$ it makes sense to quickly recall their meanings and point out changes.

1. **Tunneling or Hopping** - This first term is equal to the hopping term in the one-component case with the enhancement that the index α denotes a summation over the different species 1 and 2. The brackets around the letters i and j indicate the summation over adjacent lattice sites. The hopping amplitude is now part of the atomic summation and in a harmonic approximation given by $t_\alpha \approx \frac{4}{\sqrt{\pi}}\mathrm{E_{rec}}(\frac{V^{(\alpha)}}{\mathrm{E_{rec}}})^{3/4}\exp[-2\sqrt{\frac{V^{(\alpha)}}{\mathrm{E_{rec}}}}]$ where the lattice depth $V^{(\alpha)}$ equals V_0 for the atomic species α. $[\widehat{a}_{i,\alpha},\widehat{a}^\dagger_{j,\alpha}]_- = \delta_{i,j}$, $[\widehat{a}_{i,\alpha},\widehat{a}_{j,\alpha}]_- = 0$ and $[\widehat{a}^\dagger_{i,\alpha},\widehat{a}^\dagger_{j,\alpha}]_- = 0$ hold. Operators of different atomic species always commute.

2. **Onsite intra-species interaction** - The second term describes the energy that has to be used when an atom of species α is put into the same lattice well with another atom of species α. This term (and the last one) plays the complement to the delocalizing tunneling term described by t_α if all involved scattering length are positive. The onsite interaction energy is given by $U_\alpha \approx \sqrt{8/\pi}ka_s^{(\alpha)}\mathrm{E_{rec}}(V_1^{(\alpha)}V_2^{(\alpha)}V_3^{(\alpha)}/{\mathrm{E_{rec}}}^3)^{1/4}$. Here the model is slightly extended because different potentials $V_\kappa^{(\alpha)}$ are possible along the three axes of the simple cubic optical lattice[2]. $a_s^{(\alpha)}$ gives the s-wave scattering length that describes the interaction between two atoms of the same kind. Since this onsite term describes an interaction between equal atoms it is referred to as intra-species interaction. The number operator $\widehat{n}_{i,\alpha}$ is given by $\widehat{a}^\dagger_{i,\alpha}\widehat{a}_{i,\alpha}$.

3. **Onsite intra-species interaction** - The third term is the new and interesting one which does not exist in the one-component case. It describes the case when an atom of species 1 happens to sit in the same lattice well as an atom of species 2. Comparing the operator terms between intra and inter-species interaction one sees that in the first case an atom interacts with all the atoms of its species where self interaction is excluded (that is how the -1 comes in). In the second case the atom of species 1 interacts with all atoms of species 2. An exclusion of a self interaction is therefore not needed (no -1). The energy of the inter-species interaction in harmonic approximation is given by [77] $U_{1,2} = \sqrt{8/\pi}ka_s^{(1,2)}\mathrm{E_{rec}}(\overline{V}_1^{(1,2)}\overline{V}_2^{(1,2)}\overline{V}_3^{(1,2)}/{\mathrm{E_{rec}}}^3)^{1/4}$. The scattering length $a_s^{(1,2)}$ describes a collision between two atoms with two

[2]Of course also three different hopping terms for the different directions exist. In the equation for the hopping term $V^{(\alpha)}$ just has to be replaced by $V_\kappa^{(\alpha)}$

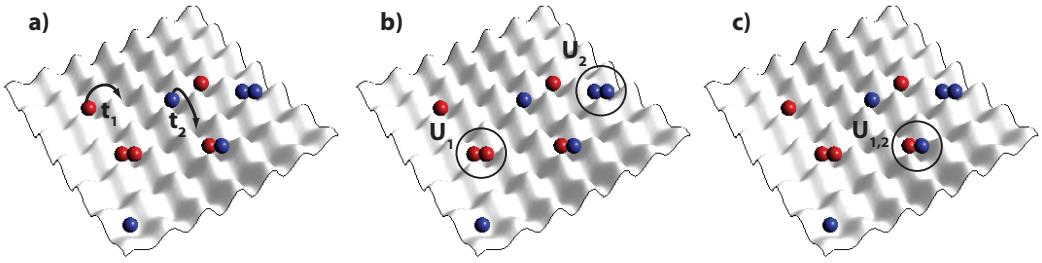

Figure 5.5: Cartoon for two-component BHM. The two different atomic hyperfine states of the atoms are shown in different colors (red and blue). a) shows the hopping of the blue and red atoms to neighboring lattice sites. Of course the atoms can not only hop to empty sites. t_1 and t_2 are the hopping amplitudes (see text). b) shows the intra-species onsite interactions of the atoms which are quantified by U_1 and U_2. c) sketches the inter-species onsite interaction. The magnitude here is given by $U_{1,2}$. This interaction between the two different species gives rise to new and interesting physics.

different internal states. The overlined lattice potentials are given by $\overline{V}_\kappa^{(1,2)} = 4V_\kappa^{(1)}V_\kappa^{(2)} / \left(\sqrt{V_\kappa^{(1)}} + \sqrt{V_\kappa^{(2)}}\right)^2$.

Fig. 5.5 shows a cartoon of the situation of two different atoms in an OL potential within the framework of the two-component BHM. In an experiment the first state could be the ^{87}Rb hyperfine ground state $|\mathrm{F} = 1, \mathrm{m_F} = -1\rangle$ (red) and the second state $|\mathrm{F} = 2, \mathrm{m_F} = -2\rangle$ (blue). These two states are chosen later for an experiment with two different types of bosons in a SDOL. Discussions of the two-component BHM and theoretical proposals for different scenarios can be found in [77–81]. It turns out that there is still (like for the one-component BHM) a transition between the SF and the MI regime but different new sub phases appear and the transition points are different.

Example: Phase Diagram Deep in the Mott Phase.

Now we will look at one very specific case which is derived in [80]. The reason for picking this special case does not lie in its theoretical importance but in its interesting results which can be achieved with a minimum of numerical computation. Therefore this section shall give a motivation why to study the two-component BHM more closely in a laboratory. Of course many more scenarios in terms of phase diagrams are (theoretically) available.
The parameters for our case are set as follows. The intra-species interaction energies U_1 and U_2 of the two different atomic species are equal and called U.

We are not in the region where the inter-species term is comparable with the intra-species one but we stay well below ($U_{1,2} < U$), nor can this theory be applied in the region where $U_{1,2}$ goes to zero. Furthermore this theory is valid deep in the MI regime (compare to 5.2.1) where the atoms are pinned down at one site. Mathematically this is described by U, $U_{1,2}$, $|U - U_{1,2}| \gg t_1$, t_2. For convenience $t_2 \leq t_1$ is taken. The calculation in [80] only holds for an odd number of atoms at each lattice site. Here we will take one atom for each site in the MI. To allow for possible checkerboard phases the lattice is divided into sublattices A and B. These two sublattices are defined that way that they build a well known NaCl structure. Now the Ansatz

$$\begin{aligned} &|\psi\rangle = \prod_{i\in A}\prod_{j\in B} |\varphi_A\rangle_i |\varphi_B\rangle_j \\ &\text{with} \\ &|\varphi_{A,B}\rangle_k = \cos\left[\theta_{A,B}/2\right]|1,0\rangle_k + \exp\left[i\phi_{A,B}\right]\sin\left[\theta_{A,B}/2\right]|0,1\rangle_k \end{aligned} \tag{5.14}$$

is used. $|n_1, n_2\rangle_k$ means n_1 and n_2 atoms of species 1 and 2 are at site k. eq. 5.14 tells that at any site there is always one atom but it can be in any coherent superposition of species 1 and 2.
A perturbative calculation leads now to an energy correction of the ground state of the MI system. This correction turns out to be [80]

$$\begin{aligned} E_{\text{corr}} \;=\; & -\frac{Nzt_1^2}{2U}\Bigg\{(1+(t_2/t_1)^2)(1+\cos[\theta_A]\cos[\theta_B]) + \\ & +(1-(t_2/t_1)^2)(\cos[\theta_A]+\cos[\theta_B]) + \\ & +(1+(t_2/t_1)^2)(1-\cos[\theta_A]\cos[\theta_B])\frac{1}{2U_{1,2}/U} + \\ & +\sin[\theta_A]\sin[\theta_B]\cos[\phi_A-\phi_B]\frac{t_2/t_1}{U_{1,2}/U}\Bigg\} \end{aligned} \tag{5.15}$$

N is the number of lattice sites and z the number of nearest neighbors. For a certain set of parameters always the state of the system with minimal energy is occupied. E_{corr} has t_2/t_1 and $U_{1,2}/U$ as parameters. Choosing numbers for these parameters within the allowed boundaries and numerically minimizing E_{corr} with respect to $\theta_{A,B}$ and $\phi_{A,B}$, yields these angles for the chosen parameters where especially $\theta_{A,B}$ is of interest. $\phi_{A,B}$ is just a phase (see eq. 5.14). Doing so one finds that three different physical cases as functions of the parameters exist.

1. **Ferromagnetic phase (FM)** - Here $\theta_A = \theta_B = 0$. According to eq. 5.14 all atoms are in the state $|1,0\rangle$. This reminds one of a ferromagnet where the magnetic spins are all well aligned in their Weiss domain. The breaking of symmetry (why not $|0,1\rangle$?) happens because $t_2 \leq t_1$ has been chosen above.

2. **Antiferromagnetic phase (AF)** - This phase is described by $\theta_{A(B)} = 0 \wedge \theta_{B(A)} = \pi$. This phase shows that the sublattices A and B were not introduced without any reasoning. One sublattice is filled with atoms of the first species the other one with atoms of the second kind. Therefore the system looks like a three dimensional checkerboard.

3. **XY phases** - Here the plural is used because the angles do not have as clear restrictions: $\theta_A = \theta_B \neq 0$. This means the atoms in this phase are in coherent superpositions of $|1,0\rangle$ and $|0,1\rangle$ with varying parts of both as a function of t_2/t_1 and $U_{1,2}/U$ in the XY region.

Fig. 5.6 shows the calculated phase diagram of the described situation. It can be calculated as described with eq. 5.15. The phase transitions between the phases are found with a simple bisection algorithm.
The discussed phase diagram covers only the deep MI regime. In [80] however diagrams showing transitions from different SF to the discussed MI phases are calculated. Interesting scenarios like one species being in the MI state while the other one still remains in the SF state can exist. Looking at Fig. 5.6 three general questions arise:

1. The first one regards the experimental realization. From an experimental point of view it has to be pointed out that realizing a system under the above conditions is challenging. Since the hopping rate (in recoil energy units) of one species does not depend on the lattice direction, the lattice depths $V^{(1)}$ and $V^{(2)}$ can be chosen differently from each other but have to be the same along every lattice direction, respectively. The onsite energies given in the discussion below eq. 5.13 therefore reduce to $U_1 \propto a_s^{(1)}(V^{(1)})^{3/4}$, $U_2 \propto a_s^{(2)}(V^{(2)})^{3/4}$ and $U_{1,2} \propto a_s^{(1,2)}\left(4V^{(1)}V^{(2)}/\left(\sqrt{V^{(1)}}+\sqrt{V^{(2)}}\right)^2\right)^{3/4}$. To explore the calculated phase diagram the ratio between $U_{1,2}$ and $U = U_1 = U_2$ and the ratio between t_2 and t_1 have to be scanned. To scan the ratio between the hopping rates the lattices depths have to be changed. This could be done by changing the polarization of the lattice light (see Fig. 4.12). However, to guarantee that $U_1 = U_2$ stays valid, the scattering lengths

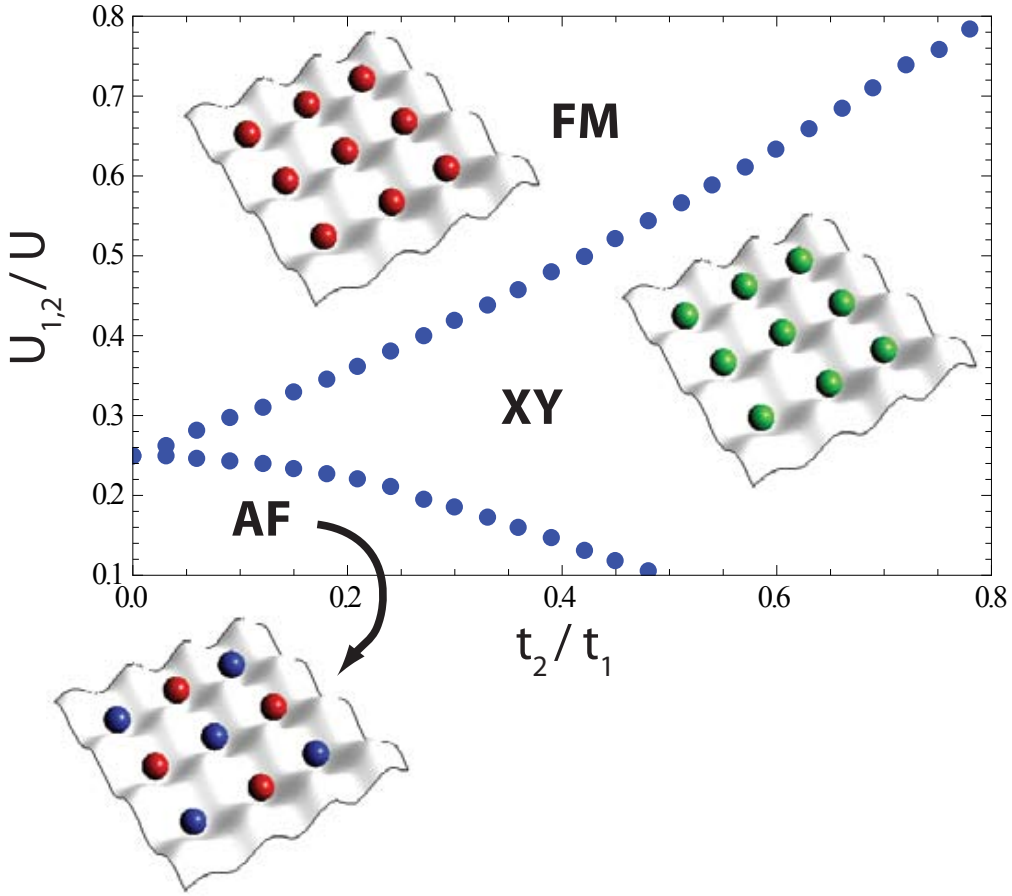

Figure 5.6: Two-component BHM phase diagram deep in the MI phase with exactly one atom per lattice site (more details: see text). The different phases are illustrated with small lattice cartoons. The point where all three phases meet sits at $t_2/t_1 = 0$ and $U_{1,2}/U = 0.25$.

$a_s^{(1)}$ and $a_s^{(2)}$ must be changed correspondingly. This can be done by Feshbach resonances (see 6.4). However it is not clear how one can drive two different Feshbach resonances at one time. When changing the lattice depths, $U_{1,2}$ is also modified. Another option might be to shift the lattices of species one and two with respect to each other [27]. Therefore all phases of the diagram could be explored. For a more general discussion of an experimental realization of theories in our system see 6.4.

2. The second question is how one would measure these phases if the system is realized experimentally? The answer is simple [80]: A TOF measurement in combination with a Stern-Gerlach pulse is used (see 2.2 and 2.3). Having two hyperfine states with different magnetic moments, the two species would separate. In our case the FM phase would be revealed by only having one cloud after applying the described method. In the AF case two clouds with equal atom numbers would exist whereas the ratio of the two clouds in the XY case would be arbitrary. These statements are only valid as long as the system is not inhomogeneous, such that different phases cannot exist for one set of parameters. This gives rise to the third question.

3. The third question is more fundamental and difficult. It is well known that the total spin number S_z of a closed system has to be conserved. The two-component BHM is equivalently described by labeling the two atomic species as spins (e.g. $\uparrow$ and $\downarrow$). If one now starts with a FM ($N_\uparrow \neq N_\downarrow = 0 \rightarrow S_z^{\mathrm{FM}} = N_\uparrow$) how could one for instance drive a transition down to the AF phase (compare Fig. 5.6) by varying the lattice parameters, although the total spin is not conserved ($N_\uparrow = N_\downarrow \rightarrow S_z^{\mathrm{AF}} = 0$)? One possible answer could be that the system has an inhomogeneity that is big enough that different parameters of the phase diagram at different places are realized. But still the question remains what happens in a rather homogeneous experimental case? And could the spin conservation problem suppress a phase transition or do other effects (e.g. Einstein-de Haas effect which describes a transfer to orbital angular momentum [82]) happen?

These are very interesting questions which complete the motivation why the two-component BHM should be studied experimentally. The following chapter will describe our first steps towards the experimental realization of such a system.

Chapter 6

State-dependent two-component Superfluid - Mott insulator transition

In the last chapter the functionality of our machine has been shown by repeating the one-component SF-MI transition [23]. Furthermore theoretical models like the band model and the one and two-component BHM have been discussed. It has been pointed out that theoretical predictions promise interesting new physics in the case of the two-component BHM. In 4.2, 4.3, 4.4 and 4.5 the specific experimental features like the XODT and the lattices (state-independent and state-dependent) have been probed, both theoretically and experimentally. This means the needed experimental conditions for a lattice experiment with two bosonic species in an OL are available.

6.1 Observing the phase transition

A BEC in the $|\mathrm{F} = 1, \mathrm{m_F} = -1\rangle$ state is prepeared in the XODT. Now three different cases are probed. In the first one, the BEC stays in its original state. In the second, the BEC is put into a coherent superposition between $|\mathrm{F} = 1, \mathrm{m_F} = -1\rangle$ (red state) and $|\mathrm{F} = 2, \mathrm{m_F} = -2\rangle$ (blue state) by applying a microwave pulse which drives a resonant Rabi coupling between the two states (see 2.3.1). In the third case, the atoms are transfered completely into the blue state by a Rabi pulse.
The following procedure is the same for every case: 4 ms after applying the Rabi pulse the 3D lattice is exponentially ramped to a certain value. Now the 3D lattice is switched off and the atoms are imaged after a TOF of 18 ms. Directly after switching the lattice off, a magnetic Stern-Gerlach pulse that

separates blue and red atoms is applied. The 3D lattice consists of two 1064 nm lattices in the xy-plane along the ODT1 and ODT2-directions (compare Fig 4.5) and a state-dependent lattice at 785 nm (σ^+-polarized) along the z-direction (see Fig. 4.13). The lattice depth at any point in time is the same for all directions[1]. Fig. 6.1 shows the data. Looking at the left column it can be seen that the red state undergoes a phase transition from SF to MI just like in Fig. 5.4. This is not surprising and there is no new physics compared to Fig. 5.4. Again the separation of the interference peaks equals $2\hbar k$. Since the imaging direction is along OL1 one can see that the vertical peak separation is bigger than the horizontal one, with a ratio of 1064/785.
The case of having only blue atoms (right column) is perhaps more interesting. In good agreement with Fig. 4.15 the $|\mathrm{F}=2,\mathrm{m_F}=-2\rangle$ state does nearly not see the 785 lattice. The BEC therefore stays in the 2D SF state which is formed by the 1064 lattice. Comparing the red and the blue BEC in the left and right column one sees that the blue BEC on the end of the ramp (a↓)) is much clearer than the red one. This could be explained by the state-dependent scattering rates (see Fig. 4.17). For σ^+-light at 785 nm the scattering rate of the red atoms equals 2.7 times the scattering rate of the blue ones. Therefore more heating in the red case is expected.
The most interesting case is shown in the middle column. Here 50% of the atoms are in the red and 50% are in the blue state. At point c) in Fig. 6.1 the red state sees the full lattice in all directions while the blue state only sees a non-neglegible lattice in the xy-plane. Consequently the red state goes to the MI phase while the blue one stays in the SF phase at the same time. Therefore this is the first state-dependent SF-MI transition of 2 inter-convertible species of bosons in one lattice where one species stays in the SF phase while the other one goes into a MI. This proves that the high scattering rate of the 785 light (see 4.5.2) is not a limiting factor for such an experiment.
Looking at the top of Fig. 6.1 one recognizes that the atoms in the middle column initially have been driven to a coherent superposition between the $|\mathrm{F}=2,\mathrm{m_F}=-2\rangle$ and the $|\mathrm{F}=1,\mathrm{m_F}=-1\rangle$ state. However in the text above a 50:50 mixture which is indeed statistical was mentioned. This mismatch is explained with Fig. 6.2. It can be seen that atomic spins decohere within a timescale of a few ms. With a spin echo pulse the coherence time can be increased up to a few 10 ms, but this is still on a smaller timescale than the applied lattice ramp.
Fig. 6.2 shows that the fraction of $|\mathrm{F}=1,\mathrm{m_F}=-1\rangle$ atoms does not equilibrate at 0.5 but at a lower value. This could be because the microwave frequency

[1]This means the depth measured in $\mathrm{E_{rec}}$ is the same in every direction. The recoil energy depends on the light used in the considered direction.

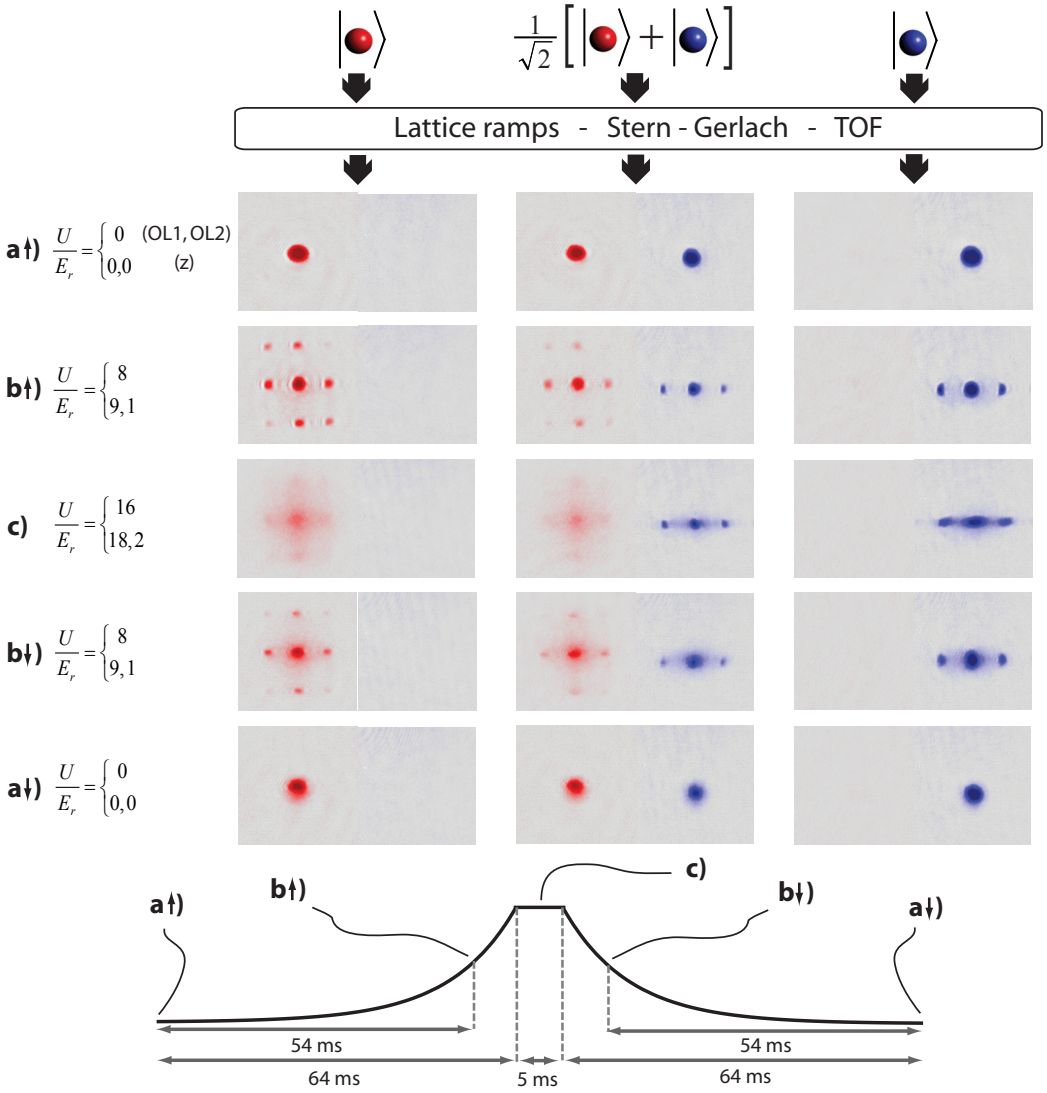

Figure 6.1: State-dependent SF-MI transition. The first column shows only $|\mathrm{F}=1,\mathrm{m_F}=-1\rangle$ (red) and the third column only $|\mathrm{F}=2,\mathrm{m_F}=-2\rangle$ (blue). The second column shows a 50:50 mixture between red and blue. Note that each of the 15 pairs of images is a single shot. The first value behind the curly braces gives the state-independent 1064 nm lattice depth in OL1 and OL2-direction. The second and third value behind the curly braces give the 785 nm lattice depths for the red state and the blue state, respectively. Again all energies are given in units of $\mathrm{E_{rec}}$ with respect to the considered wavelength. At the bottom the symmetric lattice ramp with the drop points of the data (for instance a↓) is shown. All images are taken along the OL1 direction.

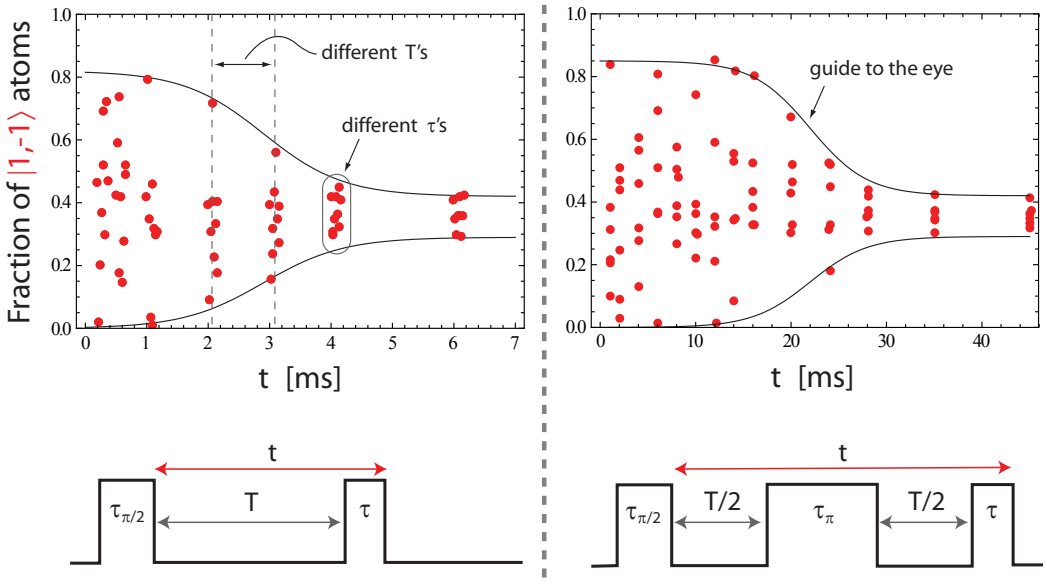

Figure 6.2: Decoherence of coherent superposition state. The atoms are put into $1/\sqrt{2}(|\mathrm{F}=2,\mathrm{m_F}=-2\rangle+|\mathrm{F}=1,\mathrm{m_F}=-1\rangle)$ by a $\pi/2$-pulse. After a hold time t they are sampled by different short Rabi pulses of lenght τ that cover a full Rabi oscillation. The difference between the right and the left data set is that a spin echo sequence [83] was implemented into the right one.

might not exactly hit the atomic resonance (see eq. 2.13). Besides time-dependent magnetic fields, the exact length of the first applied Rabi pulse and technical issues (imaging) play a role, too.
Therefore Fig. 6.1 shows a statistical mixture of red and blue bosons in the middle column because the ramp time is much bigger than the decoherence time.

6.2 Separation of Species

In the recent time there have been discussions and experiments on how Bose-Fermi mixtures in optical lattices behave [84–87]. For instance there are theoretical proposals how the presence of fermions would influence the SF-MI transition [86]. Such an effect is also expected for our two boson mixture experiment (Fig. 6.1). Here a suppression of the MI is expected [88]. This can be understood if one thinks about the role of the blue atoms that do not undergo a phase transition into the MI state but stay superfluid. These atoms interact with the red atoms which are more and more confined when ramping up the state-dependent 785 nm lattice. But there still will be a higher[2] effective hopping term of the red atoms because they can use the blue atoms as "medium". This would lead to an enhancement of the SF phase.
Experimentally, we try to explore this effect by comparing the scenario shown in the left column of Fig. 6.1 where only red atoms exist with the scenario in the middle column where red and blue atoms (ratio 1:1) are trapped. The visibility (compare 2.3.3) of the red atoms is evaluated for both cases. The lattice ramp is exponential and switched off at certain depths[3] (see Fig. 6.3) on the way up. The ramp time for maximum lattice depth is 100 ms. Since the visibility is a measure of coherence it tells when the SF phase is left behind and the MI phase is entered (visibility goes from 1 to 0). Fig. 6.3 shows the data.
It is guaranteed that atom number of the red state does not affect the measurement. Therefor in any case the atoms are put into a 50:50 mixture by a microwave pulse (compare 2.3.1) while they are confined in the pure XODT.
The green data (joined by dashed green line) is now measured by performing the above described experiment.
For the red data (joined by red solid line) the $|\mathrm{F}=2,\mathrm{m_F}=-2\rangle$ atoms (blue state) are blown away by a 100 μs cycling light pulse (see Fig. 3.1). This is done with a small magnetic gradient that separates the species such that

[2]Compared to the one-component case.

[3]The lattice depth is for all three directions about the same in corresponding recoil energy units.

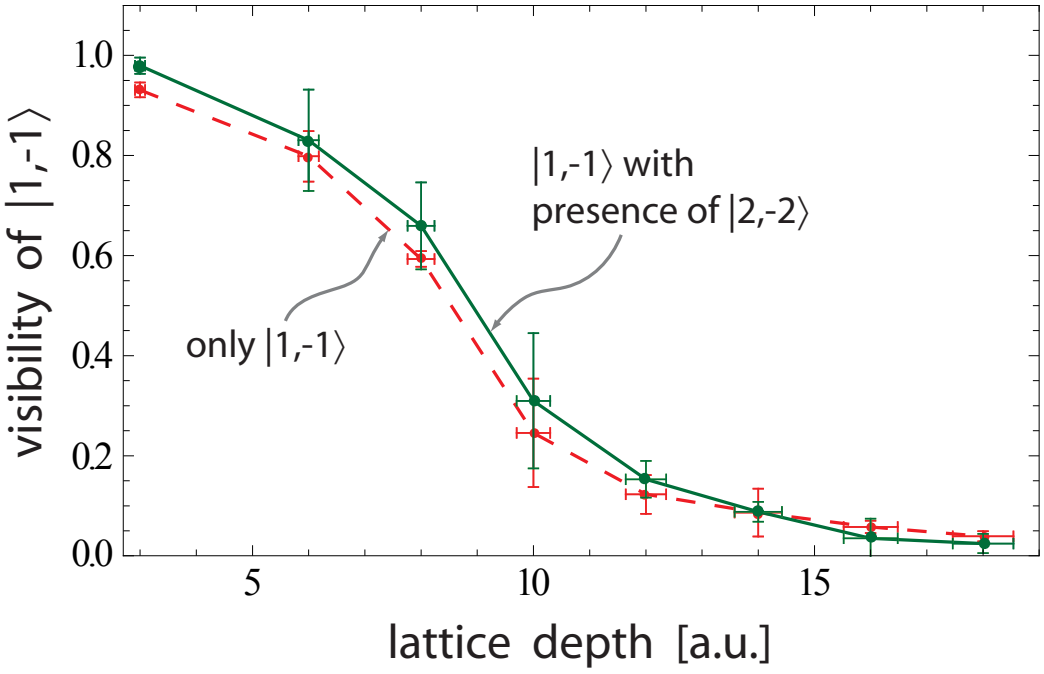

Figure 6.3: Measurement of visibility in a two-component scenario. The red points show the visibility as a function of the lattice depth the red atoms see, for the case of a normal one-component $|\mathrm{F}=1,\mathrm{m_F}=-1\rangle$ BEC (red state, dashed line) as starting point. The lattice depth is given in arbitrary units because of calibration issues. The green data points show the visibility of the red state in presence of the blue state. Each data point is measured three times. The error of the visibility arises from the standard deviation of these three measurements. The error of the lattice depth is estimated with 3%. The lines are guides to the eye.

heating of the red state is minimized.
In both cases the data are taken after a Stern-Gerlach pulse to separate the two-components for imaging and a TOF of 18 ms. Fig. 6.3 shows that there seems to be no fundamental difference between only red atoms in the system that undergo the phase transition and red atoms that undergo the phase transition in the presence of a superfluid blue background.
One reason for this could lie in residual magnetic gradients that pull the blue and the red state apart ($\sim$ ms). Therefore the system would not really be a two-component system but the red state would sit in one part of the lattice and the blue one in the other part.
However, this spatial separation due to different magnetic moments of the states is minimized by nulling the magnetic field gradient at the BEC position with gradient coils. Doing so, partial spatial overlaps of the two states up to 2 s have been achieved. The shown visibility data was measured under such conditions.
Another problem might occur if the 785 nm beam is slightly misaligned, has a non Gaussian internal structure, or an internal polarization profile. In this case the beam which is only talking to the red atoms[4] will separate the states, too. In the following section such a beam misalignment is simulated.

6.3 Simulation of misaligned 785 nm beam

As described in the preceding section the experimental problem of a spatial separation of the atomic species in the XODT was found. Besides residual magnetic field gradients at the BEC position, a misalignment of the 785 beam also leads to a separation of the species. Fig. 6.4 shows the result of a simple classical calculation. It is assumed that the 785 beam is misaligned but still propagates along the z′-direction (see Fig. 4.5). This beam with a smallest waist of 230 μm at $x' = y' = \Delta z' = 0$ is ramped up exponentially to 200 mW in 50 ms and then held at constant power. The atoms are assumed to be in the red state. Before the 785 beam is ramped up, they are sitting at the 1064 nm XODT minimum with the fixed parameters of Fig. 4.3. The calculation is done under the simplification that there is no interaction between the atoms. The calculation is a classical one and based on a numerical solution of Newton's equations for the center of mass of the BEC in the given beam potentials (time-dependent for the z- beam).
This means that in none of the three directions a lattice is implemented. For

[4] An internal polarization profile leads to a non-zero potential seen by the blue state.

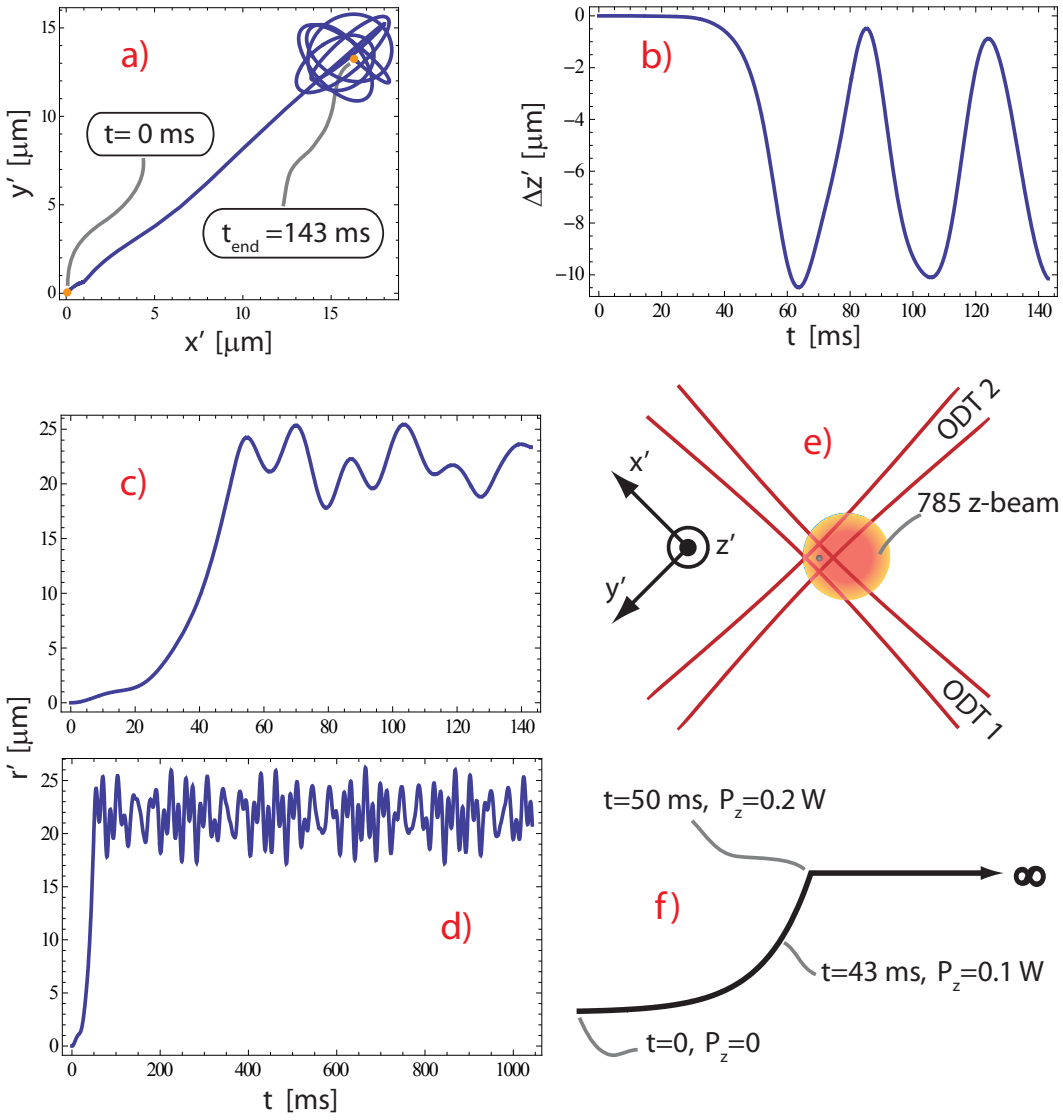

Figure 6.4: Simulation of misaligned z-beam. The misaligned 785 z-beam is ramped up on the atoms in the $|\mathrm{F} = 1, \mathrm{m_F} = -1\rangle$ state, which are sitting in the XODT. Part a) shows the displacement of the atoms in the XODT-plane. b) shows the time resolved displacement in the z′-direction. Part c) and d) illustrate the radial displacement for short and long timescales, where $\mathrm{r}' = \sqrt{(\mathrm{x}')^2 + (\mathrm{y}')^2 + (\Delta \mathrm{z}')^2}$. $\Delta \mathrm{z}' = 0$ marks the BEC equilibrium z′-position if there is no 785 z-beam, and grows in the negative direction if the BEC falls. e) is a cartoon of the XODT and the misaligned z-beam and f) shows the used exponential ramp. For more information see text.

the implementation of a lattice one would have to consider the band model (see 5.1) in a dynamical way which would complicate the calculations immensely. For the shown figure the displacement of the 785 beam was chosen to be 30 μm away from both ODT axes.
Fig. 6.4 shows the separation between the red and the blue species because the blue atoms do not see the 785 light. The position of the blue species is $x' = y' = \Delta z' = 0$. The oscillations of the plots in the figure never decay. This is because no damping was inserted into the equations. In the real experiment the spacial oscillations will damp out because of interactions between the atoms which finally leads to a heating of the BEC. For the shown calculations this would lead to a heating of the BEC of 10 nK, with the assumption that there is no energy transfer to the blue atoms. This also leads to an atom loss mainly along the z′-direction. Part a) and b) show that the amplitudes of the oscillations along the x′ and the y′-direction are by a factor of ~ 2 smaller than the amplitude of the z′-signal. The reason for this is the confinement of the trap along the z′-direction (see Fig. 4.3) which is weak compared to the confinement in the x′y′-plane. Furthermore by looking at b) and c) it can be seen that the oscillation along all directions start around the same time. This and the non harmonic oscillation shapes of the curves indicate the anharmonicity of the potential. It turns out that there is a strong coupling between the x′ and the z′, and the y′ and the z′-direction but a weak one between the x′ and the y′-direction. A similar effect has been observed for XODT trap frequency measurement shown in Fig. 4.4. All oscillation periods differ from the ones which have been calculated for Fig. 4.3. There are two reasons for this. First, the simulated oscillation is not harmonic (as discussed above), and second the trap point of equilibrium has changed due to the misaligned beam. This also changes the oscillation frequency along the z′-direction. A change of the confinement along this direction because of the z-beam itself can be neglected since the Rayleigh range of the beam is ~ 20 cm. All statements made in this clause are qualitatively true, independent of specific simulation parameters.
In conclusion the simulation has shown that under simplified conditions the separation of the species always happens on the timescale of the 785 ramp (see parts c) an f)). This however will not hold for the case of an added 3D lattice ramp. Here the separation will occur on a slower timescale, especially for deep lattices and will stop if the MI phase is reached before the BEC went to its above calculated equilibrium position. If this is not the case separation of the species will be the same as the calculated one if one applies the suggested technique (see Fig. 4.8) in order to keep the external confinement constant. Another 785 beam effect that leads to a separation of the species is an internal non Gaussian structure (fringes, etc.) of the beam. There are indications that

this could be the case in our setup.
Therefore the challenge in the near future will be to increase the spatial overlap of the two species by upgrading the properties and the alignment of the 785 beam. With spatial overlap of the two states in the lattice, a clear effect on the visibility of the red state is expected.

6.4 Comparison with Theory and Outlook

In general comparison with sophisticated models [77–81] is not straightforward. There are several reasons for this. Some theoretical proposals do simply not fit to our experimental possibilities. For instance [89] requires heteronuclear bosons. But even for porposals that seem to fit our system quite well [77, 80] challenges occur. To the best of my knowledge, to date there is no paper that discusses the case of equal lattice spacing along two directions (here 1064 nm lattice) but a different spacing along the third direction (785 nm lattice). The extension of the existing theories to this case seems to be non-trivial, since the symmetry of the system is broken which for instance has its manifestation in different hopping amplitudes of one species for different directions. However equal hopping rates along all directions in our setup can experimentally be achieved via adjusting the 785 and 1064 lattice depths.
Effects of the experimentally indispensable external confinement are often ignored in theoretical treatments. This confinement however might lead to different phases for one specific system with fixed parameters and raises the question how one experimentally can distinguish different cases. One experimental attempt could be to try to reduce the external confinement. This procedure however has boundaries which will be reached quickly in our setup. Other theoretical restrictions like a fixed chemical potential for both species or certain filling factors in principle hinder direct comparisons.
On the other hand, it is likely that fundamental properties like new (in comparison to the one-component case) phases still can be seen with our system. But even if a direct comparison to theory might not be our aim challenges still exist. To explore different phases in a phase diagram it is necessary to have access to the parameters that drive the transitions. In 5.2.2 it is shown that all parameters depend on V_0. Therefore the lattice depth that can simply be varied by changing the lattice laser intensity as an important parameter for scanning through the phase diagram. Shifting the lattices for the two different species with respect to each other [27] can lead to interesting scenarios, too.
All onsite interaction terms in eq. 5.13 depend on scattering lengths. Looking at Fig. 5.6 one might want to change the ratio of the inter-species and intra-species interaction in order to try to drive a phase transition from the FM to

the AF phase. The scattering lengths could be changed via Feshbach resonances [30, 90, 91]. For ^{87}Rb these resonances are experimantally not easily accessible [92, 93]. But the ratio of the interaction terms is experimentally well accessible by tuning the lattice depths and the relative position of the atoms (by shifting the SDOL [27]). New phases are expected to be seen clearly for unequal scattering lengths. This is intuitively clear because one important difference between the one and the two-component BHM is the inter-species interaction which significantly changes the scenario if it is preferably unequal to the intra-species interaction energy. The phase diagram shown in Fig. 5.6 for instance is not valid for $U \approx U_{1,2}$. The scattering lengths of the ^{87}Rb states of interest ($|\mathrm{F} = 2, \mathrm{m_F} = -2\rangle$ and $|\mathrm{F} = 1, \mathrm{m_F} = -1\rangle$) are all ~ 100 $\mathrm{a_0}$ [94]. This could impede the research on new phases. One advantage of our system over a system with two different bosonic [95] atoms, however, is that we can inter-convert the atomic states.
In conclusion, challenging future experiments have the potential to reveal new interesting physics.

Chapter 7

Conclusion

We have done the first two-component state-dependent SF-MI transition with dilute ^{87}Rb quantum gas and thereby proved that the high scattering rate of light that forms state-dependent potentials, is in principle not a limiting factor for such an experiment.
Furthermore we have discussed the properties of the XODT alone and in connection with back reflected light that leads to the OL1 and OL2 potentials, and can affect the envelope shape of the dipole trap. A reliable method for lattice calibration has been introduced.
We have performed measurements on the basis of state-dependent potentials and scattering rates in good agreement with theory and have shown the reliability of the BEC machine by driving the system to a one-component SF-MI transition.
The next steps will include a search for interactions between the two used hyperfine species in the two-component case. This will be done by increasing the spatial overlap between the two species.

Bibliography

[1] Franco Dalfovo, Stefano Giorgini, Lev P. Pitaevskii, and Sandro Stringari. Theory of Bose-Einstein condensation in trapped gases. *Rev. Mod. Phys.*, 71(3):463–512, Apr 1999. doi: 10.1103/RevModPhys.71.463.

[2] W. Ketterle, D. S. Durfee, and D. M. Stamper-Kurn. Making, probing and understanding Bose-Einstein condensates, 1999. URL http://www.citebase.org/abstract?id=oai:arXiv.org:cond-mat/9904034.

[3] A. L. Schawlow and C. H. Townes. Infrared and optical masers. *Phys. Rev.*, 112(6):1940–1949, Dec 1958. doi: 10.1103/PhysRev.112.1940.

[4] H. J. Metcalf and P. van der Straten. *Laser Cooling and Trapping*. Springer, 1999.

[5] M. R. Matthews C. E. Wieman M. H. Anderson, J. R. Ensher and E. A. Cornell. Observation of Bose-Einstein condensation in a dilute atomic vapor. *Science*, 269:198–201.

[6] C. C. Bradley, C. A. Sackett, J. J. Tollett, and R. G. Hulet. Evidence of bose-einstein condensation in an atomic gas with attractive interactions. *Phys. Rev. Lett.*, 75(9):1687–1690, Aug 1995. doi: 10.1103/PhysRevLett.75.1687.

[7] K. B. Davis, M. O. Mewes, M. R. Andrews, N. J. van Druten, D. S. Durfee, D. M. Kurn, and W. Ketterle. Bose-einstein condensation in a gas of sodium atoms. *Phys. Rev. Lett.*, 75(22):3969–3973, Nov 1995. doi: 10.1103/PhysRevLett.75.3969.

[8] Immanuel Bloch, Jean Dalibard, and Wilhelm Zwerger. Many-body physics with ultracold gases. *Reviews of Modern Physics*, 80(3):885, 2008. doi: 10.1103/RevModPhys.80.885. URL http://link.aps.org/abstract/RMP/v80/p885.

[9] Dallin Durfee and Wolfgang Ketterle. Experimental studies of Bose-Einstein condensation. *Opt. Express*, 2(8):299–313, 1998. URL http://www.opticsexpress.org/abstract.cfm?URI=oe-2-8-299.

[10] K. I. Petsas, A. B. Coates, and G. Grynberg. Crystallography of optical lattices. *Phys. Rev. A*, 50(6):5173–5189, Dec 1994. doi: 10.1103/PhysRevA.50.5173.

[11] R. Grimm, M. Weidemüller, and Y. B. Ovchinnikov. Optical dipole traps for neutral atoms. *Advances in Atomic, Molecular and Optical Physics*, 42, 1999.

[12] C. I. Westbrook, R. N. Watts, C. E. Tanner, S. L. Rolston, W. D. Phillips, P. D. Lett, and P. L. Gould. Localization of atoms in a three-dimensional standing wave. *Phys. Rev. Lett.*, 65(1):33–36, Jul 1990. doi: 10.1103/PhysRevLett.65.33.

[13] P. S. Jessen, C. Gerz, P. D. Lett, W. D. Phillips, S. L. Rolston, R. J. C. Spreeuw, and C. I. Westbrook. Observation of quantized motion of rb atoms in an optical field. *Phys. Rev. Lett.*, 69(1):49–52, Jul 1992. doi: 10.1103/PhysRevLett.69.49.

[14] A. Hemmerich and T. W. Hänsch. Two-dimesional atomic crystal bound by light. *Phys. Rev. Lett.*, 70(4):410–413, Jan 1993. doi: 10.1103/PhysRevLett.70.410.

[15] G. Grynberg, B. Lounis, P. Verkerk, J.-Y. Courtois, and C. Salomon. Quantized motion of cold cesium atoms in two- and three-dimensional optical potentials. *Phys. Rev. Lett.*, 70(15):2249–2252, Apr 1993. doi: 10.1103/PhysRevLett.70.2249.

[16] Maxime Ben Dahan, Ekkehard Peik, Jakob Reichel, Yvan Castin, and Christophe Salomon. Bloch oscillations of atoms in an optical potential. *Phys. Rev. Lett.*, 76(24):4508–4511, Jun 1996. doi: 10.1103/PhysRevLett.76.4508.

[17] Qian Niu, Xian-Geng Zhao, G. A. Georgakis, and M. G. Raizen. Atomic Landau-Zener tunneling and wannier-stark ladders in optical potentials. *Phys. Rev. Lett.*, 76(24):4504–4507, Jun 1996. doi: 10.1103/PhysRevLett.76.4504.

[18] S. R. Wilkinson, C. F. Bharucha, K. W. Madison, Qian Niu, and M. G. Raizen. Observation of atomic Wannier-Stark ladders in an accelerating

optical potential. *Phys. Rev. Lett.*, 76(24):4512–4515, Jun 1996. doi: 10.1103/PhysRevLett.76.4512.

[19] J. Feldmann, K. Leo, J. Shah, D. A. B. Miller, J. E. Cunningham, T. Meier, G. von Plessen, A. Schulze, P. Thomas, and S. Schmitt-Rink. Optical investigation of bloch oscillations in a semiconductor superlattice. *Phys. Rev. B*, 46(11):7252–7255, Sep 1992. doi: 10.1103/PhysRevB.46.7252.

[20] A. R. Kolovsky, A. V. Ponomarev, and H. J. Korsch. Damped Bloch oscillations of cold atoms in optical lattices. *Phys. Rev. A*, 66(5):053405, Nov 2002. doi: 10.1103/PhysRevA.66.053405.

[21] M. Gustavsson, E. Haller, M. J. Mark, J. G. Danzl, G. Rojas-Kopeinig, and H.-C. Nägerl. Control of interaction-induced dephasing of Bloch oscillations. *Physical Review Letters*, 100(8):080404, 2008. doi: 10.1103/PhysRevLett.100.080404. URL http://link.aps.org/abstract/PRL/v100/e080404.

[22] C. Orzel, A. K. Tuchman, M. L. Fenselau, M. Yasuda, and M. A. Kasevich. Squeezed states in a Bose-Einstein condensate. *Science*, 291, March 2001.

[23] Greiner Markus, Mandel Olaf, Esslinger Tilman, Hansch Theodor W., and Bloch Immanuel. Quantum phase transition from a superfluid to a mott insulator in a gas of ultracold atoms. *Nature*, 415(6867), 2002.

[24] Matthew P. A. Fisher, Peter B. Weichman, G. Grinstein, and Daniel S. Fisher. Boson localization and the superfluid-insulator transition. *Phys. Rev. B*, 40(1):546–570, Jul 1989. doi: 10.1103/PhysRevB.40.546.

[25] Ivan H. Deutsch and Poul S. Jessen. Quantum-state control in optical lattices. *Phys. Rev. A*, 57(3):1972–1986, Mar 1998. doi: 10.1103/PhysRevA.57.1972.

[26] D. Jaksch, C. Bruder, J. I. Cirac, C. W. Gardiner, and P. Zoller. Cold bosonic atoms in optical lattices. *Phys. Rev. Lett.*, 81(15):3108–3111, Oct 1998. doi: 10.1103/PhysRevLett.81.3108.

[27] Olaf Mandel, Markus Greiner, Artur Widera, Tim Rom, Theodor W. Hänsch, and Immanuel Bloch. Coherent transport of neutral atoms in spin-dependent optical lattice potentials. *Phys. Rev. Lett.*, 91(1):010407, Jul 2003. doi: 10.1103/PhysRevLett.91.010407.

[28] Olaf Mandel, Markus Greiner, Artur Widera, Tim Rom, Theodor W. Hänsch, and Immanuel Bloch. Controlled collisions for multi-particle entanglement of optically trapped atoms. *Nature*, 425(1):010407, October 2003.

[29] Kerson Huang. *Statistical mechanics*. John Wiley & sons, second edition.

[30] C. J. Pethick and H. Smith. *Bose-Einstein condensation in dilute gases*. Cambridge University Press, 2002.

[31] M.-O. Mewes, M. R. Andrews, N. J. van Druten, D. M. Kurn, D. S. Durfee, and W. Ketterle. Bose-Einstein condensation in a tightly confining dc magnetic trap. *Phys. Rev. Lett.*, 77(3):416–419, Jul 1996. doi: 10.1103/PhysRevLett.77.416.

[32] Stephan Albert. *Cooling, Trapping, and Transport of Atom Clouds in a New BEC Apparatus*. Master's thesis, Stony Brook University, 2007.

[33] Daniel Greif. *Evaporative cooling and Bose-Einstein Condensation of Rb-87 in a moving-coil TOP trap geometry*. Master's thesis, Stony Brook University, 2007.

[34] P. W. Milonni and J. H. Eberly. *Lasers*. John Wiley and Sons, 1988.

[35] I. I. Rabi. Space quantization in a gyrating magnetic field. *Phys. Rev.*, 51(8):652–654, Apr 1937. doi: 10.1103/PhysRev.51.652.

[36] Jan R. Rubbmark, Michael M. Kash, Michael G. Littman, and Daniel Kleppner. Dynamical effects at avoided level crossings: A study of the Landau-Zener effect using Rydberg atoms. *Phys. Rev. A*, 23(6):3107–3117, Jun 1981. doi: 10.1103/PhysRevA.23.3107.

[37] M.-O. Mewes, M. R. Andrews, D. M. Kurn, D. S. Durfee, C. G. Townsend, and W. Ketterle. Output coupler for Bose-Einstein condensed atoms. *Phys. Rev. Lett.*, 78(4):582–585, Jan 1997. doi: 10.1103/PhysRevLett.78.582.

[38] D. M. Stamper-Kurn, M. R. Andrews, A. P. Chikkatur, S. Inouye, H.-J. Miesner, J. Stenger, and W. Ketterle. Optical confinement of a Bose-Einstein condensate. *Phys. Rev. Lett.*, 80(10):2027–2030, Mar 1998. doi: 10.1103/PhysRevLett.80.2027.

[39] H. Haken and H. C. Wolf. *The Physics of Atoms and Quanta*. Springer-Verlag, 1993.

[40] M. D. Barrett, J. A. Sauer, and M. S. Chapman. All-optical formation of an atomic Bose-Einstein condensate. *Phys. Rev. Lett.*, 87(1):010404, Jun 2001. doi: 10.1103/PhysRevLett.87.010404.

[41] H. Schmaljohann, M. Erhard, J. Kronjäger, M. Kottke, S. van Staa, L. Cacciapuoti, J. J. Arlt, K. Bongs, and K. Sengstock. Dynamics of $f = 2$ spinor Bose-Einstein condensates. *Phys. Rev. Lett.*, 92(4):040402, Jan 2004. doi: 10.1103/PhysRevLett.92.040402.

[42] Fabrice Gerbier, Artur Widera, Simon Fölling, Olaf Mandel, Tatjana Gericke, and Immanuel Bloch. Phase coherence of an atomic mott insulator. *Phys. Rev. Lett.*, 95(5):050404, Jul 2005. doi: 10.1103/PhysRevLett.95.050404.

[43] D. E. Sproles. *in preparation*. Master's thesis, Stony Brook University, 2009.

[44] Daniel Pertot, Daniel Greif, Stephan Albert, Bryce Gadway, and Dominik Schneble. Versatile transporter apparatus for experiments with optically trapped Bose-Einstein condensates, 2009. URL http://www.citebase.org/abstract?id=oai:arXiv.org:0907.1323.

[45] Daniel Adam Steck. Rubidium 87-D line data, revision 2.0.1. *http://steck.us/alkalidata*, 2008.

[46] Yutaka Yoshikawa, Takeshi Umeki, Takuro Mukae, Yoshio Torii, and Takahiro Kuga. Frequency stabilization of a laser diode with use of light-induced birefringence in an atomic vapor. *Appl. Opt.*, 42(33):6645–6649, 2003. URL http://ao.osa.org/abstract.cfm?URI=ao-42-33-6645.

[47] A. Yariv and P. Yeh. *Photonics - optical electronics and modern communication*. Oxford University Press, 2007.

[48] Coherent 899 Ring Laser Ti:Sa Manual. Appendix A - gain medium information - high power, short wavelength configuration.

[49] René Reimann. The coherent ring laser 899 pumped by a verdi v-10, (stony brook - laser course term paper - unpublished), 2008.

[50] W. Ketterle and N.J. van Druten. Evaporative cooling of trapped atoms. *Adv. At. Mol. Opt. Phys.*, 37:181–236, Dec 1996.

[51] V. S. Letokhov. Narrowing of the Doppler width in a standing light wave. *JETP Lett.*, 7(7):348–351, 1968. URL http://www.jetpletters.ac.ru/ps/1685/article_25663.pdf.

[52] Steven Chu, J. E. Bjorkholm, A. Ashkin, and A. Cable. Experimental observation of optically trapped atoms. *Phys. Rev. Lett.*, 57(3):314–317, Jul 1986. doi: 10.1103/PhysRevLett.57.314.

[53] L. Allen and J. H. Eberly. *Optical resonance and two-level atoms*. Dover Book, 1975.

[54] Claude Chohen-Tannoudji, Jacques Dupont-Roc, and Gilbert Grynberg. *Atom-photon interactions*. Wiley-VCH Verlag, 2004.

[55] Nir Friedman, Ariel Kaplan, and Nir Davidson. Dark optical traps for cold atoms. *Advances in atomic, molecular and optical physics*, 48:99–151, 2002.

[56] J. H. Müller, O. Morsch, D. Ciampini, M. Anderlini, R. Mannella, and E. Arimondo. Atomic micromotion and geometric forces in a triaxial magnetic trap. *Phys. Rev. Lett.*, 85(21):4454–4457, Nov 2000. doi: 10.1103/PhysRevLett.85.4454.

[57] Yong P. Chen, J. Hitchcock, M. Junker D. Dries, C. Welford, S. E. Pollack, T. A. Corcovilos, and R. G. Hulet. Experimental Studies of Bose-Einstein Condensates in Disorder. *Physica D*, 238, 2009.

[58] Phillip L. Gould, George A. Ruff, and David E. Pritchard. Diffraction of atoms by light: The near-resonant Kapitza-Dirac effect. *Phys. Rev. Lett.*, 56(8):827–830, Feb 1986. doi: 10.1103/PhysRevLett.56.827.

[59] Peter J. Mar, Bruce G. Oldaker, Andrew H. Miklich, and David E. Pritchard. Bragg scattering of atoms from a standing light wave. *Phys. Rev. Lett.*, 60(6):515–518, Feb 1988. doi: 10.1103/PhysRevLett.60.515.

[60] H. Batelaan. Colloquium: Illuminating the Kapitza-Dirac effect with electron matter optics. *Reviews of Modern Physics*, 79(3):929, 2007. doi: 10.1103/RevModPhys.79.929. URL http://link.aps.org/abstract/RMP/v79/p929.

[61] Markus Greiner. *Ultracold quantum gases in three-dimensional optical lattice potentials*. PhD thesis, LMU Munich, Germany, 2003.

[62] Oliver Morsch and Markus Oberthaler. Dynamics of Bose-Einstein condensates in optical lattices. *Reviews of Modern Physics*, 78(1):179, 2006. doi: 10.1103/RevModPhys.78.179. URL http://link.aps.org/abstract/RMP/v78/p179.

[63] J Hecker Denschlag, J E Simsarian, H Haffner, C McKenzie, A Browaeys, D Cho, K Helmerson, S L Rolston, and W D Phillips. A Bose-Einstein condensate in an optical lattice. *Journal of Physics B: Atomic, Molecular and Optical Physics*, 35(14):3095–3110, 2002. URL http://stacks.iop.org/0953-4075/35/3095.

[64] Jakub Zakrzewski and Dominique Delande. Breakdown of adiabaticity when loading ultra-cold atoms in optical lattices, 2009. URL http://www.citebase.org/abstract?id=oai:arXiv.org:0902.1117.

[65] P.L. Kapitza and P.A.M Dirac. The reflection of electrons from standing light waves. *Proc. Cambridge Phil. Soc.*, 29:297, Apr 1931.

[66] Bryce Gadway, Daniel Pertot, Rene Reimann, Martin G. Cohen, and Dominik Schneble. Analysis of Kapitza-Dirac diffraction patterns beyond the Raman-Nath regime, 2009. URL http://www.citebase.org/abstract?id=oai:arXiv.org:0907.3507.

[67] J. H. Huckans, I. B. Spielman, B. Laburthe Tolra, W. D. Phillips, and J. V. Porto. Quantum and classical dynamics of a BEC in a large-period optical lattice, 2009. URL http://www.citebase.org/abstract?id=oai:arXiv.org:0901.1386.

[68] Olaf Mandel. *Entanglement with quantum gates in an optical lattice*. PhD thesis, LMU Munich, Germany, 2005.

[69] Albert Haug. *Theoretical solid state physics, Volume 1*. Pergamon Press, 1972.

[70] Dieter Jaksch. *Bose-Einstein Condensation and Applications*. PhD thesis, Leopold-Franzens-University Innsbruck, Austria, 1999.

[71] Wolfgang. *Grundkurs Theoretische Physik 7, Viel-Teilchen-Theorie*. Springer Verlag, 2005.

[72] Subir Sachdev. *Quantum Phase Transitions*. Cambridge University Press, 1999.

[73] Markus Greiner, Olaf Mandel, Theodor W. Hansch, and Immanuel Bloch. Collapse and revival of the matter wave field of a Bose-Einstein condensate. *Nature*, 419(6967), 2002.

[74] Wolfgang Ketterle. Icap, summer school on atomic physics - course notes, 21 july,. 2008.

[75] D. van Oosten, P. van der Straten, and H. T. C. Stoof. Quantum phases in an optical lattice. *Phys. Rev. A*, 63(5):053601, Apr 2001. doi: 10.1103/PhysRevA.63.053601.

[76] F. Gerbier, S. Trotzky, S. Fölling, U. Schnorrberger, J. D. Thompson, A. Widera, I. Bloch, L. Pollet, M. Troyer, B. Capogrosso-Sansone, N. V. Prokof'ev, and B. V. Svistunov. Expansion of a quantum gas released from an optical lattice. *Physical Review Letters*, 101(15):155303, 2008. doi: 10.1103/PhysRevLett.101.155303. URL http://link.aps.org/abstract/PRL/v101/e155303.

[77] L.-M. Duan, E. Demler, and M. D. Lukin. Controlling spin exchange interactions of ultracold atoms in optical lattices. *Phys. Rev. Lett.*, 91(9):090402, Aug 2003. doi: 10.1103/PhysRevLett.91.090402.

[78] A. B. Kuklov and B. V. Svistunov. Counterflow superfluidity of two-species ultracold atoms in a commensurate optical lattice. *Phys. Rev. Lett.*, 90(10):100401, Mar 2003. doi: 10.1103/PhysRevLett.90.100401.

[79] Juan Jose Garcia-Ripoll and Juan Ignacio Cirac. Spin dynamics for bosons in an optical lattice. *New Journal of Physics*, 5:76, 2003. URL http://stacks.iop.org/1367-2630/5/76.

[80] A. Isacsson, Min-Chul Cha, K. Sengupta, and S. M. Girvin. Superfluid-insulator transitions of two-species bosons in an optical lattice. *Phys. Rev. B*, 72(18):184507, Nov 2005. doi: 10.1103/PhysRevB.72.184507.

[81] Ehud Altman, Walter Hofstetter, Eugene Demler, and Mikhail D Lukin. Phase diagram of two-component bosons on an optical lattice. *New Journal of Physics*, 5:113, 2003. URL http://stacks.iop.org/1367-2630/5/113.

[82] Krzysztof Gawryluk, Mirosław Brewczyk, Kai Bongs, and Mariusz Gajda. Resonant Einstein–de Haas effect in a rubidium condensate. *Physical Review Letters*, 99(13):130401, 2007. doi: 10.1103/PhysRevLett.99.130401. URL http://link.aps.org/abstract/PRL/v99/e130401.

[83] E. L. Hahn. Spin echoes. *Phys. Rev.*, 80(4):580–594, Nov 1950. doi: 10.1103/PhysRev.80.580.

[84] Kenneth Günter, Thilo Stöferle, Henning Moritz, Michael Köhl, and Tilman Esslinger. Bose-Fermi mixtures in a three-dimensional optical lattice. *Physical Review Letters*, 96(18):180402, 2006. doi: 10.1103/

PhysRevLett.96.180402. URL http://link.aps.org/abstract/PRL/v96/e180402.

[85] C. Ospelkaus, S. Ospelkaus, L. Humbert, P. Ernst, K. Sengstock, and K. Bongs. Ultracold heteronuclear molecules in a 3d optical lattice. *Physical Review Letters*, 97(12):120402, 2006. doi: 10.1103/PhysRevLett.97.120402. URL http://link.aps.org/abstract/PRL/v97/e120402.

[86] Roman M. Lutchyn, Sumanta Tewari, and S. Das Sarma. Boson Hubbard model with weakly coupled fermions. *Physical Review B (Condensed Matter and Materials Physics)*, 78(22):220504, 2008. doi: 10.1103/PhysRevB.78.220504. URL http://link.aps.org/abstract/PRB/v78/e220504.

[87] Lode Pollet, Corinna Kollath, Ulrich Schollwöck, and Matthias Troyer. Mixture of bosonic and spin-polarized fermionic atoms in an optical lattice. *Physical Review A (Atomic, Molecular, and Optical Physics)*, 77(2):023608, 2008. doi: 10.1103/PhysRevA.77.023608. URL http://link.aps.org/abstract/PRA/v77/e023608.

[88] Group of D. Jaksch. private communication, 2009.

[89] S. G. Soyler, B. Capogrosso-Sansone, N. V. Prokof'ev, and B. V. Svistunov. Sign-alternating interaction mediated by strongly-correlated lattice bosons. *New Journal of Physics*, 11:073036, 2009. URL http://www.citebase.org/abstract?id=oai:arXiv.org:0811.0397.

[90] E. Tiesinga, B. J. Verhaar, and H. T. C. Stoof. Threshold and resonance phenomena in ultracold ground-state collisions. *Phys. Rev. A*, 47(5):4114–4122, May 1993. doi: 10.1103/PhysRevA.47.4114.

[91] S. Inouye, M. R. Andrews, J. Stenger, H.-J. Miesner, D. M. Stamper-Kurn, and W. Ketterle. Observation of Feshbach resonances in a Bose-Einstein condensate. *Nature*, 392(6672), 1998.

[92] A. Marte, T. Volz, J. Schuster, S. Dürr, G. Rempe, E. G. M. van Kempen, and B. J. Verhaar. Feshbach resonances in rubidium 87: Precision measurement and analysis. *Phys. Rev. Lett.*, 89(28):283202, Dec 2002. doi: 10.1103/PhysRevLett.89.283202.

[93] Thomas Bergeman. private communication, 2009.

[94] Heather Jean Lewandowski. *Coherences and correlations in an ultracold Bose gas*. PhD thesis, University of Colorado, 2002.

[95] J. Catani, L. De Sarlo, G. Barontini, F. Minardi, and M. Inguscio. Degenerate bose-bose mixture in a three-dimensional optical lattice. *Physical Review A (Atomic, Molecular, and Optical Physics)*, 77(1):011603, 2008. doi: 10.1103/PhysRevA.77.011603. URL http://link.aps.org/abstract/PRA/v77/e011603.

[96] T. Okoshi, K. Kikuchi, and A. Nakayama. Novel method for high resolution measurement of laser output spectrum. *Electronics Letters*, 16(16): 630–631, 31 1980. ISSN 0013-5194. doi: 10.1049/el:19800437.

[97] Hidemi Tsuchida. Simple technique for improving the resolution of the delayed self-heterodyne method. *Opt. Lett.*, 15(11):640, 1990. URL http://ol.osa.org/abstract.cfm?URI=ol-15-11-640.

Appendix A

Linewidth of Coherent 899-21 Ring Laser

The linewidth[1] of the 899 Ring Laser needs to be known to make sure that it is narrow enough to use the laser for optical lattice experiments. A too broad linewidth leads to heating in the atom-lattice system and the desired circumstances of the BHM are not given any more (see 5.2).
Homodyning[2] is a well-known technique for measuring the linewidth of a laser. Using this technique the laser output is combined with a delayed and frequency shifted version of itself. The combined signal can then be monitored with a spectrum analyzer [96]. The delay has to be on the order of the coherence length of the laser light to ensure that in the end the signal consists of two different wave packets. To achieve this delay, generally an optical fiber is used. In our experiment the linewidth of the 899 Ring laser is expected to be around 0.5 MHz, requiring a fiber with a length of several hundreds of meters for a sufficient resolution. Even though there have been improvements on the resolution of the method [97] still a fiber of the mentioned order of length would be needed.
To overcome the lack of such a fiber a second laser with an adequate small linewidth can be used as a reference signal. In a simple picture one can assume an infinitely small linewidth for two lasers with different frequencies ω_1 and ω_2. Beating this two lasers against each other, one would anticipate interference terms at $\omega_1 + \omega_2$ and at $\Delta = |\omega_1 - \omega_2|$. Since lasers emit light in the range of hundreds of nm the first term would be in the region of 10^{15} Hz and therefore too fast oscillating to be measured electronically. However it is possible to measure the-so called beat signal of the two lasers at $\omega = \Delta$, as long as the

[1] linewidth=FWHM
[2] also called self-heterodyning

spacing is within the frequency range of an oscilloscope or spectrum analyzer (typical value $\sim$ GHz).
In our case we want to measure the linewidth of the 899 Ring Laser Γ_{899} by overlapping its beam with the beam of the DL Pro 780 Laser. The linewidth of the DL Pro 780 Laser Γ_{780} is specified to be smaller than 200 kHz and therefore sharp enough to act as a reference signal. The setup for the measurement is shown in Fig. A.1. The beams of the two lasers with parallel polarizations are coupled into a fiber to guarantee spatial overlap. Both laser outputs are monitored with a Fabry-Perót interferometer to ensure single mode operation.

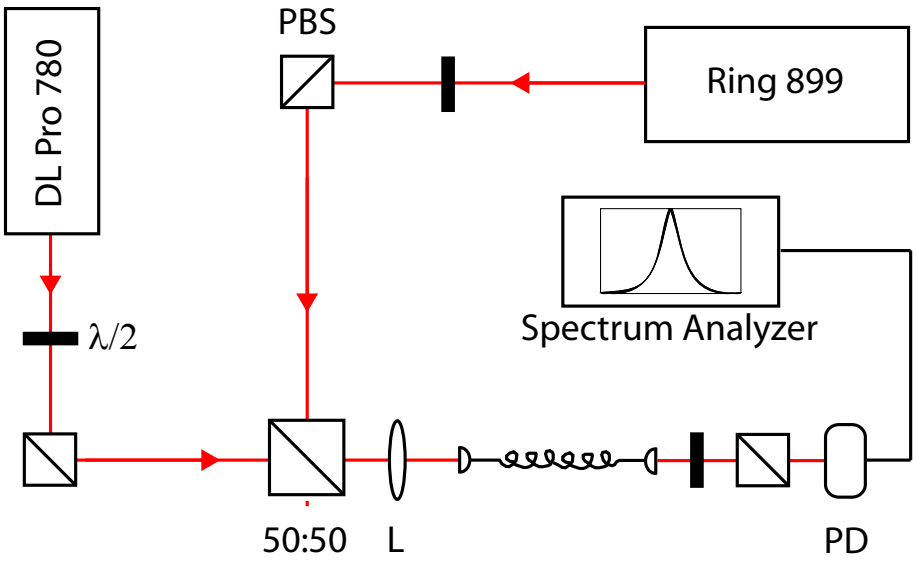

Figure A.1: Simplified setup for the linewidth measurement of the Ring Laser 899. The polarization of the two laser beams is cleaned up before combining them on a non-polarizing 50-50 beam splitter. The beams with equal polarization are now coupled into a fiber to ensure perfect overlap. Since the fiber is not polarization maintaining a third PBS is used before measuring the signal with a spectrum analyzer via a photodiode. The graphic does not show the setups used for the polarization spectroscopy, Fabry-Perót interferometer and the mirrors for aligning the beams.

To find the beat note, both lasers scan at maximum scan width and the signal at the photodiode[3] is monitored with an oscilloscope. By changing the wavelength of the 899 Ring Laser slightly the beat signal at the oscilloscope can be

[3]Thorlabs DET 110 with 50 Ω terminating resistor, bandwidth $\sim$ 160 MHz

observed. In order to lock the two lasers at nearly the same frequency, the scan width of the lasers has to be lowered by small amounts while the beat note must not disappear from the oscilloscope. The lasers have to be locked closely to each other to stay within the bandwidth of the photodiode. The DL Pro 780 is locked to its spectroscopy signal while the 899 Ring Laser is locked to its external cavity. Now one can monitor the signal with a spectrum analyzer[4] to view the combined linewidth of both lasers Γ_c. With a scan time of ca. 2 s for the whole line, the combined linewidth is measured as $\Gamma_c = (800 \pm 50)$ kHz, where the height at half width full maximum equals -6 dBm compared to the maximum of the line. Fig. A.2 shows a screenshot of the spectrum analyzer with the described line.

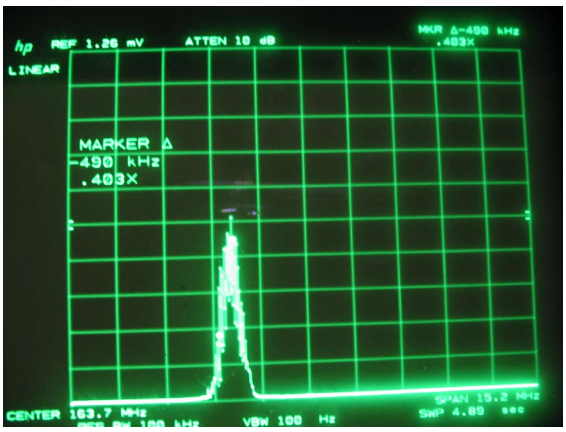

Figure A.2: Photo of spectrum analyzer with beat signal of DL Pro 780 and 899 Ring Laser. The amplitude scale is linear. The span of the whole screen is 15.2 MHz.

To check the measurement for consistency the 899 Ring Laser is exchanged for the locked DL 100 Laser which has a specified linewidth of ~ 500 kHz. In this case the combined linewith is (500 ± 50) kHz. Therefore the DL Pro 780 Laser appears indeed to be a sharp reference signal. In conclusion the linewidth of the 899 Ring Laser can be estimated to be:

$$\underline{\Gamma_{899} \lesssim 800 \text{ kHz}}$$

Since a slow drift of the line Γ_c on the order of 100 kHz$\cdot$s^{-1} is observed the given value can be considered as an upper bound. For the beat signal of the

[4]HP 8566A Spectrum Analyzer

DL Pro 800 and the DL 100 the combined line was much more stable in time (slow jitter which remains within 50 kHz around the center of the line). This means that the slow drift of Γ_c is induced by the 899 Ring Laser.
The 899 Ring Laser is well suited for performing an OL experiment.

Appendix B

List of Abbreviations

AF Antiferromagnetic (phase). This phase of the two-component BHM has a checkerboard structure where atoms of different species alternate.

AOM Acousto-optic modulator. This device is used to diffract light by a sound wave. Frequency shifts of the light in the MHz range are the result.

BEC Bose-Einstein condensate. For very low temperatures bosonic atoms macroscopically occupy the lowest energetic state of their system which then can be described by a single wave function.

BHH Bose-Hubbard Hamiltonian. The quantum mechanical Hamiltonian of the BHM.

BHM Bose-Hubbard model. This model describes bosons in a lattice. The dynamic is driven by tunneling rates to neighboring sites and onsite interaction energies.

CCD Charge-coupled device. The principle is to convert photonic energy to electrical one. CCD-chips are used in most modern cameras.

FM Ferromagnetic (phase). In this phase of the two-component BHM all lattice sites are occupied by one atomic species.

MI Mott insulator. In this phase of the BHM the atoms are pinned to specific lattice sites. There is no macroscopic phase which would lead to interferences as for the SF phase.

MOT Magneto-optical trap. Combining red detuned laser beams and magnetic field gradients, the MOT traps and cools atom down a few tens of μK

OL Optical lattice. The simple principle of a standing light wave and the dipole force (see. 4.1) are here used to trap quantum gases in a 3D OL.

PID Proportional - integral - derivative (controller). The controller combines the advantages of an proportional, integral and derivative controller. The device is used to stabilize a system at a wanted point by correcting the error with respect to the wanted point.

RF Radio frequency. Electromagnetic radiation in the $\sim$MHZ range.

SDOL State-dependent optical lattice. An OL that has significantly different potentials for different internal atomic states. The state dependence is achieved by the choice of a certain wavelength and polarization of the lattice light.

SF Superfluid (phase). In this phase of the BHM the atoms move freely in the OL. There is a macroscopic phase which leads to interferences in contrast to the MI phase.

TOF Time-of-flight. The time of flight technique is widely used in the BEC community. The atoms fall under the effect of gravitation after switching of the trap. The quantum pressure of the cloud reveals the BEC momentum distribution for long enough TOF.

TOP Time-averaged orbiting potential (trap). To avoid that ultra cold atoms undergo Majorana flips in the field zero of the time independent magnetic trap, a magnetic time orbiting potential is added which results in a harmonic confinement for the atoms with no field zero.

XODT Crossed optical dipole trap. The XODT is used to trap the atoms independently of their internal state. The atom light interaction comes in due to the conservative dipole potential (see. 4.1).

XY XY (phases). These phases of the two-component BHM consist of coherent superpositions of atoms in state one and two which are not described by the FM or AF phase.